Active Galactic Nuclei in Dwarf Galaxies

by

Vivienne Francesca Baldassare

A dissertation submitted in partial fulfillment
of the requirements for the degree of
Doctor of Philosophy
(Astronomy and Astrophysics)
in The University of Michigan
2017

Doctoral Committee:

Associate Professor Elena Gallo, Chair
Dr. Laura Ferrarese, Herzberg Institute for Astrophysics
Associate Professor Oleg Y. Gnedin
Associate Professor Dragan Huterer
Associate Research Professor Monica Valluri

Vivienne Francesca Baldassare

vbaldas@umich.edu

ORCID iD: 0000-0003-4703-7276

© Vivienne Francesca Baldassare 2017

"Because survival is insufficient" -*Station Eleven* by Emily St. John Mandel

To Jeremy and Henri.

ACKNOWLEDGEMENTS

Firstly, I am incredibly grateful to my PhD advisor, Elena Gallo, for her mentorship, support, and guidance. Over the last five years, Elena has demonstrated to me how to be a careful, quantitative, and thorough scientist while never losing sight of the larger context of your results. I have benefited greatly from her advice and perspective on many matters, scientific and otherwise.

I have been fortunate to be surrounded by many excellent scientists. In particular, I would like to acknowledge my collaborators Amy Reines and Jenny Greene for their mentorship and scientific guidance, which have helped shape my career in astronomy.

I am grateful to the other members of my thesis committee – Laura Ferrarese, Oleg Gnedin, Monica Valluri, and Dragan Huterer – for their input throughout my graduate career; their comments and suggestions have improved this thesis and my work overall.

My sincerest gratitude is extended to the entire University of Michigan Astronomy Department. It was a pleasure to earn my degree in such a collaborative, supportive, and friendly environment. I am especially grateful for my graduate cohort, who made study sessions more bearable with friendship and nachos.

I am grateful for financial support in the form of a National Science Foundation Graduate Research Fellowship, and a Predoctoral Fellowship from the Rackham Graduate School at the University of Michigan.

I am thankful to my parents, Andrea and Wayne, for their unending support, love, and encouragement, and for always reminding me to “keep fighting”.

Thank you to my sister and co-conspirator Lily for inspiring me every day to be more bold and confident, and for being the Frodo to my Samwise.

Finally, I am especially grateful to have taken this journey alongside my husband, Jeremy Hoskins: my best friend; co-adventurer; and the guardian of my solitude.

TABLE OF CONTENTS

LIST OF FIGURES

Figure

LIST OF TABLES

Table

ABSTRACT

Supermassive Black Holes (BHs; typically with mass $M_{\rm BH} \gtrsim 10^5\ M_\odot$) are ubiquitous in the cores of all massive galaxies ($M_* \gtrsim 10^{10} M_\odot$). However, BHs in dwarf galaxies ($M_* \gtrsim 10^{9.5} M_\odot$) are more difficult to detect, and thus have remained relatively elusive. Theoretical work suggests that clues to BH formation and growth can be found in present day dwarf galaxies, making this an important population to study.

Searching for signs of BH accretion is one way of identifying BHs in dwarf galaxies more distant than the Local Group. Until recently, only a handful of dwarf galaxies had been identified with actively accreting central BHs, or Active Galactic Nuclei (AGNs). However, with the advent of large-scale surveys, it has been possible to search for signs of BH accretion in samples comprised of tens of thousands of galaxies. Recent works have identified roughly two hundred dwarf galaxies with AGN signatures, making it possible to begin to carry out demographic studies. This thesis describes an in-depth, multi-wavelength characterization of this relatively unexplored population. We determine which observational AGN identifiers used for massive galaxies also apply for dwarf galaxies, study the accretion properties of confirmed AGNs, and explore relationships between BH mass and host galaxy properties in these systems. We also present evidence for an active $\sim 50,000\ M_\odot$ BH in the center of the dwarf galaxy RGG 118, which at the time of writing, is the smallest BH yet reported in a galaxy center.

CHAPTER I

Introduction

In this introduction, I give an overview of the structure and observational signatures of actively accreting Massive Black Holes (BHs, typically with BH masses $M_{BH} \gtrsim 10^5 M_{\odot}$), also termed Active Galactic Nuclei (AGNs). I discuss the concept of co-evolution of galaxies and their central BHs, as evidenced by scaling relations between BH mass and large-scale host galaxy properties. I also detail different methods used for estimating the masses of BHs. I describe different theories for BH formation at high redshift, and discuss how BHs in present-day dwarf galaxies can place constraints on the formation mechanisms. Finally, I introduce the field of active galactic nuclei in dwarf galaxies. Throughout this thesis, the term dwarf galaxies refers to galaxies with stellar masses $M_* \lesssim 3 \times 10^9 M_{\odot}$.

The work described in this thesis comprises an in-depth characterization of AGNs in dwarf galaxies by way of multi-wavelength observations of well-defined subsamples of dwarf galaxies with optical spectroscopic signatures of AGN activity. An overview of open questions in this field is given at the end of the introduction.

1.1 Background: active galactic nuclei

1.1.1 Brief history of AGNs

Quasars are exceptionally bright celestial sources, named as such because they often appear as point sources in the night sky, similar to stars (quasar comes from "quasi-stellar

radio source"). The first quasars were identified as bright radio sources of unknown origin. In 1963, Maarten Schmidt used the Palomar 200-inch telescope to observe the quasar 3C 273, and realized that it had a redshift of $z = 0.158$ based on optical emission lines Schmidt (1963). This firmly established quasars as extragalactic sources.

Quasars have high bolometric luminosities (in excess of 10^{45-46} erg s^{-1}) and variability on the order of hours to days. This led astronomers to conclude that they were powered by accretion (i.e., the release of gravitational potential energy from in-falling matter) onto very compact, supermassive objects (e.g., Salpeter 1964). Two decades later, Soltan (1982) argued that if quasars are indeed powered by accretion onto BHs, dead (or quiescent) quasars should exist in the cores of present-day galaxies. This would later be confirmed by the *Hubble Space Telescope* (HST). Prior to HST, BH masses had been measured for a handful of nearby galaxies (e.g., M31, M32, NGC 3115) using optical/near-IR absorption line spectroscopy (Dressler & Richstone 1988; Kormendy & Richstone 1992). The superior angular resolution of HST confirmed these detections, and allowed for dynamical BH detections in many more systems, heralding an era of BH demographic studies (Magorrian et al. 1998; Kormendy 2004; Kormendy & Ho 2013). We now know that BHs exist in the cores of virtually all massive galaxies (i.e., with stellar masses $M_* \gtrsim 10^{10} M_\odot$). The term AGN broadly refers to BHs with detectable accretion signatures down to some luminosity limit. Quasars comprise the most luminous end of this distribution.

1.1.2 AGN structure

AGN emit across the entire electromagnetic spectrum, from low-energy radio waves to high-energy X-rays and gamma rays. AGN are comprised of several different components, including the central BH, accretion disk, and dusty torus (see Figure 1.1 for a schematic). Below, I describe each individual component in more detail.

- Central supermassive black hole: As mentioned above, AGNs are powered by accreting BHs. These BHs typically weigh in excess of $\sim 10^5\ M_\odot$, with some weighing more than $10^{10}\ M_\odot$ (Kelly & Merloni 2012).

- Accretion disk: As gas in the vicinity of the BH spirals towards it, it forms an accretion disk with a radius of approximately several hundred AU ($\sim 10^{-3}$ pc). As this material sheds angular momentum, it gradually accretes onto the BH from the disk, converting gravitational potential energy into heat. Since angular momentum is conserved in the disk, in order for the gas to lose angular momentum and accrete onto the BH, angular momentum must also be transported outwards. Current theories suggest magneto-rotational instability in the accretion disk drives turbulence in the disk, allowing for outward transport of angular momentum.

- Broad-line region: Gas in the broad line region is photoionized by photons from the accretion disk. This gas is also dense ($n_e \gtrsim 10^7\ \mathrm{cm}^{-3}$) and close enough to the BH (D $\lesssim$ several parsecs) for its motion to be dominated by the gravity of the BH. Emission lines generated in this region are broadened by the Doppler effect. From an observer's perspective, as gas in the broad line region rotates around the black hole, some will be observed to be moving towards the observer, and some will be moving away. Emission from gas that is moving away from the observer will be red-shifted to longer wavelengths; gas that is moving towards will be blue-shifted to shorter wavelengths. Thus, the emission line becomes broadened; the width of the broad emission line is related to how fast the gas is moving which in turn is set by the BH gravity.

- Narrow-line region: The narrow-line region gas is also photoionized by photons in the accretion disk, but is less dense than that in the broad line region ($n_e \lesssim 10^4\ \mathrm{cm}^{-3}$) and is farther from the BH (D~ 100 pc). Because this gas is less dense and collisions

less common, excited atoms in this region can undergo forbidden atomic transitions. Characteristic lines produced in the narrow-line region include $[\mathrm{OIII}]\lambda 5007$.

- Torus: The accretion disk is thought to be surrounded by an obscuring torus (scale of approximately $100 - 1000$ pc). While all narrow emission lines are observable for all AGNs, only a fraction show broadened emission lines. AGN unification suggests that all AGNs produce broad and narrow emission lines, but that some of the inner broad line regions are obscured by a dusty torus that blocks our line of sight.
- Jets: Some AGNs produce jets, or very collimated outflows of material. These jets can extend several kiloparsecs from the galaxy center. Radio emission from jets is thought to be synchrotron emission from electrons accelerated in a magnetic field.

1.1.3 Observational signatures of AGNs

In this section, I discuss observational signatures of AGN activity. As mentioned above, AGNs emit brightly across much of the entire electromagnetic spectrum. In addition to emitting over much of the electromagnetic spectrum, AGNs are also highly variable at all wavelengths. In particular, AGN X-ray emission, which is generated in a hot corona above the accretion disk, has been found to vary on timescales less than a day (see Mushotzky et al. 1993 for a review on X-ray variability of AGN). Variability was an important factor in determining the origin of bright quasar emission, since it constrains the size of the emitting region to have a radius less than one light-day (i.e., the source must be extremely compact).

Figure 1.2 shows the standard spectral energy distribution of a quasar (Elvis et al. (1994), see also Richards et al. (2006) for an updated version). Notable features include the non-thermal radio and X-ray emission, and "big blue bump" in the ultraviolet. The energy output of quasars is also roughly consistent over a wide range in frequencies – from

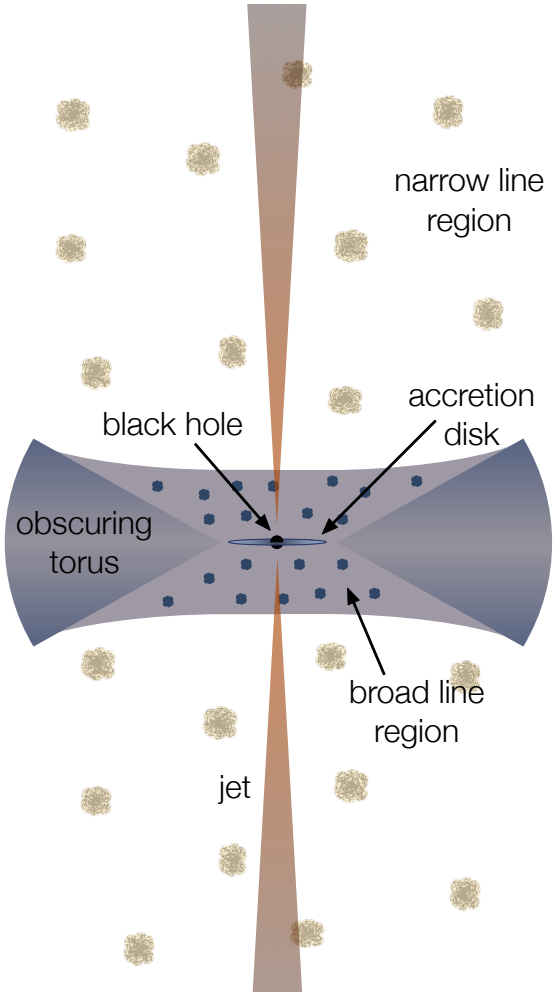

Figure 1.1 Simplified schematic of an active galactic nucleus (not to scale). Figure inspired by schematic from Urry & Padovani (1995). Depending on the viewing angle, the emission from the broad line region clouds may or may not be visible.

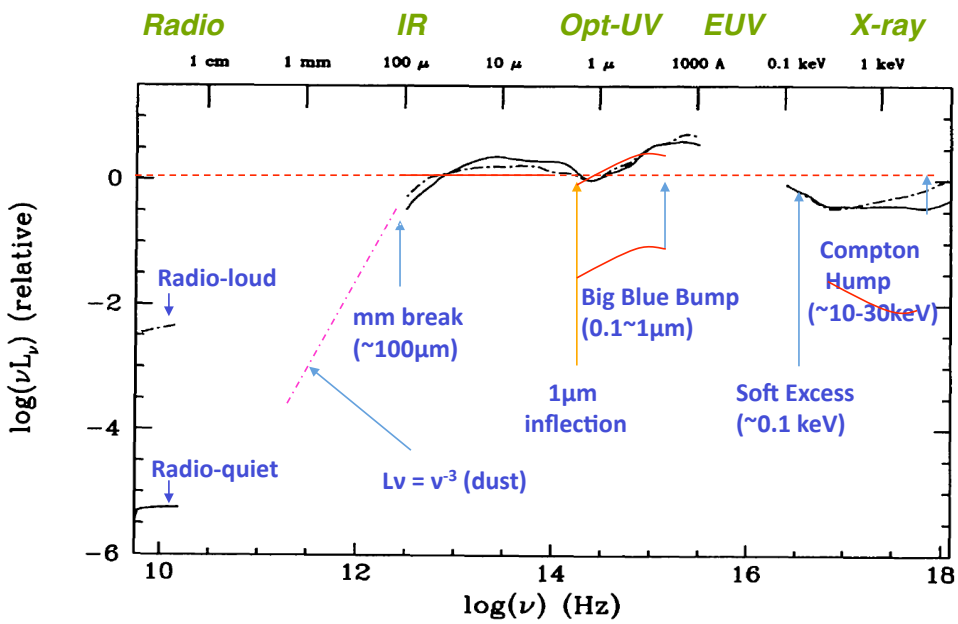

Elvis et al., 1994, ApJS, 95, 1

Figure 1.2 Typical quasar spectral energy distribution from Elvis et al. (1994).

the infrared through X-ray.

Continuum from the accretion disk emits in the optical/UV. The UV "big blue bump" is thought to be the sum of black bodies at varying temperatures, produced by continuum emission from different radii in the accretion disk. The continuum emission from the accretion disk photoionizes gas within the galaxy, producing bright optical emission lines. Hα and Hβ emission lines are sometimes observed to have broad emission line components with line widths upwards of 1000 $\mathrm{km\ s^{-1}}$. These broadened emission lines are generated in the dense broad-line region where the motion of the gas is dominated by the gravity of the BH. Narrow forbidden emission lines are also used for AGN detection. "Forbidden" atomic transitions occur extremely rarely; in the high density broad line region, atoms are disturbed via collisions before forbidden atomic transitions can occur. Thus, we only observe these transitions occurring in the lower-density narrow line region gas, which is more distant from the BH. Typical forbidden transitions observed in the optical spectra

of AGNs include [OIII] $\lambda 4959$ and $\lambda 5007$, the [NII] $\lambda\lambda 6548, 6583$ doublet, and the [SII] $\lambda\lambda 6717, 6731$ doublet.

AGNs are not the only astrophysical phenomena that result in forbidden emission lines. These emission lines are also observed in star forming galaxies; in this case, the photoionizing continuum comes from HII regions around newborn stars. However, different photoionizing continua produce different relative emission line strengths, i.e., certain ratios of emission line fluxes differ depending on whether the source of ionization is an AGN or an HII region. The "BPT" diagram (named for Baldwin, Phillips & Terlevich 1981) separates galaxies according to their photoionizing continuum. In particular, the BPT diagram uses the flux ratio [OIII]$\lambda 5007$ / H$\beta\lambda 4861$ versus [NII]$\lambda 6583$ / H$\alpha\lambda 6563$ to divide AGN and star forming galaxies. Later work expanded on the original dividing lines, adding a category for objects with contributions from both an AGN and star formation (Kewley et al. 2001; Kauffmann et al. 2003; Kewley et al. 2006).

X-ray emission from AGNs is thought to be generated via inverse Compton scattering of lower-energy photons emitted by the accretion disk by electrons in the hot corona above the accretion disk. Luminous X-ray emission ($L_X \gtrsim 10^{42}$ erg s^{-1}) is a commonly used identifier of AGN activity, though soft X-rays are sometimes obscured by dust. The shape of the X-ray spectrum of AGNs is also consistent with Comptonization. Other X-ray features of AGN include a high energy bump at $\sim 20 - 100$ keV, and the relativistic Fe Kα emission line (see reviews by Fabian et al. 2000; Risaliti & Elvis 2004).

An important diagnostic of AGN power is the Eddington fraction. The Eddington luminosity is the maximum luminosity of any accreting object, set by the balance of inward gravitational force with radiation pressure outward. The expression for the Eddington luminosity is $L_{\rm Edd} = 4\pi\, G\, M\, m_p\, c/\sigma_T$, where G is the gravitational constant, M is the mass of the accreting object, m_p is the mass of a proton, c is the speed of light, and σ_T is the

Thomson cross section. This simplifies to $L_{\rm Edd} = 1.2 \times 10^{38} \times (M_{\rm BH}/M_{\odot})\ {\rm erg\ s^{-1}}$. Given the mass of the accreting object and its luminosity, you can determine at what percentage of maximal it is accreting at. For example, if a $10^6\ M_{\odot}$ BH has a total luminosity of 10^{43} ${\rm erg\ s^{-1}}$, it is accreting at $\sim\ 10\%$ of its Eddington luminosity (or 10% of its maximum accretion rate).

Often, the BH luminosity is measured in one band (i.e., in X-rays). However, given the spectral energy distribution, it is possible to infer the total power of the AGN from the luminosity in one band by applying a *bolometric correction* (Marconi et al. 2004; Vasudevan & Fabian 2009). While the spectral energy distribution of massive AGNs is well constrained (Richards et al. 2006; Polletta et al. 2007), little is known about the spectral energy distribution for AGNs in dwarf galaxies. Thus, it is unclear whether the bolometric corrections for more massive systems should apply in the low-mass regime.

1.2 Evolution of galaxies and central massive black holes

1.2.1 Scaling relations

Despite their large masses, BHs have relatively small gravitational spheres of influence compared to the size of their host galaxies. For example, the Milky Way central massive BH Sgr A* has a gravitational sphere of influence $r\ =\ G\ \times\ M_{\rm BH}/\sigma^2\ \approx\ 2$ pc (for a bulge velocity dispersion $\sigma\ =\ 100\,{\rm km\,s^{-1}}$). The radius of the Milky Way disk, on the other hand, is ~ 15 kpc – several orders of magnitude larger than the gravitational sphere of influence of the BH. For this reason, studies focused on galaxy evolution were long considered to be a separate subject from studies of central BHs/AGNs. This picture has changed dramatically in the last two decades, with the discovery of tight "scaling relations" between BH mass and large-scale galaxy properties.

Seminal works released simultaneously by two groups (Ferrarese & Merritt 2000 and

Gebhardt et al. 2000a) reported on the discovery of a tight correlation between BH mass and the stellar velocity dispersion of the host galaxy bulge. The correlation was found to hold over several orders of magnitude in BH mass. The presence of a correlation between the BH mass and much larger-scale properties of the host galaxy points towards feedback between the growth of the BH and the growth of the galaxy, i.e., they regulate each other. In the two decades since this initial discovery, much work has been dedicated to understanding the impact that BHs have on the evolution of their hosts, and vice versa.

Since the discovery of the relation between BH mass and bulge stellar velocity dispersion (called the "M-sigma" or $M_{\rm BH} - \sigma_*$ relation), many authors have revisited the topic, building bigger samples of galaxies with measured BH masses and recalibrating the relation (see e.g., Gültekin et al. 2009; Woo et al. 2010; Xiao et al. 2011; McConnell & Ma 2013). Additionally, several other scaling relations have been discovered, such as the relation between BH mass and bulge mass (Marconi & Hunt 2003; Häring & Rix 2004), and the relation between BH mass and bulge luminosity (Marconi & Hunt 2003).

It has been suggested that scaling relations do not apply for certain systems, though this remains a topic of debate. For example, Kormendy & Ho (2013) argue that such scaling relations hold only for galaxies that with classical, dispersion-supported bulges, i.e., elliptical galaxies or bulge-dominated disk galaxies. Such systems also tend to be relatively massive $M_* \gtrsim 10^{10} M_\odot$. On the other hand, relations do not seem to hold for disk-dominated galaxies, or those with rotationally-supported pseudobulges. Disk-dominated/pseudobulge galaxies seem to sit below the scaling relations defined by classical bulges, i.e., their BHs are under-massive with respect to the relation.

Understanding under what circumstances scaling relations *do not* hold is also useful. Disk-dominated and low-mass galaxies are observed to have under-massive BHs with respect to local scaling relations; this suggests that their BHs are fed primarily through

secular processes, whereas BHs in massive galaxies with classical bulges may experience rapid growth during major galaxy mergers. On the other hand, BHs in very massive ultra-luminous infrared galaxies undergoing gas-rich mergers appear to be over-massive with respect to scaling relations, suggesting that in these systems, the BH grows quickly relative to the galaxy during the merger (Medling et al. 2015). Systems which deviate from scaling relations help illuminate precisely how galaxies and their BHs evolve.

1.2.2 BH mass measurements

Black holes are, by nature, invisible. Thus, techniques for estimating their mass rely on studying (directly or indirectly) the gravitational influence of the BH on stars or gas. Direct methods rely on measuring the dynamics of stars and gas in the vicinity of the BH (i.e., close enough to be gravitationally dominated by the BH). These produce the most accurate BH mass measurements. Indirect methods produce a BH mass estimate by relying on correlations between BH mass and other observables. While they are associated with larger uncertainties, these methods are useful as direct methods are infeasible for many systems.

The best-constrained BH mass measurement comes from the supermassive BH at the center of our own galaxy. Astronomers have now tracked the orbits of stars within the central few parsecs of the Milky Way for almost two decades. These stars are moving at speeds of thousands of kilometers per second around a common center of mass. Some, such as the S0-2 star, have been observed throughout their entire orbit. By measuring the orbital parameters of these stars, astronomers have inferred the presence of an unseen mass at the center of our galaxy weighing roughly 4 million times the mass of our Sun (Schödel et al. 2002, 2003; Ghez et al. 2003, 2005, 2008).

The next most reliable BH mass measurements come from water megamaser spots in circumnuclear disks. Water masers emit at 22 GHz, and are sometimes observed in

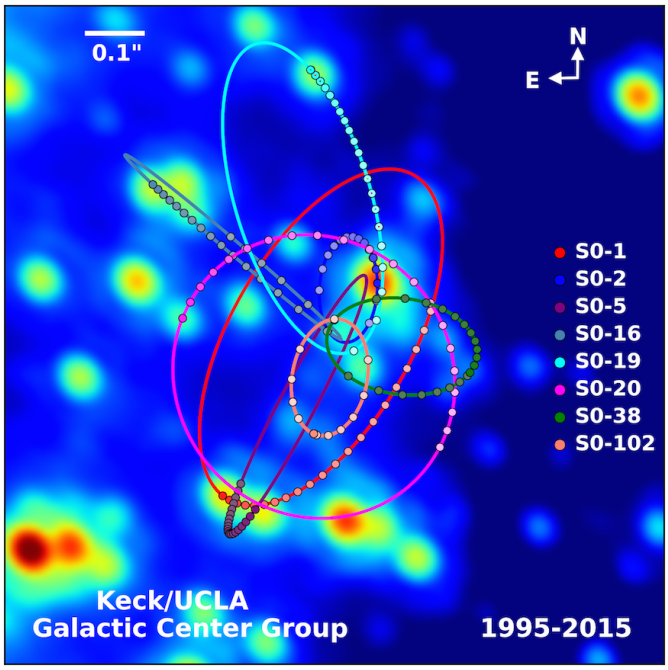

Figure 1.3 Stellar orbits at the center of the Milky Way. This image was created by Prof. Andrea Ghez and her research team at UCLA and is from data sets obtained with the W. M. Keck Telescopes.

rotating circumnuclear disks. The observed velocities and positions of the masers are well described by Keplerian orbits (see, e.g., Kuo et al. 2011), allowing one to very accurately determine the central mass. For galaxies with masers in circumnuclear disks, the mass enclosed within less than a parsec can be determined. The best-studied and first system with a BH mass measured via megamasers is NGC 4258 (Miyoshi et al. 1995); since then, more than two dozen galaxies with water megamaser disks have been identified. This technique has been especially useful for measuring BH masses in spiral galaxies (as opposed to very massive elliptical galaxies; Greene et al. 2010; Kuo et al. 2011; Greene et al. 2016).

Stellar and gas dynamical methods are often used for relatively nearby systems. These techniques rely on modeling the bulk motions of gas and stars in the vicinity of the BH. The advent of HST and its superior angular resolution led to a burst in BH detections and mass measurements. There exist a variety of approaches to modeling (detailed descriptions

are given in reviews by (Ferrarese & Ford 2005; Kormendy & Ho 2013). The current state-of-the-art technique is Schwarzschild modeling (Schwarzschild 1979; see also Gebhardt et al. 2000b, 2003; Valluri et al. 2004). This approach involves creating a library of stellar orbits, and determining which superposition of orbits best reproduces surface brightness (photometry) and kinematics of the galaxy. This in turn gives a measurement of the BH mass, stellar mass-to-light ratio, as well as the dark matter mass, and can take into account triaxiality (van den Bosch & de Zeeuw 2010; see McConnell et al. 2012; Walsh et al. 2016 for examples).

Stellar and gas dynamical mass measurement techniques generally are used for nearby systems with quiescent BHs. For AGNs, the light from the accreting BH outshines light from the stars in the nearby vicinity, and different techniques must be used to estimate the mass of the BH. Reverberation mapping (Blandford & McKee 1982; Kaspi et al. 2000; Peterson et al. 2004; Bentz et al. 2009) is a BH mass measurement technique used for active galaxies. Specifically, it provides a way to estimate the distance from the central BH/accretion disk to the broad line region. Under the assumption that the gas in the broad line region is photoionized by photons from the accretion disk, one can observe changes in the emission from broad line region in response to fluctuations in the accretion disk continuum emission. For example, if the accretion disk suddenly emits more photons, increased emission will be observed from the broad line region some time later. By tracking changes in the accretion disk emission and broad line region emission over time, one can measure the time lag between the two. Since the speed of light is known, the time lag can be converted into a distance from the accretion disk to the broad line region. The velocity of gas in the broad line region is estimated from emission line widths. The distance to the broad line region and velocity of the broad line region gas are then used to compute a BH mass. However, there are several note-worthy assumptions that go into this mass

estimate. First, it is assumed that the gas in the broad line region is virialized, such that $M_{\rm BH} = f R_{\rm BLR} \Delta V^2 / G$, where $R_{\rm BLR}$ is the radius to the broad line region and f is a scale factor dependent on the geometry of the system. Since it is not possible to determine the precise geometry, f is determined by calibrating reverberation-mapped BH masses against the local $M_{\rm BH} - \sigma_*$ relation.

Correlations have also been found between the $R_{\rm BLR}$ (as measured by reverberation mapping) and other quanitites. For example, the radius of the broad line region is found to correlate with the AGN luminosity (Kaspi et al. 2000; Bentz et al. 2009, 2013). This is useful as it allows one to estimate the broad line region radius without long-term monitoring. It is even possible to obtain a BH mass estimate using the broad Hα line alone, by using broad Hα luminosity as a proxy for radius, and the width of broad Hα as a characteristic velocity of gas in the broad line region (Greene & Ho 2005b; Reines et al. 2013). Uncertainties on BH masses estimated in this way are often large, i.e., a factor of 2-3.

1.3 Supermassive black hole formation

1.3.1 Seed formation mechanisms

A major open question in astrophysics is related to the mechanism by which the first BHs formed in the early universe. The existence of high redshift quasars with large BH masses raises the question of how the universe forms/grows BHs of such masses in a relatively short period of time. For example, Mortlock et al. (2011) reports on a quasar with $M_{\rm BH} = 2 \times 10^9 M_\odot$ at $z = 7.085$, corresponding to just 750 million years after the Big Bang. Do BHs begin small and accrete at prodigious rates? Or do they start their lives relatively massive? Models for the formation of BH seed tend to fall into two categories: "light seeds" and "heavy seeds". There exist several extensive reviews of BH seed formation (e.g., Volonteri 2010; Latif & Ferrara 2016); here I briefly describe different formation

models and discuss observations which may help illuminate the primary formation mechanism.

Light seed models suggest that BH seeds form from the deaths of Population III stars (Madau & Rees 2001; Heger et al. 2003; Alvarez et al. 2009). Population III stars comprise the first generation of stars; because of the very low metallicity of gas clouds in the early universe, gas did not cool as efficiently as in the present day universe (Abel et al. 2002). Thus, clumps could grow to much bigger masses before collapsing, producing very massive stars. These stars in turn would produce BHs with larger initial masses than present-day stars are capable of producing. Seeds formed via the deaths of Population III stars are expected to be ~ 100 solar masses. However, there are still many open questions relating to this formation mechanism. For instance, the initial mass function of Population III stars remains uncertain; the final star masses depend on many factors such as disk fragmentation, accretion rate, and feedback from UV photons. Some simulations suggest that due to photoevaporation of the protostellar accretion disk, Population III stars may actually only reach $\sim 40 - 50\ M_{\odot}$ (Hosokawa et al. 2011). However, others show that sufficiently high accretion rates should be able to produce stars with masses in excess of $100\ M_{\odot}$ (Hirano et al. 2014). It is worth noting that light seed models require super-Eddington accretion in order to grow BHs to the masses observed in high redshift quasars in the requisite time (Madau et al. 2014).

Heavy seed models propose that BH seeds of $10^{4-5} M_{\odot}$ form from the direct collapse of very massive gas clouds (Loeb & Rasio 1994; Bromm & Loeb 2003; Begelman et al. 2006). Direct collapse BHs are attractive in that they provide a more straightforward way of obtaining $10^9\ M_{\odot}$ quasars by $z \approx 7$ without invoking super-Eddington accretion. In the direct collapse scenario, large amounts of gas inflow to the center of a halo, where the cloud collapses into a BH without fragmenting and forming stars. To obtain sufficiently

high accretion rates without invoking dynamical processes such as bars or mergers, the gas must remain warm, which requires metal free halos (Lodato & Natarajan 2006; Ferrara et al. 2014). While observational work suggests that metal-free gas structures can exist to redshift $z \sim 7$ (e.g., Simcoe et al. 2012), there are still complications. For instance, the accreting gas cloud needs to remain warm and therefore must be irradiated (Agarwal et al. 2016; Schauer et al. 2017) while simultaneously avoiding pollution from supernovae winds following the deaths of nearby stars (Dijkstra et al. 2014). It has also been suggested that the formation of direct collapse BHs could be facilitated by supermassive stars with masses in excess of $1000\ M_{\odot}$ (Begelman 2010; Volonteri & Begelman 2010; Chon & Latif 2017). This scenario requires sufficiently high accretion rates such that the accretion time scale is shorter than the contraction timescale.

There is also a third BH seed formation pathway which produces "intermediate-mass" seeds ($\sim 10^3 M_{\odot}$) involving collisions of stellar mass objects in dense stellar environments (e.g., Portegies Zwart et al. 2004; Freitag et al. 2006). In particular, dense, massive nuclear star clusters (NSCs) have been proposed as potential birthplaces for BH seeds (Miller & Lauburg 2009; Davies et al. 2011; Neumayer & Walcher 2012). NSCs are found in the cores of most galaxies with $M_* \lesssim 10^{10} M_{\odot}$ (Côté et al. 2006, 2007). They have typical stellar masses of $10^{5-7} M_{\odot}$ and effective radii of just a few parsecs, making them the densest known stellar environments in the universe (Böker et al. 2002, 2004; Ferrarese et al. 2006; Georgiev & Böker 2014). Merritt (2009) show that BHs with intermediate masses can form in young star clusters at high redshift; unlike some of the previous seed formation mechanisms discussed, Merritt (2009) assume mild pollution from metals. BHs can also form in NSCs at intermediate or low redshifts. Miller & Davies (2012) suggest that any relaxed stellar systems with velocity dispersions $\gtrsim 40\,\mathrm{km\,s^{-1}}$ will necessarily collapse and form a BH, since heating from binaries will not be sufficient to support the

cluster. More recently, Stone et al. (2017) found that NSCs with sufficiently high velocity dispersions and densities can form BHs via a runaway tidal capture process in less than a Hubble time.

1.3.2 Observational tests of BH formation theories

We do not currently possess the technological capabilities to observe the formation of the first BHs at high redshift. However, theoretical work suggests that clues to the formation of BH seeds can be found in the smallest galaxies at present day (see recent review by Reines et al. 2016). In particular, the occupation fraction, i.e., the fraction of galaxies containing central BHs, is expected to be sensitive to the dominant seed formation mechanism. While virtually all galaxies with stellar masses above $\sim 10^{10}\ M_{\odot}$ contain a central BH regardless of the seed formation mechanism, the occupation fraction for lower-mass systems may differ. Volonteri et al. (2008) find that for heavy seed formation models, a large fraction of low-mass halos end up without a central BH. However, if seeds primarily form via the deaths of Population III stars, the occupation fraction of low-mass halos is expected to be relatively higher (see also Volonteri 2010; Greene 2012).

In practice, the occupation fraction is difficult to measure, because it is typically not possible to strictly rule out the presence of a central BH. There are a few cases where a dynamical constraints can be placed on the mass of a central BH. For example, the dwarf elliptical galaxy NGC 205 has a BH mass upper limit of $\sim 3 \times 10^4\ M_{\odot}$ (Valluri et al. 2005). The bulgeless Local Group spiral galaxy M33 has a BH mass upper limit of $3000\ M_{\odot}$ Merritt et al. (2001). However, both M33 and NGC 205 are ~ 1 Mpc away; such stringent upper limits cannot be placed on systems outside the Local Group.

While the occupation fraction is not feasible to measure directly, we can measure the active fraction, or the fraction of galaxies with an accreting BH (down to a chosen luminosity threshold). One can then attempt to infer the occupation fraction from the active

fraction. Recently, Miller et al. (2015) placed constraints on the occupation fraction using *Chandra X-ray Observatory* observations. They search for nuclear X-ray emission in a sample of ~ 200 nearby, early-type galaxies down to a luminosity limit of $\log L_X = 38.3$ $\mathrm{erg\ s^{-1}}$. They next simultaneously fit for the occupation fraction and the scaling between nuclear X-ray luminosity and stellar mass. In the end, they constrain the occupation fraction for low-mass early type galaxies ($M_* < 10^{10} M_\odot$) to be $> 20\%$. This constraint can be improved upon by expanding the total sample size.

An additional observational test of seed formation mechanisms relies on scaling relations. The low-mass end of the $\mathrm{M_{BH}}$-σ_* relation is also expected to be sensitive to the dominant seed formation mechanism (Volonteri & Natarajan 2009). While the high-mass end of the relation is established early, lower-mass systems evolve onto it over time. If BH seeds formed via the heavy seed models, then BHs are initially over-massive with respect to the relation. Thus, we would observe a plume of objects above $\mathrm{M_{BH}}$-σ_* at the low-mass end at $z = 0$. However, if BHs form via light seeds, we expect to see low-mass systems scattering below the $\mathrm{M_{BH}}$-σ_* relation.

1.4 Dwarf galaxies with AGN signatures

As discussed above, the population and properties of BHs in the smallest galaxies have the potential to inform models of BH formation and growth over cosmic time. Thus, it is desirable to search for and characterize BHs in dwarf galaxies. Unfortunately, BHs in dwarf galaxies are relatively low-mass compared to BHs in larger galaxies and are more difficult to detect. For reference, a BH weighing $10^5 M_\odot$ will have a gravitational sphere of influence of $\mathrm{GM_{BH}}/\sigma^2 \sim 1\mathrm{pc}$. This is unresolvable with current technology for galaxies outside the Local Group of galaxies. Thus, stellar and gas dynamical methods are largely infeasible for identifying BHs in dwarf galaxies. Instead, we search for signatures of BH

accretion to find such systems.

The first dwarf galaxies identified to contain active galactic nuclei were NGC 4395 (Filippenko & Sargent 1989; Filippenko & Ho 2003; Moran et al. 2005; O'Neill et al. 2006; den Brok et al. 2015) and POX 52 (Kunth et al. 1987; Barth et al. 2004; Thornton et al. 2008). Both NGC 4395 and POX 52 were classified as AGNs due to the presence of bright optical emission lines with relative strengths characteristic of photoionization by an AGN. Both systems were serendipitous discoveries, and were the only known dwarf galaxies with AGNs for more than a decade.

Large-scale astronomical surveys with publicly available data are responsible for the recent advances in the field of AGNs in dwarf galaxies. The Sloan Digital Sky Survey (SDSS; York et al. 2000) has been particularly revolutionary. The SDSS has been collecting imaging and spectroscopic data of celestial objects since 2000 with a dedicated 2.5m telescope at Apache Point Observatory. In all, SDSS has collected spectroscopic observations of roughly 1 million galaxies. The first work using SDSS data to search specifically for low-mass BHs was Greene & Ho (2004). They searched the SDSS for galaxies with broad $H\alpha$ emission lines indicative of BHs with masses $M_{\rm BH} < 10^6\ M_{\odot}$. Greene & Ho (2004) presented 19 galaxies with BHs ranging in stellar mass from $\sim\ 10^5 - 10^6 M_{\odot}$; Greene & Ho (2007) presented an expanded sample of 174 objects. While most of the host galaxies were not dwarf galaxies, these works demonstrated that galaxies do contain BHs in this mass regime, and that galaxies do not require classical bulges to host a central BH (Greene & Ho 2007; Greene et al. 2008; Jiang et al. 2011b).

The first work to focus specifically on AGNs in dwarf galaxies was Reines et al. (2013). Using the NASA-Sloan Atlas (Aihara et al. 2011), Reines et al. (2013) searched for narrow or broad optical emission line signatures of AGNs in a sample of more than 25,000 nearby ($z < 0.055$) dwarf galaxies. Specifically, they identified 136 galaxies with narrow-

emission line ratios indicative of photoionization at least partly due to an AGN; 10 of these galaxies also had broad Hα emission from which BH masses could be estimated. Additionally, they identified 15 galaxies with broad Hα but with narrow emission lines dominated by star formation. This work represented an order of magnitude increase in the number of dwarf galaxies known to contain AGNs. Several other studies have since successfully identified AGNs in dwarf galaxies using optical spectroscopic signatures (Moran et al. 2014; Sartori et al. 2015).

AGNs in dwarf galaxies have also been detected by searching for X-ray emission. The first dwarf starbursting galaxy found to contain an AGN was Henize 2-10 Reines et al. (2011), based on spatially coincident X-ray and radio emission (Reines & Deller 2012; Reines et al. 2016). Lemons et al. (2015) cross-matched the Reines et al. (2013) parent sample ($\sim 45,000$ dwarf galaxies) with the Chandra Source Catalog and found 8 systems with nuclear hard X-ray emission at levels higher than expected from low-mass and high-mass X-ray binaries. X-ray searches can also extend to higher redshift than optical searches. Pardo et al. (2016) searched for X-ray emission in dwarf galaxies out to $z \sim 1$, identifying 10 systems (out of a sample of 605) with X-ray emission consistent with an AGN. They estimate an AGN fraction of $\sim 1\%$ for their sample of dwarf galaxies. Mezcua et al. (2016) carried out a stacking analysis of dwarf galaxies in the COSMOS field out to $z = 1.5$. They found an excess of X-ray emission which is attributed to a population of accreting BHs, after taking into account expected contributions from low-mass and high-mass X-ray binaries and X-ray emission from hot gas. Most recently, Chen et al. (2017) found 10 AGNs in low-mass galaxies from the NuSTAR serendipitous survey, which can probe hard X-ray emission up to 24 keV.

Attempts have been made to identify AGNs in dwarf galaxies using mid-IR colors Sartori et al. (2015). Such selection methods have been successful for more massive AGNs

(Stern et al. 2012), since AGNs can heat dust, producing red mid-IR colors. However, very red mid-IR colors can also be produced by extreme star formation. Thus, this method cannot be used alone to select AGNs in samples of dwarf galaxies Hainline et al. (2016)

It is worth noting that BHs have been dynamically detected in the centers of ultra compact dwarf galaxies (UCDs) in the Virgo Cluster (distance ~ 16.5 Mpc). UCDs are very dense; with masses of up to a few times $10^8 M_\odot$ and half-light radii of tens of parsecs. UCDs tend to exist in galaxy cluster environments. A recent study of the Virgo Cluster UCD M60-UCD1 revealed the presence of a BH with $M_{\rm BH} = 2.1 \times 10^7 M_\odot$, corresponding to 15% of the galaxy mass (Seth et al. 2014). Since then, BHs have been discovered in two other Virgo UCDs, both with masses of a few times $10^6 M_\odot$ Ahn et al. (2017). Since these BHs weigh such a significant fraction of the total galaxy stellar mass, these results lend support to the theory that UCDs are the tidally stripped cores of galaxies that were formerly more massive.

1.5 Thesis contents

The population of dwarf galaxies with AGNs is finally large enough to allow for demographic studies. We can now begin to answer some of the following open questions relating to AGN in dwarf galaxies:

- What are the masses of BHs in the centers of present-day dwarf galaxies?
- What were the masses of the first BH seeds?
- What is the occupation fraction of low-mass galaxies?
- Where do dwarf galaxies with AGNs sit with respect to BH-galaxy scaling relations?
- What is the spectral energy distribution of AGNs in dwarf galaxies?
- Does environment effect the presence of AGNs in dwarf galaxies?
- What impact do AGNs have on star formation in dwarf galaxies?

This thesis represents a first step towards answering the questions posed above. In particular, this thesis reports on detailed follow-up of the Reines et al. (2013) catalog with the goal of answering targeted questions about the nature of dwarf galaxies with AGN signatures. The following chapters detail multi-wavelength observations of dwarf galaxies with AGN signatures identified in Reines et al. (2013). Chapter 2 discusses multi-epoch spectroscopy of a sub-sample of dwarf galaxies from Reines et al. (2013). Chapter 3 focuses on one particular object from that sub-sample, which was found to host a $50,000\ M_{\odot}$ BH in its core. Chapter 4 presents X-ray and UV observations of dwarf galaxies with AGNs and discuss the accretion properties of these systems. Future directions are discussed in Chapter 5.

CHAPTER II

Multi-epoch spectroscopy of dwarf galaxies with optical AGN signatures

2.1 Motivations and Aims

This chapter describes multi-epoch spectroscopic observations of a subsample of dwarf galaxies with optical spectroscopic AGN signatures in the SDSS from Reines et al. (2013) and is based on work published in Baldassare et al. (2016). Follow-up spectroscopy was obtained for 28 total galaxies with broad and/or narrow-line of AGN activity in their SDSS spectroscopy. Certain narrow emission line ratios indicate photoionization by an AGN, while broad emission lines can be characteristic of dense gas orbiting around the BH, and can be used to estimate BH masses. However, the broad emission line widths measured in SDSS are such that they are also consistent with being generated by transient stellar processes such as Type II Supernovae. Our goals for this work were two-fold:

- For objects with **broad emission lines** in SDSS, determine whether the broad emission is persistent/consistent in follow-up spectroscopy. If the broad emission is generated by transient stellar processes, it will fade on timescales of several years and will not be present in follow-up observations.
- For objects with **narrow emission line** AGN signatures in SDSS, search for faint broad emission not detectable with SDSS, and measure host stellar velocity dispersions in order to determine where objects sit with respect to the $M_{BH} - \sigma_*$ relation.

Our follow-up spectroscopy shows that broad emission in star-forming dwarf galaxies (those with narrow-lines indicating photoionization by star forming regions as opposed to AGN) fades on timescales of 5-10 years, indicating that it was due to transient stellar processes. However, broad emission in objects which also have narrow-line AGN evidence is persistent and consistent, suggesting it is emission from gas orbiting around the BH. We present stellar velocity dispersions for 15 objects with narrow-line AGN evidence, and clearly detect broad emission in one new system: RGG 118. Results for RGG 118 were published separately in Baldassare et al. (2015) (see Chapter 3).

2.2 Introduction

While massive black holes (BHs; here defined as $\mathrm{M_{BH}} \gtrsim 10^{4-5}\ M_{\odot}$) are ubiquitous in the centers of galaxies of Milky Way mass and larger (Magorrian et al. 1998), little is known about the occurrence rate and properties of BHs in dwarf galaxies (i.e., galaxies with $\mathrm{M}_{\star} \lesssim 10^{9.5}\ M_{\odot}$). Studying the population of BHs in dwarf galaxies is useful for understanding BH formation and growth in the early universe. Having had relatively quiet merger histories, their BHs may have masses similar to their "birth" mass (e.g., Volonteri 2010; Bellovary et al. 2011).

Clues to the formation of BH seeds may reside in the well studied relation between BH mass and stellar velocity dispersion (see e.g., Ferrarese & Merritt 2000; Gebhardt et al. 2000a; Gültekin et al. 2009). Using semi-analytic modeling, Volonteri & Natarajan (2009) find that, while the relationship between BH mass and velocity dispersion (or the $\mathrm{M}_{BH} - \sigma$ relation) is in place by $z \sim 4$ for massive halos, systems with lower mass BHs ($\mathrm{M}_{BH} < 10^{6}\ M_{\odot}$) evolve onto it at later times. If BH seeds form "light" ($\sim 10^{2} M_{\odot}$; the remnants of Population III stars, see e.g., Madau & Rees 2001; Alvarez et al. 2009; Madau et al. 2014), then BHs begin as undermassive with respect to the local $\mathrm{M}_{BH} - \sigma_{\star}$

relation, and will evolve towards it from below. Alternatively, if BH seeds form "heavy" ($10^{4-5} M_{\odot}$; through direct collapse of gas clouds, e.g., Begelman et al. 2006; Lodato & Natarajan 2006), then BHs are initially overmassive and systems evolve rightwards onto the relation (i.e., towards higher velocity dispersions) as the host galaxies grow through mergers. The smallest $z = 0$ halos ($\sigma_{\star} \sim 20 - 50$ km s^{-1}) have not yet undergone major mergers, and thus may be present-day outliers on the local $M_{BH} - \sigma_{\star}$ relation.

Finding and weighing relatively low-mass BHs is difficult due to the small gravitational sphere of influence of the BH, which is typically $\lesssim 1$ parsec for $M_{BH} \sim 10^5\ M_{\odot}$. Thus, in order to identify BHs in dwarf galaxies outside the Local Group, it is necessary to look for signs of BH activity (i.e., active galactic nuclei, or AGN). Large-scale surveys such as the Sloan Digital Sky Survey (SDSS) have made it possible to search for signatures of AGN in samples comprised of tens of thousands of galaxies. Early work by Greene & Ho (2004) (see also Greene & Ho 2007), identified galaxies in the SDSS with low-mass AGN by searching for broad Hα emission, which can be produced by virialized gas near the central BH. These studies identified ~ 200 low-mass AGN candidates with a median BH mass of $\sim 10^6\ M_{\odot}$.

More recent studies have pushed the search for low-mass AGN into the dwarf galaxy regime. X-ray and radio observations led to the discovery of AGN in the dwarf starburst galaxy Henize 2-10 (Reines et al. 2011; Reines & Deller 2012), and in the dwarf galaxy pair Mrk 709 (Reines et al. 2014). Optical spectroscopic observations revealed the well-studied AGN in NGC 4395 (Filippenko & Sargent 1989; Filippenko & Ho 2003) and POX 52 (Barth et al. 2004), and more recently led to the discovery of a BH with a mass in the range of $27,000 - 62,000\ M_{\odot}$ in the dwarf galaxy RGG 118 (Baldassare et al. 2015). Additionally, multiwavelength studies using large samples of *bona fide* dwarf galaxies have produced a collective sample of hundreds of AGN candidates in dwarf galaxies (Reines

et al. 2013; Moran et al. 2014; Lemons et al. 2015; Sartori et al. 2015; Pardo et al. 2016).

Reines et al. 2013 (hereafter R13) searched for dwarf galaxies with spectroscopic signatures of AGN activity based on their narrow and/or broad emission lines. Out of $\sim 25,000$ nearby ($z \leq 0.055$; D $\lesssim 250$ Mpc) dwarf galaxies in the SDSS, they identified 136 galaxies with narrow-line ratios indicating photoionization at least partly due to an AGN based on the BPT (Baldwin, Phillips & Terlevich 1981) diagram, i.e., they were classified as either AGN or AGN/star-forming composites (see also Kewley et al. 2001; Kauffmann et al. 2003; Kewley et al. 2006). A fraction of these also had broad Hα emission. Additionally, R13 identified 15 galaxies with broad Hα emission in their SDSS spectroscopy (FWHM ranging from $\sim 600 - 3700$ km s^{-1}), but with narrow-line ratios that placed them in the star forming region of the BPT diagram. We are particularly concerned with the origin of the broad emission in these systems.

Broad Balmer emission with FWHM up to several thousand kilometers per second can be produced by stellar processes such as Type II supernovae (Filippenko 1997; Pritchard et al. 2012), luminous blue variables (Smith et al. 2011a), or Wolf-Rayet stars. Follow-up spectroscopy, taken over a sufficiently long baseline, can help distinguish between an AGN and one of the aforementioned transient stellar phenomena.

Here, we present follow-up optical spectroscopic observations of 14 of the 15 BPT star forming galaxies with broad Hα presented in R13, as well as observations of ten BPT AGN (one with broad Hα) and three BPT composites (one with broad Hα). Follow-up observations for RGG 118 – the current record holder for the lowest-mass BH in a galaxy nucleus – were presented separately in Baldassare et al. (2015). The goals of this work are two-fold. First, for our targets which were identified by R13 to have broad Hα emission (broader than narrow lines such as [SII]$\lambda\lambda$6713,6731) with FWHM > 500 km s^{-1}, we analyze their spectra and determine whether the broad Hα emission is still present and con-

sistent with previous observations. Second, for galaxies with sufficiently high-resolution follow-up spectroscopy, we measure stellar velocity dispersions.

In Section 2.3, we describe our observations and data reduction procedures. In Section 2.4, we discuss our emission line fitting analysis and report stellar velocity dispersion measurements for objects with sufficiently high spectral resolution data. In Section 2.5, we present results from the follow-up spectroscopy for the broad line objects.

2.3 Observations and Data Reduction

The sample analyzed here is comprised of 27 total targets. Of these, 16 comprise our "SDSS broad Hα sample" or galaxies identified to have broad Hα emission in their SDSS spectroscopy. In the SDSS broad Hα sample, 14 objects are BPT star forming, 1 is a BPT composite and 1 is a BPT AGN. Additionally, we have follow-up observations for 11 objects (9 BPT AGN and 2 BPT composites) that did not have broad Hα emission in their SDSS spectroscopy. In addition to the SDSS observations, each galaxy has one or two follow-up spectroscopic observations taken between 5 and 14 years after the SDSS spectrum. Below, we outline our observations and data reduction procedures for each instrument used. See Table 2.1 for a summary of our sample and observations. All spectra were corrected for Galactic extinction.

Table 2.1 Summary of Observations

R13 ID	NSAID	SDSS Name	z	R13 BPT class	SDSS obs.	DIS obs.	MagE obs.	OSMOS obs.
6	105376	J084025.54+181858.9	0.0150	AGN	2005-12-07	–	2013-04-20	–
9	**10779**	J090613.75+561015.5	0.0466	AGN	2000-12-30	2013-03-15	–	–
16	30370	J111319.23+044425.1	0.0265	AGN	2002-02-21	–	2013-04-19	–
22	77431	J130434.92+075505.0	0.0480	AGN	2008-02-08	–	2013-04-20	–
27	78568	J140228.72+091856.4	0.0191	AGN	2007-03-16	–	2013-04-19	–
28	70907	J140510.39+114616.9	0.0174	AGN	2006-03-05	–	2013-04-19	–
29	71023	J141208.47+102953.8	0.0326	AGN	2006-04-23	–	2013-04-20	–
31	71565	J143523.42+100704.2	0.0312	AGN	2005-06-14	–	2013-04-20	–
33	120870	J144712.80+133939.2	0.0323	AGN	2007-05-22	–	2013-04-20	–
34	124249	J153941.68+171421.8	0.0458	AGN	2008-04-07	–	2013-04-20	–
118	166155	J152303.80+114546.0	0.0234	Composite	2007-05-14	–	2013-04-20	–
119	**79874**	J152637.36+065941.6	0.0384	Composite	2008-03-15	2013-03-15	2013-04-19	–
120	72952	J152913.46+083010.6	0.0430	Composite	2006-06-19	–	2013-04-20	–
128	73346	J160544.57+085043.9	0.0154	Composite	2004-08-11	–	2013-04-19/20	–
B	**15952**	J084029.91+470710.4	0.0421	SF	2001-03-13	2013-02-09	–	2015-01-20
C	**109990**	J090019.66+171736.9	0.0288	SF	2006-11-13	2013-02-16	–	2014-02-02
D	**76788**	J091122.24+615245.5	0.0266	SF	2007-12-16	–	–	2015-01-21
E	**109016**	J101440.21+192448.9	0.0289	SF	2006-02-02	–	2013-04-19	2015-01-20
F	**12793**	J105100.64+655940.7	0.0325	SF	2001-01-20	–	–	2015-01-22
G	**13496**	J105447.88+025652.4	0.0222	SF	2002-03-20	–	2013-04-20	–
H	**74914**	J111548.27+150017.7	0.0501	SF	2005-01-09	–	2013-04-19	–
I	**112250**	J112315.75+240205.1	0.0250	SF	2007-02-23	2013-03-15	–	2015-01-23
J	**41331**	J114343.77+550019.4	0.0272	SF	2003-04-05	2013-02-16	–	–
K	**91579**	J120325.66+330846.1	0.0349	SF	2005-05-08	2013-03-15	–	2015-01-21
L	**33207**	J130724.64+523715.5	0.0262	SF	2002-04-12	2013-02-16	–	–
M	**119311**	J131503.77+223522.7	0.0230	SF	2008-02-11	2013-02-16	–	2014-02-02
N	**88972**	J131603.91+292254.0	0.0378	SF	2006-06-18	–	–	2015-01-20
O	**104565**	J134332.09+253157.7	0.0287	SF	2006-02-01	–	–	2015-01-22

Notes. Summary of our spectroscopic observations. The first column gives the ID assigned in Reines et al. (2013), the second gives the NASA-Sloan Atlas ID, and the third column gives the SDSS designation. Redshift is given in the fourth column, and the fifth column gives the region of the BPT diagram in which the object fell in R13 based on analysis of the SDSS spectrum. The remaining four columns give the dates of observations for SDSS, DIS, MagE, and MDM when applicable. The R13 ID and NSAID for objects in the SDSS broad Hα sample are shown in bold. Note that observations for RGG 118 were presented in a prior work (Baldassare et al. 2015).

Clay/MagE.

We observed 16 targets (including RGG 118) with the Magellan Echellette Spectrograph (MagE; Marshall et al. 2008). MagE is a moderate-resolution (R=4100) spectrograph on the 6.5m Clay Telescope at Las Campanas Observatory. Data were collected on the nights of 2013 April 18-19 using a $1''$ slit. Spectral coverage spans roughly from 3200 Å to 10000 Å across 15 orders. Seeing was measured to be $0.5''$-$1.2''$ over the two nights. Total exposure times per object ranged from 1800 to 4800s. A thorium argon arc lamp was observed for wavelength calibration, and the flux standard θ Crt was observed for flux calibration. Flux calibrated reference spectra were obtained from the European Southern Observatory library of spectrophotometric standards.

Flat fielding, sky subtraction, extraction, wavelength calibration, and flux calibration were performed with the mage_reduce pipeline written by George Becker.[1] One-dimensional spectra were extracted with a $3''$ aperture (the larger signal within $3''$was useful for determining stellar velocity dispersions; see Section 2.4.2).

APO/DIS.

Eight targets were observed with the Dual Imaging Spectrograph (DIS[2]) on the 3.5m Astrophysical Research Consortium telescope at Apache Point Observatory. Observations were taken using a $1.5''$ slit. DIS consists of a red channel and a blue channel, with a transition wavelength of ~ 5350Å. We used the B1200 and R1200 gratings (R=1200), which give linear dispersions of 0.62 Å/pix for the blue channel and 0.58 Å/pix for the red channel. DIS targets were observed on the nights of 2013 February 9, 2013 February 16, and 2013 March 15. Each object had three exposures with individual exposure times of 1200s. A Helium-Neon-Argon lamp was observed for wavelength calibration, and standard stars

[1]The mage_reduce reduction pipeline is available for download at: ftp://ftp.ociw.edu/pub/gdb/mage_reduce/mage_reduce.tar.gz
[2]http://www.astro.princeton.edu/∼rhl/dis.html

Feige 34 and Feige 66 were observed for flux calibration. The flux calibrated reference spectra were obtained from the *Hubble Space Telescope* CALSPEC Calibration Database.

Reductions for the two-dimensional images, as well as extraction of the one-dimensional spectra and wavelength calibration were done using standard longslit reduction procedures in *IRAF*[3] following Massey et al. 1992 and Massey 1997.

MDM/OSMOS.

We observed ten targets with the Ohio State Multi-Object Spectrograph (OSMOS; Martini et al. 2011) on the MDM Observatory 2.4 Hiltner Telescope on 2 February 2014 and 20-23 January 2015. For each target, we used a $1.2''$ by $20'$ slit, with a VPH grism ($R = 1600$, or 0.7 Å / pixel), which covered an observed wavelength range of $3900 - 6900$ Å . The seeing was measured to be $0.8''$-$1.1''$ for the February 2 observation, and between $0.8''$-$1.8''$ for the January 20-23 observations. Each object was observed with multiple exposures of 1800s. For wavelength calibration, we observed an Argon arc lamp, and for flux calibration, we observed the spectrophotometric standards Feige 34 and Feige 66.

The data were reduced following standard *IRAF* routines from the *longslit* package, including bias and dark subtraction, flat fielding, wavelength calibration, and telluric and background subtraction. One-dimensional spectra were then extracted using a $\sim 3''$ aperture along the slit, and corrected for heliocentric velocity.

SDSS.

For purposes of comparison, we also make use of the SDSS observations of the galaxies in our sample. The objects were originally selected by R13 by analyzing SDSS spectroscopy of $\sim 25,000$ dwarf emission line galaxies in the NASA-Sloan Atlas [4].

[3] *IRAF* is distributed by the National Optical Astronomy Observatory, which is operated by the Associate of Universities for Research in Astronomy (AURA) under cooperative agreement with the National Science Foundation.

[4] http://www.nsatlas.org

2.4 Analysis

2.4.1 Emission line modeling

For each galaxy, we modeled the Hα-[NII] complex in order to ascertain whether broad Hα emission was present. We summarize the general procedure here, though more thorough discussions can be found in R13 and Baldassare et al. (2015). In this work, we are mainly interested in whether a broad Hα emission line is present. Thus, we simply fit the continuum as a line across the region surrounding the Hα-[NII] complex. This also ensures that we do not artificially introduce a broad line by over-subtracting an absorption feature. We then create a model for the narrow-line emission using an intrinsically narrow-line (e.g., [SII]$\lambda\lambda$ 6713,6731; forbidden lines are guaranteed not to be produced in the dense broad line region gas). We use the narrow-line model to fit the narrow Hα emission and the [NII] lines simultaneously. The width of the narrow Hα line is allowed to increase by up to 25%. The relative amplitudes of the [NII] lines are fixed to their laboratory values. We next add an additional Gaussian component to the model to represent broad Hα emission. If the preferred FWHM for the component is $> 500\,\mathrm{km\,s^{-1}}$ and the χ^2_ν is improved by at least 20%, then we classify the galaxy as having persistent broad Hα emission (Hao et al. 2005; R13). As noted in R13, this threshold is somewhat arbitrary, but found to be empirically suitable for this work. If the broad model is preferred, we attempt to add an additional broad component, effectively allowing the broad emission to be modeled with up to two Gaussians. Once we have our best-fit model (i.e., adding additional components no longer improves the χ^2_ν by our threshold value), we measure the FWHM and luminosity of broad Hα, if present. We model and measure emission line fluxes for Hβ and [OIII] λ5007. Below, we discuss the narrow-line models used for each instrument.

Narrow-line models

MagE: For the MagE spectra, we follow R13 and model the narrow-line emission by fitting Gaussian profiles to the [SII] $\lambda\lambda$6713,6731 doublet. In our modeling, the two lines are required to have the same width.

OSMOS: The wavelength coverage of the OSMOS spectra does not extend to the [SII] doublet, so here we model the narrow emission with the [OIII] λ5007 line. The profile of [OIII] often has a core component and a wing component (Heckman et al. 1981; De Robertis & Osterbrock 1984; Whittle 1985; Greene & Ho 2005a; Mullaney et al. 2013; Zakamska & Greene 2014). We therefore fit the [OIII] line with two components if the addition of a second component improves the χ^2_ν by at least 20%. If [OIII] is indeed best fit with both a core and wing component, then we use the width of the core component for our narrow-line model. If it is instead best fit with a single component, we retain the width of the single component for our narrow-line model. In order to determine whether the use of [OIII] as our narrow line would affect our fits to the Hα-[NII] complex, we compared the profiles of [SII] and [OIII] in the SDSS spectra for our OSMOS targets. We find that, for a given object, the FWHMs of the [OIII] and [SII] lines differ by very little, with percent differences in FWHM ranging from 0.3 to 11%. Since we allow the width of the Hα narrow line to increase by up to 25%, we do not expect this choice of narrow line to affect our results.

DIS: For the DIS spectra, we also use the [SII] lines to model the narrow-line emission. However, the emission lines in the DIS spectra display some additional instrumental broadening, which we observe in the red channel arc lamp spectra (see Figure 2.1). Since this instrumental broadening is not visible in low S/N [SII] lines but can still affect the fit to

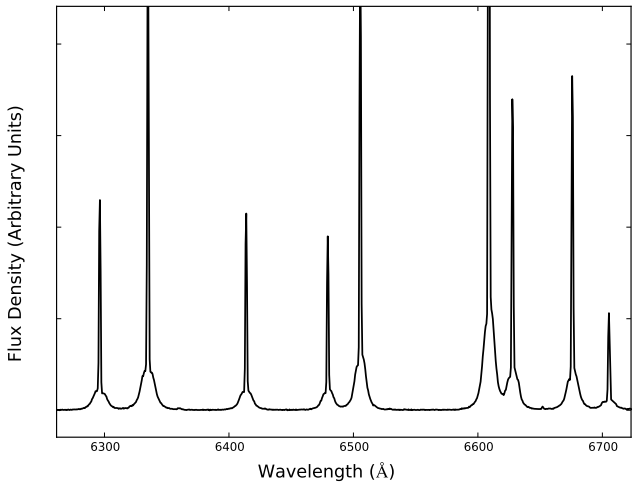

Figure 2.1 Red channel He-Ne-Ar arc lamp spectrum taken as part of our observations with the Dual-Imaging Spectrograph on the ARC 3.5m telescope. Note that the shape of the instrumental broadening has two components – a narrow core and a broad base.

Hα, we created a basic model for the narrow-line emission to use in fitting the [SII] lines. Using the galaxy spectrum for which the [SII] lines had the most flux, we generated a narrow-line model consisting of two Gaussians with fixed relative amplitudes and widths. This basic shape was then used to model [SII] lines in all other DIS galaxy spectra, and correspondingly, their narrow Hα and [NII] lines. Figure 2.2 shows the [SII] lines from a representative DIS spectrum.

Given the instrumental broad component seen in the emission lines, we tested the degree to which the narrow-line model affects the presence/properties of broad Hα emission to ensure that our results were not influenced by this broadening. To do this, we created two additional narrow-line models: one where the instrumental broadening is less prevalent (i.e., we reduced the relative width and relative amplitude of the "broad" narrow-line component by 10%), and one where it is more prevalent (i.e., the relative width and amplitude are increased by 10%). We then refit the spectra and assessed the security of our broad Hα detections. We found this to have little effect on the FWHM and luminosity of broad Hα for secure detections (i.e., FWHM varied by less than 10%), but to greatly influ-

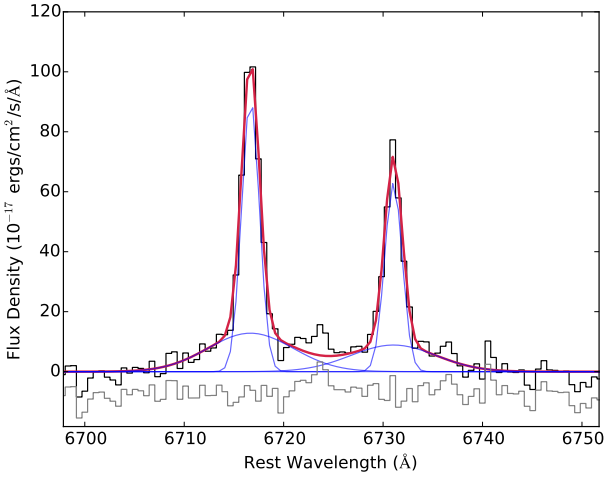

Figure 2.2 [SII]$\lambda\lambda 6716, 6731$ lines from the DIS spectrum of RGG C (NSA 109990). The black line shows the observed spectrum, the red line is our best fit to the two lines, and the solid blue lines show the various components corresponding to our best fit of the two [SII] lines. We constrain the relative heights and widths of the "narrow" and "broad" components and use that model to fit the narrow-lines in the Hα-[NII] complex for DIS observations.

ence these measured quantities for more ambiguous detections (with the FWHM varying by as much as 90% for a slightly different narrow-line model). We err on the side of caution in our classifications; objects which have ambiguous broad Hα detections in their DIS spectra are classified as ambiguous.

2.4.2 Stellar velocity dispersions

We measured stellar velocity dispersions for 15 galaxies with MagE observations using pPXF (Penalized Pixel Fitting; Cappellari & Emsellem 2004). As a reminder, of these, 9 are classified as BPT AGN, 3 are BPT composites, and 3 are BPT star forming galaxies. Four galaxies (1 composite and 3 star forming) overlap with our SDSS broad Hα sample.

PPXF uses a library of stellar templates to fit the stellar continuum and kinematics of a galaxy spectrum. We used a library of 51 stars from the ELODIE spectral database (Prugniel & Soubiran 2001). Our library consists of stars covering spectral classes from O through M and luminosity classes from bright giants to dwarfs (see Table 2.2 for a list of stars and spectral types). The ELODIE spectra span from 3900Å to 6800Å in wavelength

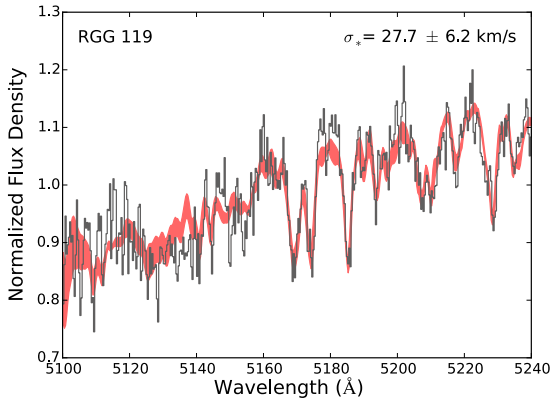

Figure 2.3 Spectral region of the MagE spectrum of RGG 119 used to measure the stellar velocity dispersion in pPXF. We use a region of the spectrum encompassing the Mg *b* triplet. The observed spectrum is shown in gray, while the shaded red region represents the range of outputs from pPXF for the chosen combinations of additive and multiplicative polynomials.

and have a spectral resolution of R=10,000.

We measured stellar velocity dispersions in region of the spectrum surrounding the Mg *b* triplet, spanning from 5100Å to 5250Å(see Figure 2.3). We fit each region using combinations of low-order multiplicative and additive polynomials (orders range from 1 to 4; see e.g., Woo et al. 2010, 2015) , and report the mean value for all measurements. Uncertainties are reported by PPXF for each individual fit (i.e. each combination of multiplicative and additive polynomial). We take the mean for all velocity dispersion measurements and add the errors in quadrature to obtain a velocity dispersion measurement and corresponding error estimate. We measure $\sigma_\star$ values ranging from $28 - 71\,\mathrm{km\,s^{-1}}$ with a median $\sigma_\star$ of $41\,\mathrm{km\,s^{-1}}$. These values correspond to galaxies with NASA-Sloan Atlas stellar masses ranging from $\sim 5 \times 10^8$ to $3 \times 10^9\ M_\odot$. All stellar velocity dispersion measurements are presented in Table 2.3.

2.5 Broad line AGN candidates: Results

We show the locations of all 16 SDSS broad Hα targets on the BPT diagram in Figure 4.1. Based on our follow-up spectroscopy, we classify our targets as having SDSS

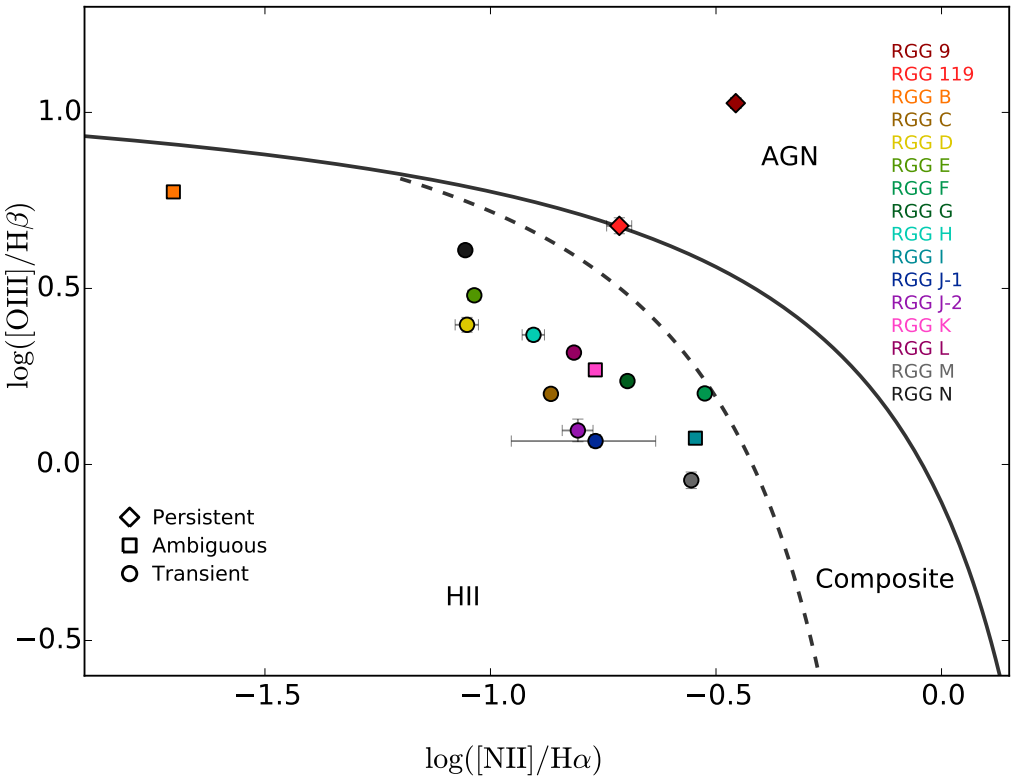

Figure 2.4 Positions of our SDSS broad Hα targets on the BPT diagram (Baldwin et al. 1981) using the classification of Kewley et al. (2006). Each target is plotted in a different color. Note that there are two points for RGG J corresponding to the two SDSS observations. A diamond indicates that broad Hα was present in follow-up spectroscopy ('persistent'), a square indicates an ambiguous follow-up broad Hα detection, and a circle indicates that broad Hα was not detected in follow-up observations ('transient').

broad Hα emission that is: transient (broad Hα is not present in follow-up spectra), persistent (broad Hα is present in follow-up spectroscopy and consistent with prior observations), or ambiguous (state of broad emission is unclear). In the following subsections, we describe our classifications in more detail. Table 2.4 summarizes the results of this analysis. Figures showing examples of fits to Hβ, [OIII], and Hα are given in Section 2.9. See Section 2.7 for a discussion on aperture effects and intrinsic variability as they relate to this work.

Table 2.2 Spectral library

Star	Sp. Type
HD061366	K0III
HD062161	F3V
HD062437	A5IV
HD062968	G8
HD063108	F0
HD064649	G5
HD065123	F7V
HD065604	K5
HD071155	A0Va
HD071557	A0
HD072722	K5
HD073667	K2V
HD079210	M0V
HD090361	A1V
HD042217	K5
HD042250	G9V
HD042548	F0
HD042618	G4V
HD043318	F5V
HD043318	F5V
HD043338	F0
HD044285	K3III
HD044418	G8III
HD044638	K0/1III
HD044770	F5V
HD044771	G8Ib/II
HD046784	M0III
HD047072	Am
HD047309	G0
HD048144	K5
HD048279	O8V+F2V
HD048433	K1III
HD060503	G8III
HD027340	A3IV/V
HD028343	M0.5V
HD028946	G9V
HD029139	K5III
HD029310	G0
HD036395	M1.5V
HD037828	G8III
HD037958	B9III/IV
HD038145	F0V
HD038237	A5IV
HD039833	G3V
HD040573	B9.5V
HD040259	F0V
HD040460	K1III
HD040573	B9.5V
HD040616	G3V
HD041079	K2

Notes. Stars used in our spectral library for stellar velocity dispersion measurements. Spectra were taken from the ELODIE spectral database (Prugniel & Soubiran 2001) and spectral types are taken from the SIMBAD database (Wenger et al. 2000).

Table 2.3 Stellar velocity dispersion measurements

R13 ID	$\sigma_\star$ ($\mathrm{km\,s^{-1}}$)
6	62 ± 12
16	33 ± 5
22	39 ± 6
27	28 ± 6
28	32 ± 4
29	49 ± 7
31	31 ± 4
33	46 ± 5
34	58 ± 3
119	28 ± 6
120	71 ± 8
128	43 ± 5
E	37 ± 12
G	41 ± 13
H	60 ± 11

Notes. Stellar velocity dispersion measurements for objects with MagE data. Stellar velocity dispersions were measured in the Mg b region of the spectrum.

Table 2.4 Broad Hα candidate results

R13 ID	NSAID	R13 $\log L_{\mathrm{H}\alpha}$ (erg s^{-1})	R13 FWHM$_{\mathrm{H}\alpha}$ (km s^{-1})	R13 BPT Class	Follow-up	Δt (years)	Persistent broad Hα?
9	10779	40.15	703	AGN	DIS	13	yes
119	79874	40.16	1043	Comp	DIS, MagE	5	yes
C	109990	40.10	3690	SF	DIS, OSMOS	8	no
D	76788	39.56	4124	SF	OSMOS	8	no
E	109016	39.26	935	SF	MagE, OSMOS	9	no
F	12793	40.09	598	SF	OSMOS	14	no
G	13496	39.56	2027	SF	MagE	11	no
H	74914	39.97	3014	SF	MagE	8	no
J	41331	39.99	1521	SF	DIS	10	no
L	33207	39.51	3126	SF	DIS	11	no
M	119311	39.75	3563	SF	DIS, OSMOS	6	no
N	88972	40.42	645	SF	OSMOS	11	no
O	104565	38.88	1653	SF	OSMOS	9	no
B	15952	40.67	1245	SF	DIS, OSMOS	14	ambiguous
I	112250	39.39	994	SF	DIS, OSMOS	8	ambiguous
K	91579	39.58	774	SF	DIS, OSMOS	10	ambiguous

Notes. Summary of our analysis for the SDSS broad Hα sample. All objects here were observed to have broad Hα in their SDSS spectroscopy in R13. Columns 1 & 2 list the R13 and NASA-Sloan Atlas ID for each object. Columns 3 & 4 list the luminosity and FWHM of the broad emission measured in R13. Column 5 lists the instrument(s) used for the follow-up spectroscopy, and Column 6 lists the time between the SDSS observation and most recent follow-up observation. Column 7 presents the classifications determined in this work.

2.5.1 Transient broad Hα

Out of the 16 objects with SDSS broad Hα, we find 11 to have transient broad Hα emission, i.e., they lacked broad emission in their followup spectroscopic observations (see Figure 2.5 for an example). All 11 fall in the "HII" region of the BPT diagram, which indicates the presence of recent star formation in the galaxy. We note that several objects (e.g., RGG G, RGG F; see Appendix) had additional components in their Hα line models with FWHMs of a few hundred $\mathrm{km\,s^{-1}}$; since these are all narrower than the broad emission in the SDSS spectra and fall below our FWHM cut of $500\,\mathrm{km\,s^{-1}}$, we do not classify those objects as having persistent broad emission. Given the narrow-emission line ratios and host galaxy properties, we consider Type II supernovae (SNe) to be the most likely origin for the transient broad Hα (see Section 2.6 for more details). We note that, as discussed in detail in R13, luminous blue variables (Smith et al. 2011a) and Wolf-Rayet stars can also produce transient broad Hα emission. However, Wolf-Rayet stars typically produce other notable spectral features, such as the Wolf-Rayet bump from λ4650-5690Å. Moreover, their spectra don't typically have strong hydrogen lines (Crowther 2007; Crowther & Walborn 2011). Finally, recent work has revealed the existence of "changing look" quasars, i.e., quasars with broad Balmer emission lines that fade significantly over the course of 5-10 years (see e.g., Runnoe et al. 2016; Ruan et al. 2015). In the case of changing look quasar SDSS J101152.98+544206.4, the broad Hα luminosity dropped by a factor of 55 on this timescale. This behavior is suspected to be caused by a sudden drop in accretion rate.

2.5.2 Persistent broad Hα

We identified 2/16 objects with secure, persistent broad Hα emission. RGG[5] 9 (NSA 10779), is classified as an AGN on the BPT diagram based on its SDSS spectrum. We

[5]RGG denotes we are using the ID assigned by Reines, Greene, & Geha (2013).

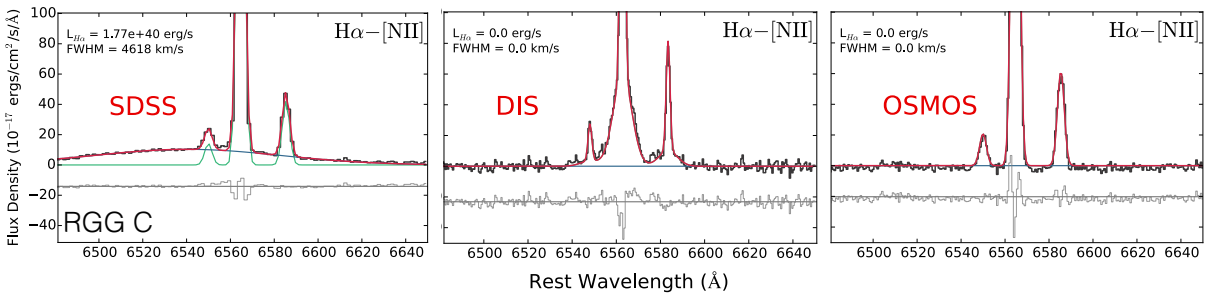

Figure 2.5 The observed Hα-[NII] complex and corresponding best-fit profile for the SDSS, DIS, and OSMOS spectra of RGG C (NSA 109990). In each, the dark gray line represents the observed spectrum. The narrow emission line fit is plotted in green, and the blue shows the fit to broad Hα emission. The overall best-fit model is given in red, and the light gray line below the observed spectrum shows the residual between the observed spectrum and the best fit, offset by an arbitrary amount. This galaxy is classified as having transient broad Hα emission.

observe broad Hα emission in both the SDSS spectrum and the DIS spectrum, taken 13 years apart (see Figure 2.6 for the best fit to the DIS spectrum). The second secure broad line object, RGG 119 (NSA 79874), is classified as a composite object on the BPT diagram. This object has broad Hα emission in the SDSS, MagE, and DIS spectra, spanning five years (see Figure 2.7).

We compute the mass of the central BH using standard virial techniques which employ only the FWHM and luminosity of the broad Hα emission (Greene & Ho 2005b; Bentz et al. 2009, 2013). The calculation also includes a scale factor ϵ intended to account for the unknown geometry of the broad line region; we adopt $\epsilon = 1$ (see Equation 5 in R13). This method makes use of multiple scaling relations between parameters (e.g., the relation between $\mathrm{FWHM_{H\alpha}}$ and $\mathrm{FWHM_{H\beta}}$), each of which has its own intrinsic scatter, giving a systematic uncertainty on the measured BH mass of 0.42 dex (Baldassare et al. 2015). To ensure that our choice of continuum subtraction method would not affect our BH mass estimates, we measured BH masses for the SDSS spectra using both R13 and our continuum subtraction, and found the masses to be consistent with one another.

For RGG 9, we measure a BH mass from the SDSS observation of $3.5(\pm0.7)\times10^5\ \mathrm{M_\odot}$.

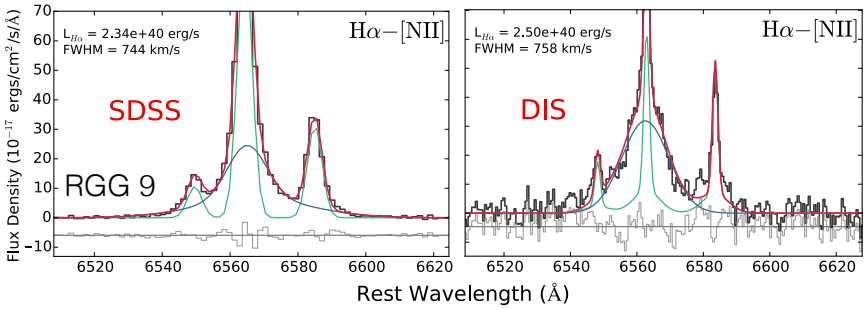

Figure 2.6 The observed Hα-[NII] complex and corresponding best-fit profile for the SDSS and DIS spectra of RGG 9. The dark gray line represents the observed spectrum. The narrow emission line fit is plotted in green, and the blue shows the fit to broad Hα emission. The overall best-fit model is given in red, and the light gray line below the observed spectrum shows the residual between the observed spectrum and the best fit, offset by an arbitrary amount. We classify this galaxy as having persistent broad Hα.

From the DIS observation, we measure a BH mass of $3.7(\pm0.3) \times 10^5$ $M_\odot$. Using these two measurements, we compute a mean mass of $M_{BH} = 3.6(\pm0.8) \times 10^5 M_\odot$. Taking into account the systematic uncertainty of 0.42 dex, this gives us a final estimate of $M_{BH} = 3.6^{+5.9}_{-2.3} \times 10^5 M_\odot$. Using the stellar mass of RGG 9 from R13 ($M_\star = 2.3 \times 10^9$ $M_\odot$), we compute a BH mass-to-stellar mass ratio of $M_{BH}/M_\star = 1.6 \times 10^{-4}$.

For RGG 119, we measure a BH mass of $2.1(\pm0.5) \times 10^5$ $M_\odot$ from the SDSS spectroscopy. The MagE observation yields a BH mass of $2.9(\pm0.2) \times 10^5$ $M_\odot$, and the DIS observation gives a BH mass of $3.6(\pm0.3) \times 10^5$ $M_\odot$. We compute a mean BH mass of $M_{BH} = 2.9(\pm0.6) \times 10^5 M_\odot$ using the three spectroscopic observations. With the additional systematic uncertainty, our final BH mass estimate is $M_{BH} = 2.9^{+4.9}_{-1.8} \times 10^5 M_\odot$. R13 reports a stellar mass of $M_\star = 2.1 \times 10^9 M_\odot$ for RGG 119, giving a BH mass to stellar mass ratio of $M_{BH}/M_\star = 1.3 \times 10^{-4}$. See Table 2.5 for the measured broad Hα FWHM and luminosities, and corresponding BH masses for each observation. We note that our measured BH masses are consistent with those measured in R13 ($2.5 \times 10^5 M_\odot$ and $5.0 \times 10^5 M_\odot$ for RGG 9 and RGG 119, respectively). We also refer the reader to Section 6 for a discussion of the potential effect of instrumentation/aperture on the measured

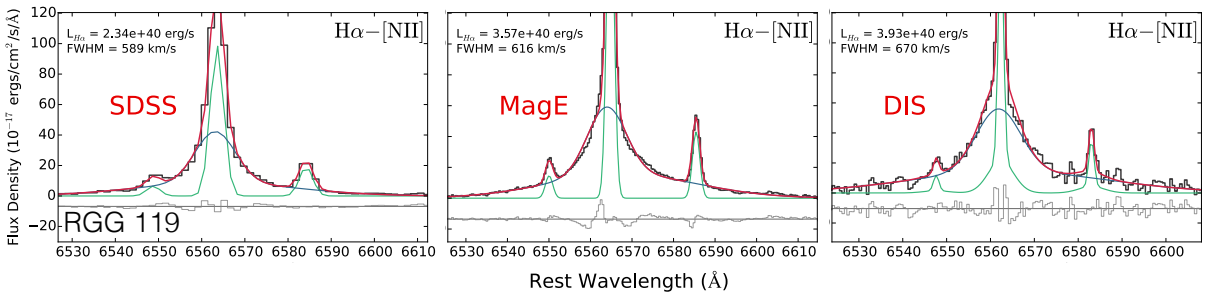

Figure 2.7 The observed Hα-[NII] complex and corresponding best-fit profile for the SDSS, MagE, and DIS spectra of RGG 119 (NSA 79874). In each, the dark gray line represents the observed spectrum. The narrow emission line fit is plotted in green, and the blue shows the fit to broad Hα emission. The overall best-fit model is given in red, and the light gray line below the observed spectrum shows the residual between the observed spectrum and the best fit, offset by an arbitrary amount. We classify this galaxy as having persistent broad Hα.

Table 2.5 Broad Hα parameters for galaxies with persistent broad Hα.

R13 ID	Obs.	$\log L_{\mathrm{H}\alpha}$ (erg s^{-1})	$\mathrm{FWHM}_{\mathrm{H}\alpha}$ (km s^{-1})	$\mathrm{M_{BH}}(10^5\ \mathrm{M}_\odot)$
9	SDSS	40.36 ± 0.01	744 ± 69	3.5 ± 0.7
9	DIS	$40.40^{+0.01}_{-0.02}$	758 ± 27	3.7 ± 0.3
119	SDSS	40.36 ± 0.01	589 ± 69	2.1 ± 0.5
119	MagE	40.55 ± 0.01	616 ± 23	2.9 ± 0.2
119	DIS	40.59 ± 0.01	670 ± 27	3.6 ± 0.3

Table 2.5. Best fit broad Hα FWHM and luminosity from each observation for objects found to have persistent broad Hα emission. We also present the corresponding BH mass calculated using the FWHM and luminosity. These values are all measured using the fitting code described in this paper, but the SDSS spectra are continuum subtracted using continuum fits obtained by R13, while the continua in the DIS and MagE spectra were modeled with a straight line.

properties of the broad Hα emission.

Using the MagE spectrum of RGG 119 we measure a stellar velocity dispersion of 28 ± 6 km s^{-1} from the Mg *b* triplet, and place this galaxy on the M_{BH}-$\sigma_\star$ relation (Figure 2.8). RGG 119 sits close to the extrapolation of M_{BH}-$\sigma_\star$ to low BH masses, similar to well-studied low-mass AGN NGC 4395 (Filippenko & Ho 2003) and Pox 52 (Barth et al. 2004). Our BH-to-galaxy stellar mass ratios are also consistent with other low-mass AGNs (Reines & Volonteri 2015).

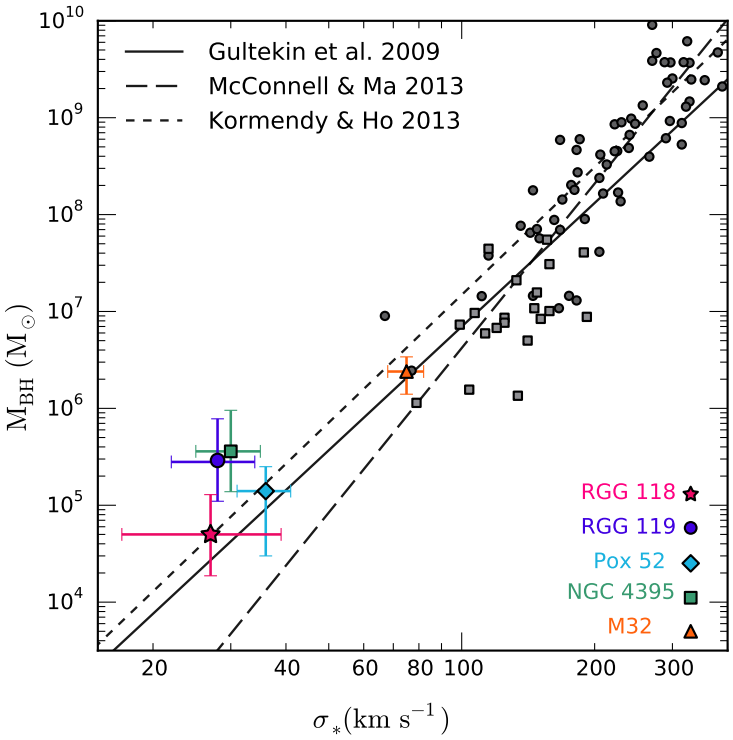

Figure 2.8 Position of low-mass AGNs on the relation between black hole mass and stellar velocity dispersion. The $M_{BH} - \sigma_\star$ relations determined in Gültekin et al. (2009), McConnell & Ma (2013), and Kormendy & Ho (2013) are plotted. We also show points for systems with dynamical BH mass measurements as compiled by Kormendy & Ho (2013) (pseudobulges are shown as gray squares, while classical bulges are plotted as gray circles). The black hole mass and stellar velocity dispersion for RGG 119 (NSA 79874; shown as a purple circle) were measured in this work. Also plotted are the low-mass AGN RGG 118 (Baldassare et al. 2015), NGC 4395 (Filippenko & Sargent 1989; Filippenko & Ho 2003), and Pox 52 (Barth et al. 2004), and the dwarf elliptical M32 (Whitmore 1980; van den Bosch & de Zeeuw 2010).

2.5.3 Ambiguous galaxies

In three cases, we were unable to definitively state whether broad Hα emission was still present and thus classify these objects as ambiguous. All three ambiguous galaxies fall in the HII region of the BPT diagram.

RGG B (NSA 15952) was observed to have broad Hα emission in its SDSS spectrum and OSMOS spectrum. Moreover, if we fit the broad Hα emission from each spectrum with one Gaussian component, we get $\mathrm{FWHM}_{\mathrm{H}\alpha,\mathrm{SDSS}} = 1036 \pm 69\,\mathrm{km\,s^{-1}}$, and $\mathrm{FWHM}_{\mathrm{H}\alpha,\mathrm{OSMOS}} = 977 \pm 32\,\mathrm{km\,s^{-1}}$ (i.e., the broad components are consistent with one another). However, the DIS spectrum – taken in between the SDSS and OSMOS spectra – does not require a broad component according to our criteria. We cannot discount that we do not detect a broad component in the DIS spectrum due to the atypical narrow-line shapes. Nevertheless, additional follow-up spectroscopy of RGG B would be useful for determining the true nature of the SDSS broad Hα emission. We note that RGG B is of particular interest since its position on the BPT diagram is consistent with a low-metallicity AGN (Izotov et al. 2007). Line ratios involving [NII] are affected by the metallicity of the AGN host galaxy (Groves et al. 2006) and AGN hosts with sub-solar metallicities can migrate left-ward into the star forming region of the BPT diagram.

RGG I (NSA 112250) has broad emission detected in the SDSS, DIS, and OSMOS spectra, but the FWHM measured for the DIS spectrum is highly dependent on the narrow-line model used, i.e., changing the parameters of the narrow-line model changes the measured FWHM by up to $\sim 90\%$. The FWHM is also not consistent between the three spectra ($1237 \pm 69\,\mathrm{km\,s^{-1}}$, $316 \pm 27\,\mathrm{km\,s^{-1}}$, and $1717 \pm 32\,\mathrm{km\,s^{-1}}$ for SDSS, DIS, and OSMOS, respectively).

Finally, RGG K (NSA 91579) has a highly asymmetric broad line observed in the SDSS and OSMOS spectra. However, the DIS spectrum, taken in between the SDSS and OS-

MOS observations, does not require a broad component. We do observe asymmetric Hα emission by eye in the all three spectra. Similarly to with RGG B, we cannot rule out that there is indeed persistent broad Hα emission, and that the DIS spectrum does not require it because of issues relating to the fitting of the unusually shaped narrow lines. Additional observations of all three ambiguous broad Hα targets will be necessary to determine whether these galaxies show persistent/consistent broad Hα and therefore do indeed host AGN. See the Appendix for figures showing fits for all observations of the ambiguous objects.

2.6 Type II supernovae in dwarf galaxies

We consider Type II supernovae the most-likely explanation for the fading broad Hα emission observed in 11/16 objects in our SDSS broad Hα sample. In this section, we further examine our SNe II candidates, and discuss this hypothesis in more detail. All 11 objects with transient broad Hα have narrow line ratios consistent with recent star formation. Moreover, their broad emission properties and galaxy properties are offset from the remainder of the SDSS broad line objects in two important ways.

As seen in Figure 2.9, SDSS broad emission that we found to be transient tended to have larger FWHM and broad lines that were more offset from the Hα line center in velocity space. All SDSS broad Hα emission lines with FWHM $\gtrsim 2000\,\mathrm{km\,s^{-1}}$ in our sample were found to be transient, as well as all those with absolute velocity offsets of more than $\sim 200\,\mathrm{km\,s^{-1}}$.

Additionally, galaxies with transient broad Hα also tend to be bluer with respect to the sample of broad and narrow-line candidate AGN host galaxies from R13 (Figure 2.10). The narrow-line AGN candidates were found to have a median galaxy color of $g - r = 0.51$ (R13), while the transient broad Hα galaxies have a median host galaxy color of

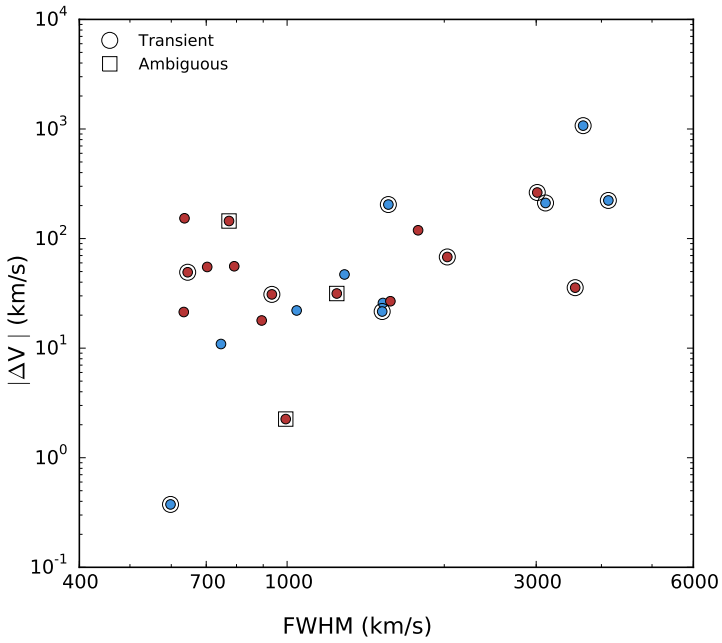

Figure 2.9 Velocity offset from the center of the Hα emission line in $\mathrm{km\,s^{-1}}$ versus the FWHM of the broad Hα emission from R13. A red dot indicates the broad line is red-shifted in velocity space, blue indicates the broad line is blue-shifted. The dots with circles around them are objects with transient broad Hα (i.e., likely SNe II hosts). Large FWHM and/or velocity shifts are more characteristic of galaxies with transient broad Hα emission.

$g - r = 0.22$ (with all transient broad Hα galaxies having $g - r < 0.4$). This suggests the transient broad Hα galaxies have, in general, younger stellar populations more likely to produce SNe II.

Using time-domain spectroscopy, we have empirically identified targets most likely to be SNe based on the disappearance of broad emission lines over long ($\sim 5 - 10$ year) time scales. A complementary analysis was performed by Graur et al. (2013, 2015). They searched through most SDSS galaxy spectra for SN-like spectra, and used SN template matching, rather than broad emission line fitting, to identify potential SNe. Here, we compare the results of the two methods.

Similar to Graur et al. (2013, 2015), R13 did identify 9 SN candidates (in a sample of $\sim 25,000$ objects) directly from the single-epoch SDSS spectra (Table 5 in R13; none of those have been followed up in this work). Those objects were identified because they

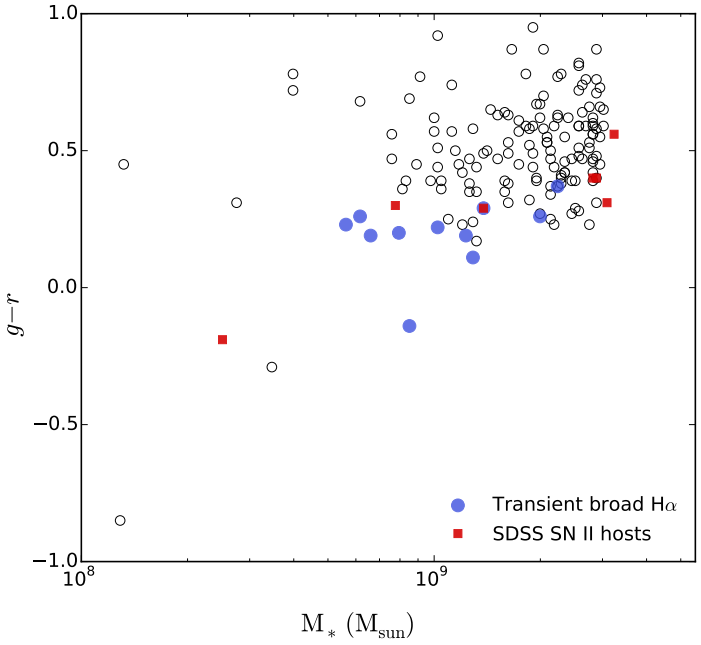

Figure 2.10 Galaxy $g-r$ color versus host galaxy stellar mass for narrow and broad line AGN candidates from R13. Stellar masses and $g-r$ colors are from the NASA-Sloan Atlas database. Objects with transient broad Hα are plotted as the larger blue circles. These galaxies tend to have bluer colors with respect to the rest of the sample. We also include SNe II hosts identified in the SDSS (Graur & Maoz 2013; Graur et al. 2015) in galaxies below our mass cut-off. The masses and colors for these also come from the NASA-Sloan Atlas database (except for the lowest mass SDSS SN II host, for which the mass/color are derived from the MPA-JHU Galspec pipeline).

exhibited P Cygni profiles in Hα. Of the 15 BPT star forming galaxies with broad Hα identified in R13 as AGN candidates (14 of which are considered in this paper), one was detected by Graur et al. (2015) and classified as a SN II (RGG M, identified in Table 1 of Graur et al. 2015 as SDSS J131503.77+223522.7 or 2651-54507-488). The remainder did not meet all of the detection criteria set by Graur et al. (2013, 2015) and thus were not detected by Graur et al. (2015). The Graur et al. (2013, 2015) method is superior at detecting bona fide SNe II near maximum light, when these objects display prominent P-Cygni profiles. The nature of the objects considered in this paper is generally more ambiguous, as no P-Cygni profiles are seen and the emission line profiles are relatively symmetric (although generally broader and more asymmetric than the bona fide AGN; Figure 2.9).

During their survey, Graur et al. (2015) also identified five ambiguous broad-line objects in dwarf galaxies, which their pipeline classified as either SNe or AGNs. Of these, three were not in the R13 parent sample due to the stellar mass cut in two cases and a glitch in the NSA catalog in the third. Two are in R13; one was identified as a transient (Koss et al. 2014), and the other (RGG J) is included in this work.

To understand why the majority of the transient sources presented here were not identified by Graur et al. (2013, 2015), and to try and learn something about their nature, we pass our continuum-subtracted SDSS spectra through the same supernova identification scheme used by Graur et al. First, the stellar continuum and narrow emission line fits are removed. We employ a different procedure from that used by Graur et al. to fit the continuum, but the overall result should be similar. Second, we de-redshift the spectra, remove their continua, and manually ran them through the Supernova Identification code (SNID;[6] Blondin & Tonry 2007). Four objects were classified as old SNe II, i.e., when their spectra

[6]http://people.lam.fr/blondin.stephane/software/snid/

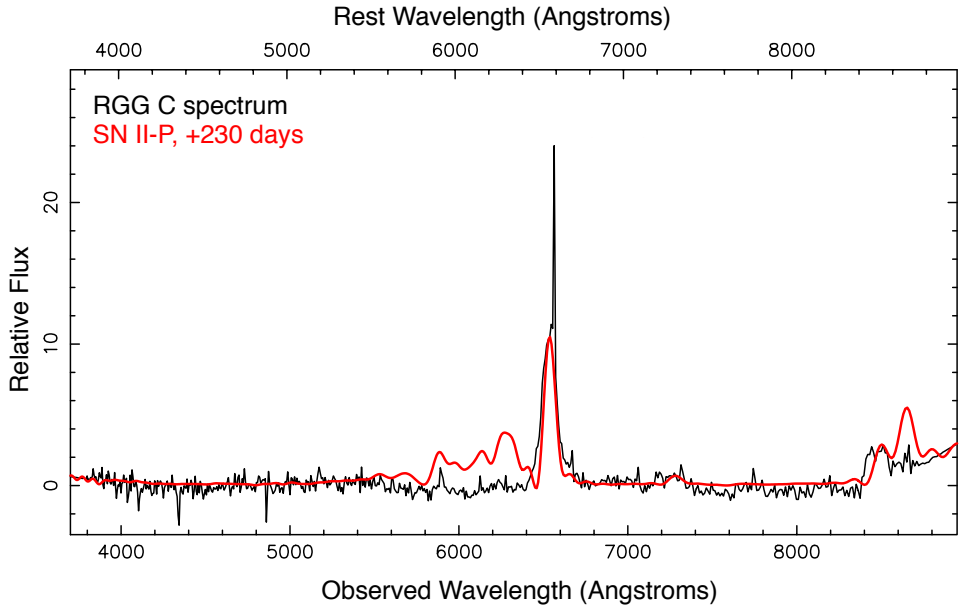

Figure 2.11 The Supernova Identification (SNID) code fit to the SDSS spectrum of RGG C. This fit had an rlap value of 7.1. The observed spectrum is shown in black, while the SNID fit is shown in red. SNID finds that the spectrum is best fit by a post-plateau SN II-P.

are dominated by a broad Hα feature, but with relatively low rlap values. The SNID 'rlap' parameter is used to assess the quality of the fit, and is equal to the height-to-noise ratio of the normalized correlation function times the overlap between the input and template spectra in $\ln\ \lambda$ space (see Blondin & Tonry 2007 for details). A value of rlap=5 is the default minimum and fits with rlap values close to 5 are regarded as suspect (see Blondin & Tonry 2007 for details). Of the four objects identified as SNe II, two had rlap values < 5 and two had rlap ~ 7. One object was classified as an old SN Ia at z $\sim$0.1. As the spectra were de-redshifted, this classification is not trustworthy. The other three objects failed to be classified by SNID. See Figure 2.11 for an example of the fit obtained by SNID to RGG C. We will discuss the special case of RGG J in some detail in Section 2.6.1.

Since we consider SNe II the best explanation for the transient broad emission, in the following we compute the expected number of SNe II in the R13 parent sample, and check for consistency with our results. R13 identified and removed 9 galaxies with SNe II from

their sample based on P Cygni profiles in the broad Hα emission. Considering the 11 objects with transient broad Hα and three ambiguous objects identified in this work, we have $20 - 23$ SNe II candidates. The Lick Observatory Supernova Search (Li et al. 2000) calculated the rate of SNe II in the local universe as a function of color and Hubble Type by observing more than 10,000 galaxies over the course of 12 years (Li et al. 2011a). Using representative SDSS *gri* magnitudes and $(g - r)$ and $(r - i)$ colors for the star forming galaxies from R13, we use filter transformations (Jester et al. 2005; Bilir et al. 2008) to determine a typical $(B - K)$ color in order to select the correct SN rate from Li et al. (2011a). Choosing a galaxy stellar mass of $1.2 \times 10^9\ M_\odot$and using the equation for $(B - K) < 2.3$, we find the expected rate of SNe II in a given galaxy over the course of 6 months is $0.002^{+0.003}_{-0.001}$. We then convert this to a probability using Poisson statistics. We choose to compute the rate over 6 months since SNe II typically begin to fade at $100 - 150$ days post explosion (see e.g., Kasen & Woosley 2009).

Similarly, Graur et al. (2015) measured a mass-normalized SN II rate of $5.5^{+3.7}_{-2.4}$ statistical $^{+1.2}_{-0.7}$ systematic $\times 10^{-12}\ \mathrm{yr}^{-1}\ \mathrm{M}_\odot^{-1}$ in galaxies with stellar masses of $0.08^{+0.06}_{-0.05}\ \times 10^{10}\ \mathrm{M}_\odot$ (see their table 2). Thus, for a galaxy of $10^9\ \mathrm{M}_\odot$, we would expect $0.0026^{+0.0025}_{-0.0016}$ SNe II in a period of six months, consistent with the rate derived from Li et al. (2011).

R13 analyzed spectroscopy of $\sim 25,000$ dwarf galaxies. For a sample of this size, the rate derived from Li et al. (2011a) suggests we can expect 50^{+75}_{-25} SNe II. Using the rate from Graur et al. (2015), we expect 65^{+63}_{-40} SNe II in a sample of 25,000 galaxies. Both rates are roughly consistent with the number we detect in our sample. Using either rate, we compute that in a sample of 25,000 galaxies, we expect less than 1 to have an observed SN signature in the original SDSS observation *and* a signature from a new SN in the follow-up observation.

2.6.1 A Possible SN IIn in RGG J

In the following, we discuss the interesting case of RGG J. This particular source, classified in this work as having transient broad Hα emission, has fooled many of us. It was identified as a broad line AGN in Greene & Ho (2007), Stern & Laor (2012), and Dong et al. (2012b). Thus, it serves as an excellent cautionary tale that there may well be transient sources lurking in our broad-line AGN samples even at higher mass.

We also have more epochs for this target than others. It was observed twice by the SDSS, once by Xiao et al. (2011) (spectrum taken in 2008), and once by us in 2013. The SDSS spectra were taken on 11 March 2003 and 05 April 2003 (see Figure 2.12). Thus, our observations span a full decade. The SDSS flagged the second epoch as the "primary" spectrum, and so the fits in the literature are most likely made to that later epoch. During their survey, Graur et al. (2015) classified this source as either a SN IIn or an AGN based on a fit to the April 2003 spectrum. By 2008, when Xiao et al. (2011) observed this source with the Echellette Spectrograph and Imager on Keck II, there was still a (rather marginal) detection of broad Ha. The broad line is undetectable in our DIS spectrum, so we conclude the broad line may be produced by a SN IIn (Figure 2.12).

Unlike SNe II-P and II-L, which exhibit broad H emission lines with P-Cygni profiles, Type IIn supernovae (SNe IIn) are characterized by narrow lines (FWHM $\lesssim 200$ km/s; hence the 'n' in 'IIn') with intermediate-width bases (FWHM $\sim 1000 - 2000$ km/s) and bluer continua (see Filippenko 1997 for a review). SNe IIn comprise $\approx 5 \pm 2\%$ of all SNe and show a wide spread of peak luminosity (Li et al. 2011b). The narrow lines are thought to be the result of strong interaction between the SN ejecta and a dense circumstellar medium. Though some SNe IIn have been associated with luminous blue variables (e.g., SN 2005gl; Gal-Yam & Leonard 2009, SN 2010jl; Smith et al. 2011b, and SN 2009ip; Foley et al. 2011), the exact nature of their progenitors is still debated (see Smith 2014 for

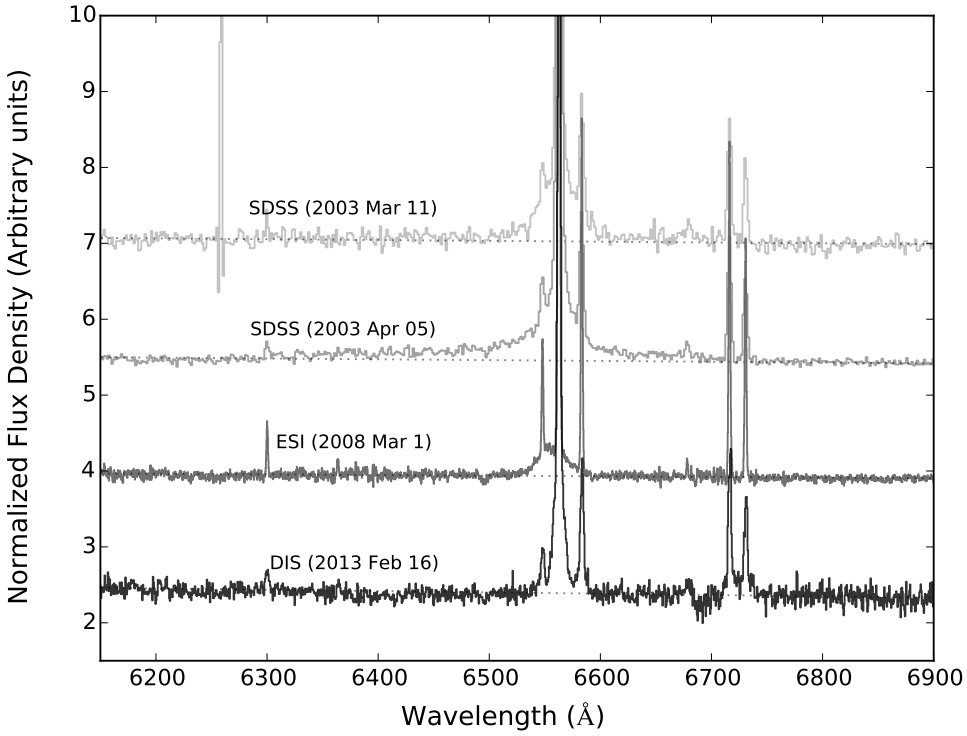

Figure 2.12 The Hα regime of the four observed spectra of RGG J. Broad Hα is clearly visibile in the two SDSS spectra taken in 2003. An Keck II ESI spectrum was taken in 2008 (Xiao et al. 2011; spectrum provided by Aaron Barth, private communication). This spectrum shows some broad Hα emission as well, though it is distinctly blue-shifted with respect to the narrow Hα line center. The DIS spectrum, taken in 2013 and analyzed in this work, does not show evidence for broad Hα emission.

a review).

2.7 Discussion

We analyzed follow-up spectroscopy of 27 dwarf galaxies with AGN signatures identified in a sample of $\sim 25,000$ dwarf galaxies in the SDSS (see R13). Of our follow-up targets, 16 were found by R13 to have broad Hα emission in their SDSS spectra, and 14 had narrow emission line ratios indicative of AGN activity (there is some overlap between the broad and narrow-line objects).

Of the 16 SDSS broad Hα objects for which we have follow-up spectroscopy, we found that the broad Hα emission faded for eleven, all of which fall in the star forming region of

the BPT diagram. As stated above, we consider SNe II to be the most likely cause of the original broad emission for these objects, though luminous blue variables and changing look quasars also produce transient broad Hα (see R13 for a more complete discussion of potential contaminants). We also find two of the SDSS broad Hα objects, both of which had narrow-line AGN signatures, to have persistent broad Hα emission, suggesting it is emission from virialized gas around a central BH. This also suggests that the broad emission for the remainder of the R13 narrow-line AGN/composite objects is due to an AGN. R13 calculates the type 1 fraction (or the fraction with detectable broad Hα emission) for BPT AGN to be $\sim 17\%$ (6/35 objects). The type 1 fraction for BPT composites is lower; including RGG 118 (Baldassare et al. 2015), $\sim 5\%$ of the composites (5/101) are type 1. Finally, three SDSS broad Hα objects (all BPT star forming) are ambiguous and will require further observations to determine the source of broad emission.

In the case of RGG J, (the expected Type II SN; see Section 2.6.1), the broad emission was persistent over at least 5 years, but the FWHM and velocity shift varied considerably. Thus, in addition to determining whether broad emission is *persistent*, we also check for consistency between epochs. We note that differences in aperture could slightly affect broad emission measurements since the measured luminosity and FWHM of broad Hα depend on the fit to the narrow emission lines. Additionally, the instruments used all have different spectral resolutions, which can affect the measured FWHM. Finally, broad line regions can vary intrinsically on these timescales (Tremou et al. 2015), making it difficult to determine the degree to which aperture effects play a role. Nevertheless, for RGG 9, we find the two measured FWHM to be consistent with one another within the errors. For RGG 119, the measured FWHM of Hα increases by $\sim 13\%$ over the course of our three observations (though the first and last measurements are consistent within the errors).

2.8 Conclusions

In summary, we were able to securely detect broad Hα arising from an AGN in the follow-up observations of two SDSS broad Hα galaxies; both of these objects also have narrow-line ratios which support the presence of an AGN. Both objects (RGG 9 and RGG 119) have BH masses of a few times 10^5 $\mathrm{M}_\odot$. *Chandra X-ray Observatory* observations (Cycle 16, PI: Reines) will provide further valuable information about the accretion properties of these AGN. Three SDSS broad line objects (all BPT star forming) are classified as ambiguous and will require additional observations to determine whether an AGN is present. For the remainder of the star forming SDSS broad Hα dwarf galaxies, we find that transient stellar phenomena are likely to be the source of detected broad Hα emission. Given the relatively low FWHMs, faint flux levels, and the prevalence of young stars, we confirm that, in dwarf galaxies (and perhaps more massive galaxies) broad Hα alone should not be taken as evidence for an AGN – another piece of evidence (such as narrow line ratios) is required (see also discussions in R13 and Moran et al. 2014).

We also measure stellar velocity dispersions for 12 galaxies with narrow-line AGN signatures. One of these – RGG 119 – also has persistent broad Hα emission. In this case, we use the broad emission to measure the BH mass and find that RGG 119 lies near the extrapolation of the $\mathrm{M_{BH}}$–$\sigma_\star$ relation to low BH masses. The measured stellar velocity dispersions for these targets range from $28 - 71\,\mathrm{km\,s^{-1}}$ with a median value of $41\,\mathrm{km\,s^{-1}}$. With galaxy stellar masses of just a few times 10^9, these stellar velocity dispersions correspond to some of the lowest-mass galaxies with accreting BHs. If the remaining narrow-line AGN/composites similarly follow the $\mathrm{M_{BH}}$–$\sigma_\star$ relation, their BH masses would range from $\sim 6 \times 10^4 - 2 \times 10^6\ M_\odot$ (using the relation reported in Gültekin et al. 2009).

2.9 Emission line fitting examples

Below are examples of emission line fits for two systems, one of which has transient broad Hα emission, and one which has persistent broad Hα.

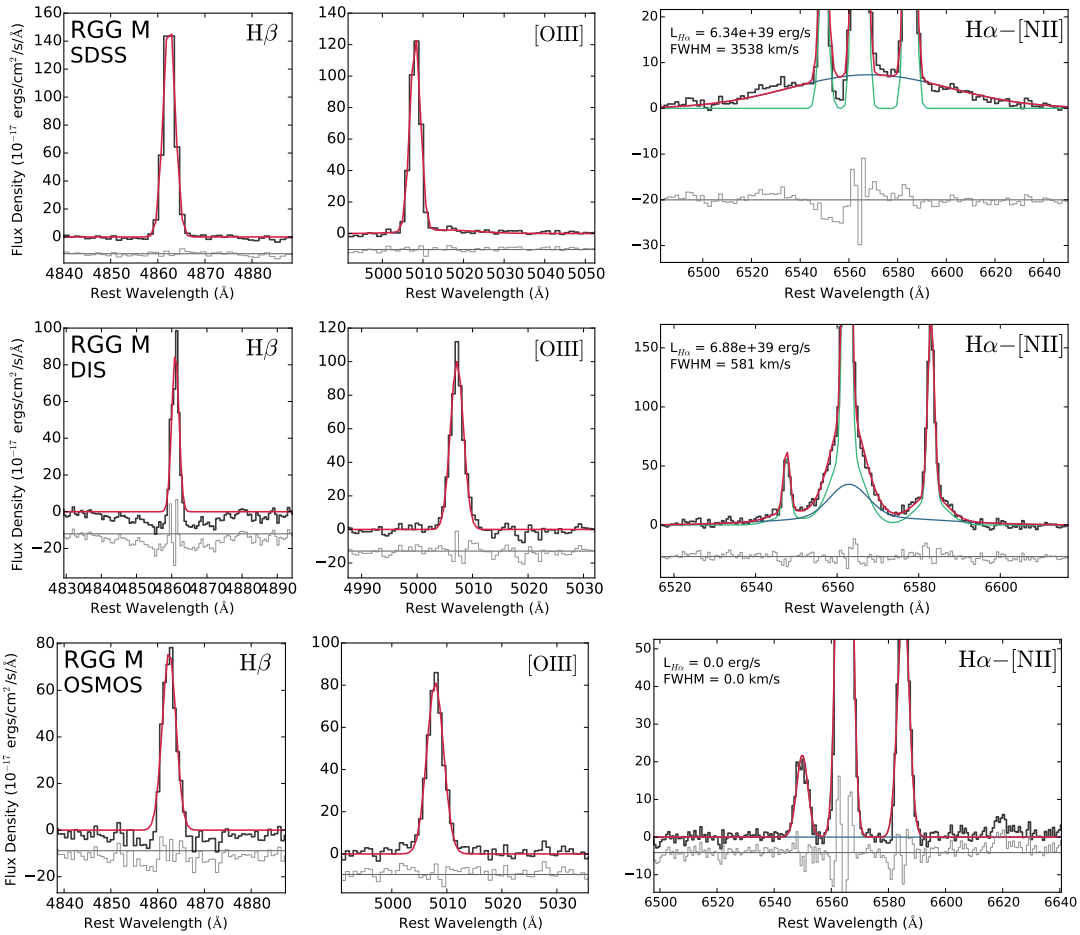

Figure 2.13 These plots show the Hβ, [OIII]λ5007, Hα, and [NII]$\lambda\lambda 6718, 6731$ lines for each observation taken of RGG M (NSA 119311). The black line shows the observed spectrum, the red line shows our best fit to the line, and the gray shows the residual between the data and model. In the fit to the Hα-[NII] complex, the green line shows the fit to the narrow lines, and the blue line shows the fit to the broad component, if present.

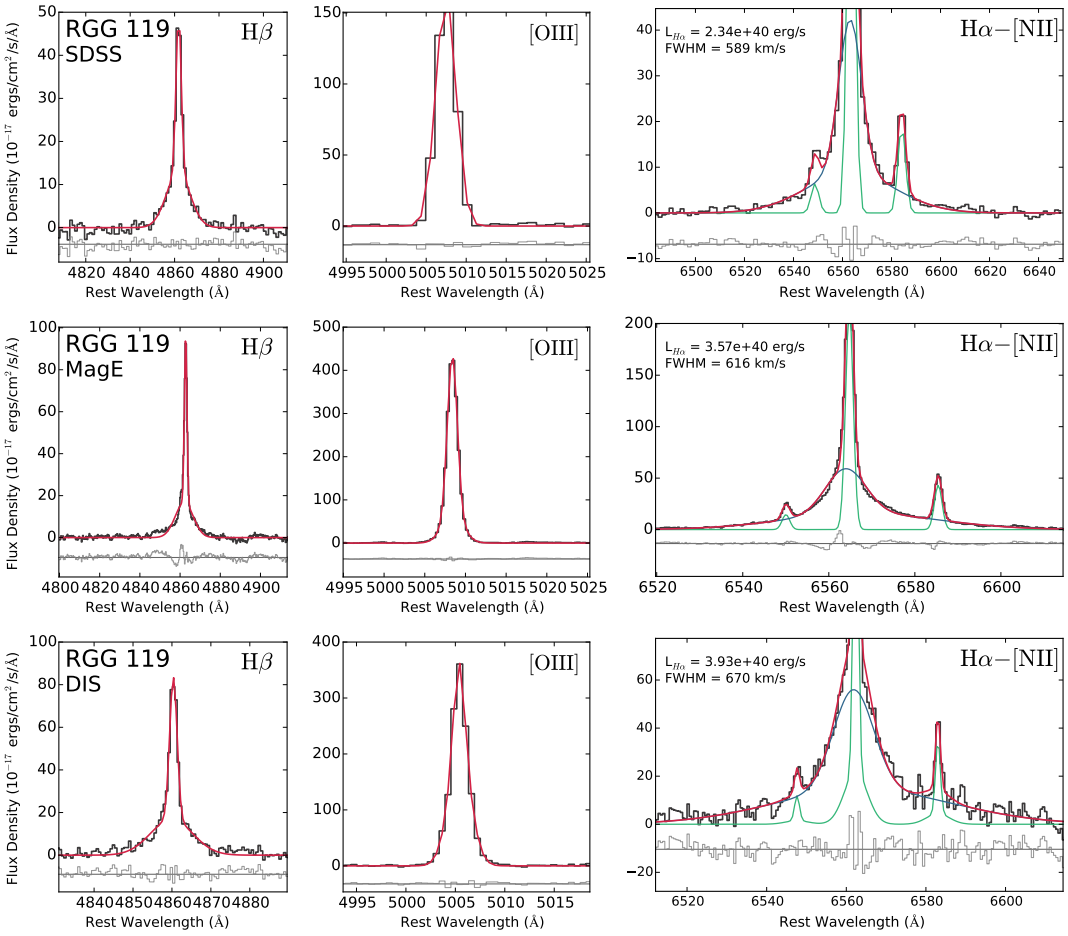

Figure 2.14 These plots show the Hβ, [OIII]λ5007, Hα, and [NII]$\lambda\lambda$6718, 6731 lines for each observation taken of RGG 119 (NSA 79874). Description is same as for Figure 2.13. We place this object in the "persistent broad Hα" category.

CHAPTER III

A 50,000 solar mass black hole in the nucleus of a dwarf galaxy

3.1 Motivation and Aims

This chapter presents a multi-wavelength analysis of the dwarf galaxy RGG 118, and is based on results published in Baldassare et al. (2015) and Baldassare et al. (2017, *submitted*). RGG 118 is a dwarf, disk galaxy ~ 100 Mpc (or 300-million light years) away, first identified as having narrow emission-line AGN signatures by Reines et al. (2013) and was a part of a sub-sample targeted for follow-up spectroscopy, as discussed in Chapter 2. Our subsequent analysis of high-resolution spectroscopy with the Magellan Echellette Spectrograph on the 6.5m Clay telescope at Las Campanas Observatory clearly revealed the presence of a broad Hα emission line, which we use to measure a BH mass of $\sim 50,000\ M_{\odot}$. At the time of writing, this is the smallest BH yet reported in a galaxy nucleus. We present *Chandra* X-ray observations showing nuclear hard X-ray emission, which provides further confirmation of an AGN in RGG 118. Based on the X-ray luminosity and a bolometric correction, we estimate that the BH in RGG 118 is accreting at $\sim 1\%$ of its Eddington fraction – similar to more massive AGNs at high redshift. Finally, we present an analysis of the structure of RGG 118 from new *Hubble Space Telescope* WFC3 UVIS and IR imaging.

3.2 Introduction

It is now established that most, if not all, massive galaxies (e.g. $M_* \gtrsim 10^{10}\ M_\odot$) host massive black holes (BHs) at their centers. Moreover, the BH masses correlate with properties of the host galaxy, such as bulge stellar velocity dispersion, bulge luminosity, and bulge mass, pointing towards co-evolution of galaxies and their BHs (Ferrarese & Merritt 2000; Gebhardt et al. 2000a; Marconi & Hunt 2003; Gültekin et al. 2009; Kormendy & Ho 2013; McConnell & Ma 2013). However, these scaling relations are poorly constrained for low BH/galaxy masses ($M_{\rm BH} \lesssim 10^6\ M_\odot$). It is presently unknown what fraction of low-mass galaxies ($M_* \lesssim 10^{10}\ M_\odot$) contain BHs, and BH mass measurements in this regime are relatively scarce.

The low-mass end of scaling relations is of particular importance for constraining models of high-redshift BH seed formation. Volonteri & Natarajan (2009) found that for BH masses $\lesssim 10^6\ M_\odot$, the slope and scatter of $M_{\rm BH} - \sigma_*$ vary depending on whether BH seeds were massive ($\sim 10^{4-5}\ M_\odot$, e.g. from direct collapse) or smaller Population III remnants ($\sim 100\ M_\odot$). Additionally, the fraction of low-mass galaxies hosting BHs is itself important for models of BH seed formation (e.g. Volonteri et al. 2008; Miller et al. 2015).

BH mass measurements for dwarf galaxies remain difficult to achieve and are often highly uncertain. Dynamical mass measurements for low-mass BHs are limited by the resolving power of our telescopes; even with the *Hubble Space Telescope*, we can only resolve the sphere of influence of BHs with $M_{\rm BH} \sim 10^5\ M_\odot$ for the Local Group. Active galactic nuclei (AGN) offer an opportunity to measure BH masses in systems beyond the Local Group; for AGN in dwarf galaxies, we can estimate masses based on broad emission lines if present (e.g. Greene & Ho 2005b; Reines et al. 2013), or from the fundamental

plane of BH activity (Merloni et al. 2003; Reines et al. 2011, 2014). These methods rely on correlations between various observables and BH mass, and thus carry larger uncertainties.

In the last few years, the number of known dwarf galaxy–AGN systems has moved beyond a few key examples such as NGC 4395 (Filippenko & Ho 2003), POX 52 (Barth et al. 2004), and Henize 2-10 (Reines et al. 2011; Reines & Deller 2012) to increasingly larger samples. The first systematic searches for low-mass BHs were done by Greene & Ho (2004, 2007), which searched the Sloan Digital Sky Survey (SDSS) for galaxies with broad Hα emission indicating AGN with masses below $2 \times 10^6 M_\odot$. Though these surveys identified ~ 200 such BHs, the host galaxies had stellar masses larger than typical dwarf galaxies (Greene et al. 2008). More recently, Reines et al. (2013) increased the number of known AGN in dwarf galaxies by an order of magnitude by searching for narrow and broad emission line AGN signatures in a sample of nearby (z $\lesssim 0.055$) dwarf galaxies ($M_* \lesssim 3 \times 10^9\ M_\odot$) in the SDSS (see also Moran et al. 2014).

Here we present optical spectroscopy, *Chandra* X-ray observations, and *Hubble Space Telescope* (HST) optical/near-infrared imaging observations of SDSS J1523+1145 (object 118 in Reines et al. 2013; hereafter referred to as RGG 118), a dwarf disk galaxy with a stellar mass of $\sim 2.5 \times 10^9\ M_\odot$ at a redshift of z = 0.0243. First identified as having narrow line ratios indicative of AGN activity based on SDSS spectroscopy, our new higher resolution spectroscopy reveals broad Hα emission indicative of a $\sim 50,000\ M_\odot$ BH.

3.3 Observations and Data Reduction

3.3.1 SDSS

The SDSS makes use of a dedicated 2.5m telescope at Apache Point Observatory in Sunspot, NM. Five band SDSS *ugriz* imaging was taken for the field containing RGG 118 on 12 May 2005 (Figure 3.1). SDSS spectroscopy of RGG 118 was taken on 14 May 2007.

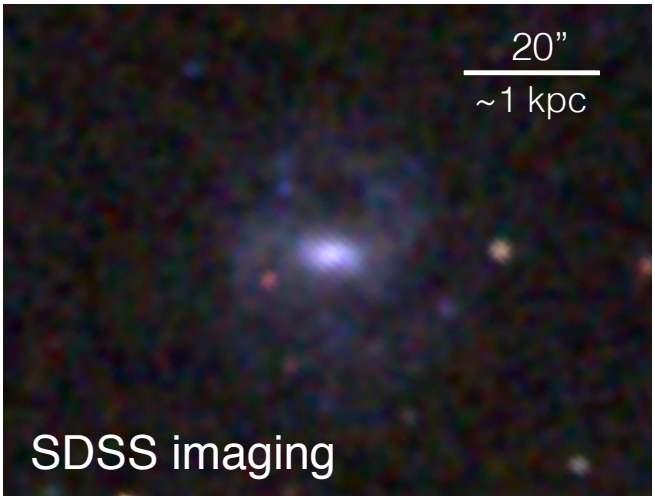

Figure 3.1 Smoothed SDSS *gri* image of RGG 118 (filters colored blue, green, and red, respectively).

The SDSS fiber-fed spectrograph uses fibers with a diameter of 3”, and has wavelength coverage extending from 3800 to 9200 Å.

3.3.2 MagE

Spectra of RGG 118 were taken on 18 April 2013 with the 6.5m Magellan II telescope at Las Campanas Observatory, using the Magellan Echellette Spectrograph (MagE; Marshall et al. 2008). MagE is a moderate resolution ($\lambda/\Delta\lambda = 4100$) echelle spectrograph, with wavelength coverage extending from 3000 to 10000Å over 15 orders. Using the arc lamp exposures, we measure an instrumental dispersion $\sigma_{\rm instrument} = 28$ km s^{-1} $\pm$ 5 km s^{-1}. Two 1200-second exposures of RGG 118 were taken using a 1″ slit. Flat fielding, sky subtraction, extraction, and wavelength calibration were carried out using the mage_reduce IDL pipeline written by George Becker. We used a boxcar extraction with an extraction width of 1″, in order to obtain the nuclear spectrum and reduce contamination from starlight.

3.3.3 Chandra X-ray Observatory

Chandra observed the field of RGG 118 with the Advanced CCD Imaging Spectrometer (ACIS) detector on 2014-12-26 UT 18:09:21, for a total of 19.8 ksec, with the target galaxy placed on the back-illuminated S3 chip of ACIS-S. Data were telemetered in very-faint mode and analysed with the *Chandra* Interactive Analysis of Observations software package (CIAO, version 4.6). First, we improved the *Chandra* astrometry by cross-matching the detected X-ray point sources on the S3 chip to the SDSS catalog (the initial X-ray source list was derived by running CIAO WAVDETECT on the pipeline event file, with the exclusion of a $2''$ circular aperture centered on the nominal position of RGG 118). This resulted in 4 matches to an SDSS optical counterpart with r-band magnitude brighter than 23 mag, yielding a final astrometric correction of $\sim 0''.7$. Next, we reprocessed the data to generate a new event list, and searched for time intervals with anomalously high background rates (none were found). Further analysis was restricted to the energy interval 0.5-7 keV, where ACIS is best calibrated.

3.3.4 Hubble Space Telescope

We obtained HST Wide Field Camera 3 (WFC3) imaging of RGG 118. Images were taken over three orbits during July 2016 (Cycle 23, Proposal 14187, PI: Baldassare). We took observations in two UVIS filters (F475W and F775W) and one IR filter (F160W). These filters correspond to *g*, *i*, and *H* band, respectively. We also employ a traditional four point dither pattern.

Data were reprocessed using the AstroDrizzle pipeline in the DrizzlePac software package. We used a square drizzling kernel and inverse-variance map weighting, recommended for background-limited targets. The native pixel scales for WFC3 are $0.04''$/pix for the UVIS channel and $0.13''$/pix for the IR channel. However, dithering of observations al-

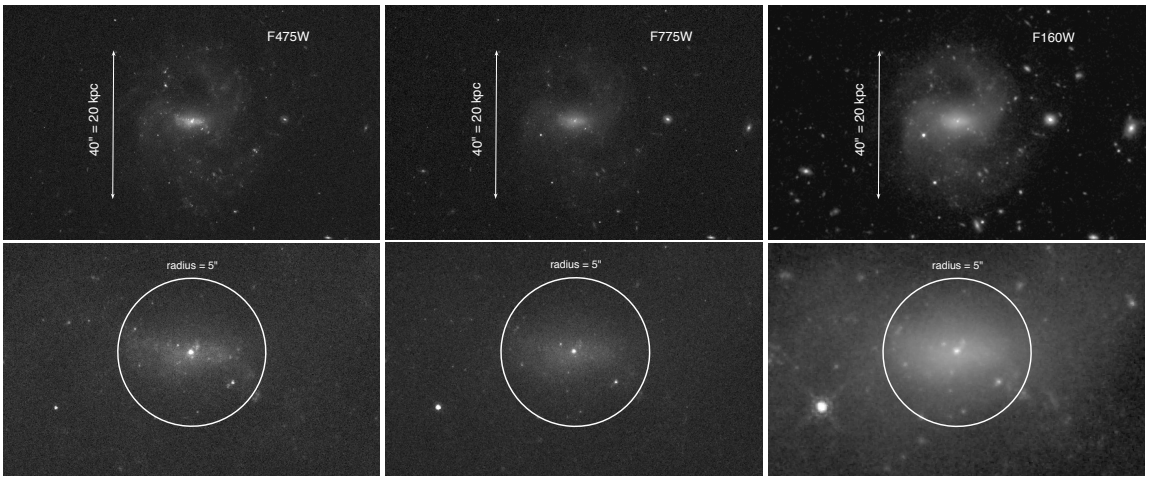

Figure 3.2 *Hubble Space Telescope* WFC3 images of RGG 118 in F475W (left), F775W (middle) and F160W (right) filters. Top row: Full galaxy images, smoothed with a Gaussian kernel of 3 pixels. Bottom row: Zoom-ins of the nucleus, not smoothed.

lows one to improve the pixel sampling of the final product. For the UVIS observations, our final drizzled product used a final pixel fraction (*final_pixfrac* parameter in AstroDrizzle) of 0.5 and a final pixel scale (*final_scale*) of 0.03″/pix. The IR observations have a *final_pixfrac* of 0.8 and *final_scale* of 0.09″/pix. Point spread functions (PSFs) for each filter were constructed using the PSF fitting software *Starfit*[1]. Figure 3.2 shows the *HST* imaging in each band. Figure 3.3 shows a comparison of the Starfit-generated PSF to the profile of a bright star in the F160W image.

3.4 Optical spectroscopic analysis

3.4.1 Emission-line modeling

Reines et al. (2013) used the SDSS and NASA-Sloan Atlas to search for dwarf galaxies with optical spectroscopic signatures of accretion onto a massive BH. They modeled the spectra of ∼25,000 nearby (z $\lesssim 0.055$) dwarf ($M_* \lesssim 3 \times 10^9\ M_\odot$) galaxies, and measured emission line fluxes. Using the narrow-line [OIII]/Hβ versus [NII]/Hα diagnostic diagram (Kewley et al. 2006), they identified 136 galaxies with emission line ratios consistent with

[1] https://www.ssucet.org/∼thamilton/research/starfit.html

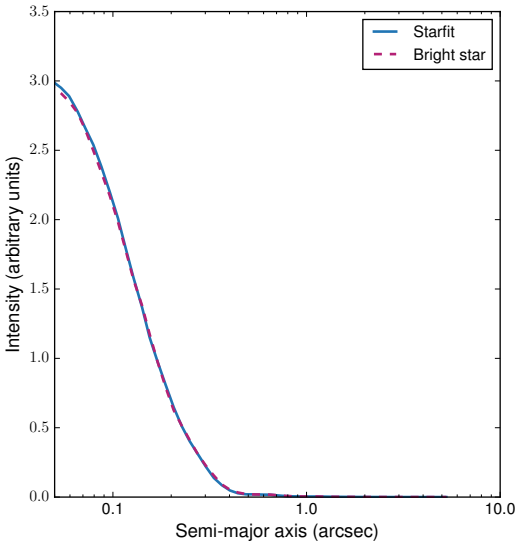

Figure 3.3 Intensity versus semi-major axis of the PSF generated by Starfit and a bright star in the image. They have been normalized to the same central intensity.

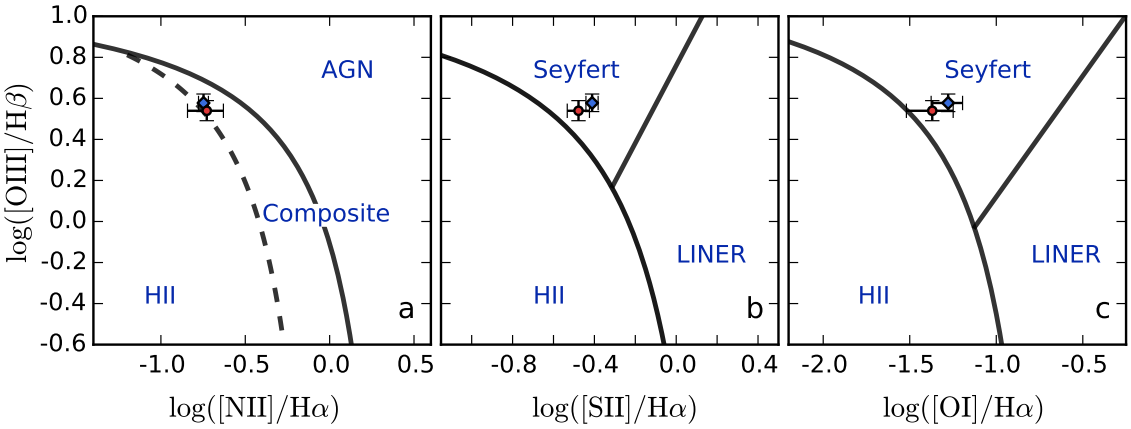

Figure 3.4 Narrow emission line diagnostic diagrams for RGG 118. Diagnostic diagrams which characterize the photoionizing continuum in RGG 118 (Baldwin et al. 1981; Veilleux & Osterbrock 1987; Kewley et al. 2006). All diagrams plot $\log([\mathrm{OIII}]/\mathrm{H}\beta)$ on the y-axis. On the x-axis, ratios of $[\mathrm{NII}]\lambda6583$, $[\mathrm{SII}]\lambda6716, 6731$, and $[\mathrm{OI}]\lambda6300$ to $\mathrm{H}\alpha$ are shown from left to right. Blue diamonds represent values from SDSS data (Reines et al. 2013) while red circles represent MagE data. All three diagrams indicate that the photoionization in RGG 118 is at least partly due to an AGN.

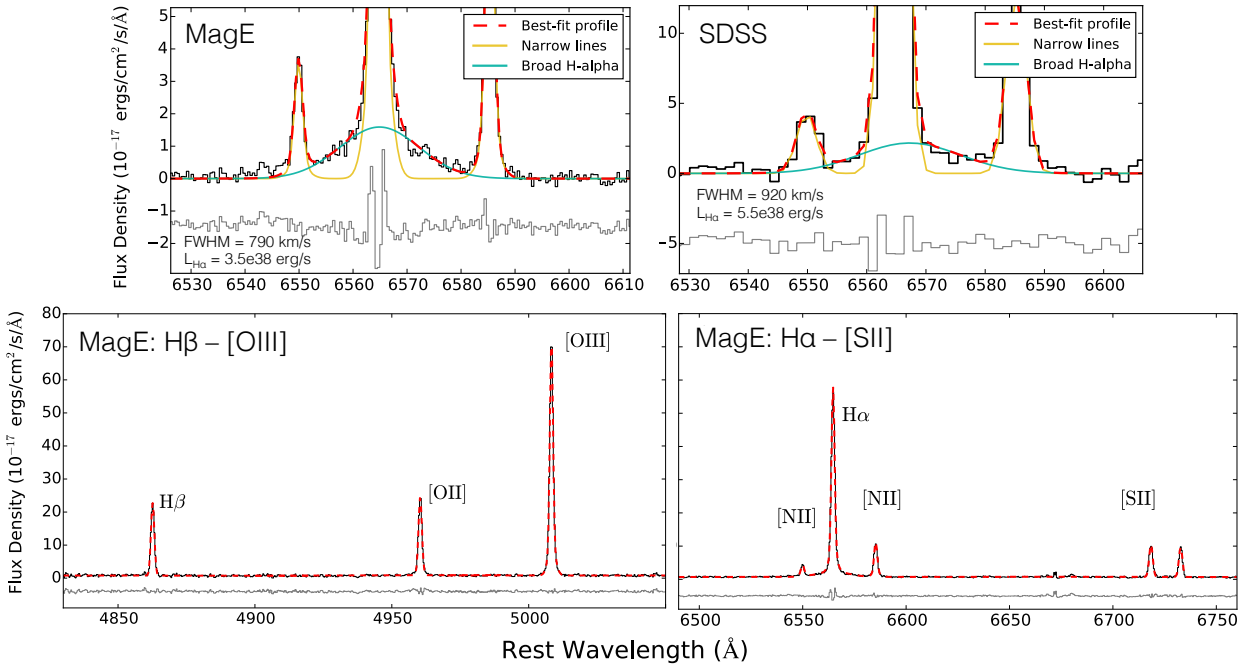

Figure 3.5 Observations of RGG 118 taken with the Magellan Echellette Spectrograph. In all panels, the black line is the observed spectrum, the red dashed line is the best-fit total profile, and the gray line is the residual between the observed spectrum and best fit, offset by an arbitrary amount.*Top*: MagE (left) and SDSS (right) spectra showing the Hα-[NII] complex. The yellow and teal solid lines represent the best-fit narrow and broad components, respectively. The narrow line model used for the MagE fit shown here is based on the [OIII] line (Model C; see text). The SDSS best-fit parameters yield a BH mass of $\sim 91,000$ $M_{\odot}$. The MagE Hα FWHM and luminosity imply a BH mass of $\sim 50,000$ $M_{\odot}$. *Bottom*: Regions of the MagE spectrum of RGG 118 showing the emission lines most relevant to our analysis.

(at least some) photoionization from an accreting BH. RGG 118 fell into the "composite" region of the [OIII]/Hβ versus [NII]/Hα diagram, indicating photoionization from both an accreting BH and stellar processes (Figure 3.4). The SDSS spectrum of RGG 118 shows evidence for broad Hα emission (see top right of Figure 3.5), but it was not identified by Reines et al. (2013) because it falls below their broad Hα detection limit of $\sim 2 \times 10^{39}$ erg s^{-1} (at their sample median redshift of z$\sim$0.03).

We analyzed the spectrum of RGG 118 using custom emission line fitting software developed in Python and broadly following the procedure laid out in Reines et al. (2013). Our software uses non-linear least squares minimization to fit Gaussian profiles to relevant emission lines.

Fitting the Hα-[NII] complex is of particular importance because the luminosity and FWHM of broad Hα emission can be used to estimate BH mass (Greene & Ho 2005b). The general procedure is to obtain a model for an intrinsically narrow line, then use that model to fit Hα λ6563, [NII] λ6548, and [NII] λ6583 simultaneously. We then add an additional component to model any broad excess and include this component in our model if its inclusion improves the reduced χ^2 by at least 20%. We then measure line widths and fluxes for the [NII] lines, and narrow and broad Hα.

We did not detect stellar absorption lines in the RGG 118 spectrum, so we model the continuum in each order as a line and subtract it before modeling the emission lines. We use three different methods to model the narrow line emission and find that an additional broad component for Hα is required in all three cases. We first use a single Gaussian narrow line model based on the profiles of the [SII] $\lambda\lambda$6713,6731 doublet (Model A). Next, we use a narrow line model based on the profile of [OIII] λ5007, which is also a forbidden transition. [OIII] λ5007 is significantly brighter than [SII], and can reveal the presence of wings (Mullaney et al. 2013; Zakamska & Greene 2014). Indeed, we modeled [OIII] λ5007 in two different ways and found both required a narrow core and wing component. First, we use the [SII] profile to model the core of the [OIII] line and find a wing component with FWHM$\sim 330\,\mathrm{km\,s^{-1}}$ (Model B). In the second [OIII] model we fit the core with no constraints from [SII]; this yields a wing of FWHM $\sim 192\,\mathrm{km\,s^{-1}}$ (Model C). Finally, we use each best fitting [OIII] profile as a model for the narrow line emission in the Hα-[NII] complex. See Table 3.1 for broad Hα FWHM and luminosities corresponding to each narrow line model.

Table 3.1 Broad Hα luminosities, FWHM, and BH masses for narrow line models A, B, and C

Model	$L_{\mathrm{H}\alpha}$ (erg s^{-1})	FWHM$_{\mathrm{H}\alpha}$ ($\mathrm{km\,s^{-1}}$)	BH mass ($10^4\ M_\odot$)
A	4×10^{38}	543	2.7
B	3×10^{38}	855	6.2
C	3.5×10^{38}	790	5.4

We also model the [OII] λ3727, Hβ, [OIII] λ4959 and [OI] λ6300 lines and place RGG 118 on narrow line diagnostic diagrams (Figure 3.4), and find the MagE narrow line ratios to be consistent with those found in the SDSS spectrum. A broad component was not found to be statistically justified for the Hβ emission line of RGG 118 (to be expected given the low luminosity of broad Hα and the typical Hα/Hβ intensity ratio of $\sim$3). We allow up to two Gaussians for the oxygen lines, which sometimes can exhibit broadening from the narrow line region. Figure 3.5 shows the fitted MagE spectrum, as well as a close-up of the Hα-[NII] complex for Model C.

3.4.2 Black hole mass

Strong evidence for BH accretion in RGG 118 comes from narrow emission line ratios (Figure 3.4), broad Hα emission, and a nuclear X-ray point source (see Section 3.5). Assuming the broad emission is indeed the signature of gas rotating around a nuclear BH, we can estimate the BH mass using standard virial techniques which assume the gas in the broad line region surrounding the BH is in virial equilibrium (Peterson et al. 2004; Bentz et al. 2010). The virial relationship gives $M_{\rm BH} \propto R_{\rm BLR}\Delta V^2/G$, where $R_{\rm BLR}$ is the radius of the broad line emitting region, and ΔV is a characteristic velocity of gas in the broad line region. We use the Hα emission line to estimate ΔV (Greene & Ho 2005b), and $L_{\rm H\alpha}$ as a proxy for $R_{\rm BLR}$ (Kaspi et al. 2000; Peterson et al. 2004; Greene & Ho 2005b; Bentz et al. 2009, 2013). The final equation used to estimate BH mass is given in Reines et al. (2013); we also adopt a scale factor of $\epsilon = 1$.

Each of the empirical relations used for this BH estimation technique has an associated scatter which contributes towards an uncertainty in the BH mass. Additionally, the scatter in the $M_{\rm BH} - \sigma_*$ relation ($\gtrsim 0.3$ dex; Shen & Liu 2012) also contributes to the total uncertainty, since the dimensionless scale factor ϵ is determined by calibrating the ensemble of reverberation-mapped AGN against the local $M_{\rm BH} - \sigma_*$ relation for non-active galaxies.

Summing in quadrature gives a total uncertainty of 0.42 dex (a factor of ~ 2.7).

For our three different narrow line modeling techniques (see Section 3.4.1), we obtain BH mass estimates ranging from $2.7 \times 10^4 - 6.2 \times 10^4\ M_\odot$ (Table 3.1) and thus adopt a nominal BH mass of $\sim 5 \times 10^4 M_\odot$. This is the smallest mass reported for a BH in a galaxy nucleus. Additionally, assuming a X-ray to bolometric correction of 10 (Marconi et al. 2004), we calculate a total accretion-powered luminosity $L = 4 \times 10^{40}$ erg s^{-1} for the black hole in RGG118. This corresponds to an Eddington ratio of ~ 1 per cent, similar to AGN in more massive systems.

While the broad Hα emission in typical AGN (i.e. FWHM $\gtrsim$ thousands of $\mathrm{km\,s^{-1}}$) is due to gas dominated by the gravity of a BH, some dwarf AGN have broad Hα line widths consistent with broadening from stellar processes. Thus, we have also considered the following alternate explanations for the broad Hα in RGG 118.

(i) Supernovae: The broad Balmer emission and luminosities of Type II supernovae can often cause their spectra to resemble those of AGN (Filippenko 1989). However, a supernova is a transient event; the marginal detection of broad Hα seen in the SDSS spectrum taken 6 years prior to the MagE spectrum makes this an unlikely source of the broad Hα.

(ii) Wolf-Rayet stars: Outflows from Wolf-Rayet stars can produce broad spectral features. However, the spectra of galaxies with Wolf-Rayet stars typically feature a characteristic "bump" at λ4650 – 4690 (Guseva et al. 2000); we do not observe this feature in either the SDSS or MagE spectra of RGG 118.

(iii) Luminous blue variables: Outbursts from luminous blue variables can produce broad Hα emission, but they are fainter than Type II supernovae (Smith et al. 2011a). Additionally, this phenomenon is transient and so is also ruled out by the persistent broad Hα emission of RGG 118.

We do not consider the above to be likely explanations for the detected broad Hα emission. Additional spectroscopic observations can further rule out the possibility of a stellar origin for the broad Hα emission.

3.5 X-ray analysis

A point-like X-ray source was detected at a position consistent with the SDSS position of RGG 118 (Figure 3.6; the X-ray source coordinates are R.A.: 15:23:05.0, Dec: +11:45:53.18; SDSS coordinates are R.A.: 15:23:04.97, Dec: +11:45:53.6). For the aperture photometry, we made use of CIAO SCRFLUX, which adopts a Bayesian formalism to estimate the source net count rate and corresponding flux. Source parameters were extracted from a 2″ radius circular region centered at the source peak, while a (source-free) annulus of inner and outer radius of 20 and 35″ was chosen for the background. The low number of X-ray counts did not allow for a proper spectral modeling. Assuming that the source spectrum is well represented by an absorbed power-law model with photon index $\Gamma = 1.7$ (typical of actively accreting black holes) and equivalent hydrogen column $N_{\rm H} = 3 \times 10^{20}$ cm^{-2}, the measured net count rate (1.96±0.6 $\times 10^{-4}$ counts sec^{-1} between 0.5-7 keV) corresponds to an unabsorbed flux $F_{\rm X} = 3.4 \times 10^{-15}$ erg s^{-1} cm^{-2} over the energy interval 2-10 keV (90% confidence intervals give a range from 9.1×10^{-16} erg s^{-1} cm^{-2} to 8.1×10^{-15} erg s^{-1} cm^{-2}). For a distance of 100 Mpc, this gives a hard X-ray luminosity of $L_{2-10\ \rm keV} = 4 \times 10^{39}$erg s^{-1} (90% confidence intervals give a range from 1.1×10^{39}erg s^{-1} to 9.6×10^{39}erg s^{-1}).

3.6 Imaging analysis

3.6.1 SDSS Imaging

We carried out a 2-D image decomposition of the SDSS *r*-band image using GALFIT (Peng et al. 2002, 2010). Using a two-tailed F test, we compared a single Sérsic model

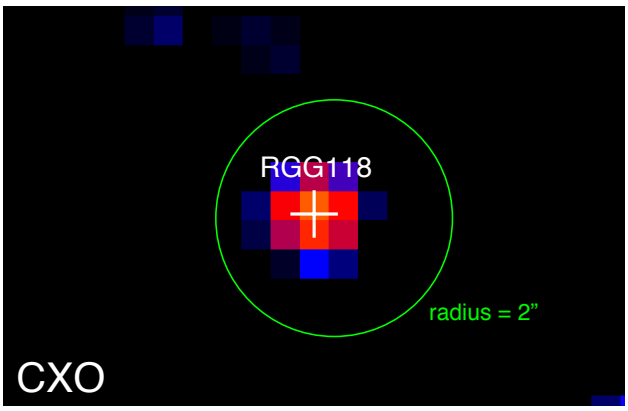

Figure 3.6 Chandra ACIS-S image of the field of view of RGG 118. An X-ray source is clearly detected at a position consistent with the nominal SDSS position (indicated by a green circle with a radius of 2″). The image has been smoothed with Gaussian kernel of $\sigma = 3$ pixels.

to a Sérsic plus exponential disk model and find that the latter is preferred (Simard et al. 2011) (the reduced χ^2 for single Sérsic model is 9.4, and the reduced χ^2 for the Sérsic plus exponential disk model is 7.2). We measure a bulge ellipticity of 0.63. Figure 3.7 shows the surface brightness profile and best-fit model.

We use the integrated g and r band magnitudes of each component to determine the r-band mass-to-light ratio (Bell et al. 2003), and calculate stellar masses of the inner and outer (exponential disk) components. Magnitudes were corrected for reddening using galactic dust extinction maps which indicate *E(B-V)* = 0.032 for RGG 118 (Schlafly & Finkbeiner 2011). For the inner Sérsic component (consistent with a pseudobulge, see Section 3.7), we measure $g - r = 0.49 \pm 0.19$, which gives $\log_{10}(\mathrm{M/L})_r = 0.23$ and $M_{*,\mathrm{inner}}$ = $10^{8.8\pm0.2} M_\odot$. For the exponential disk component we measure $g - r = 0.41 \pm 0.07$, which yields $\log_{10}(\mathrm{M/L})_r = 0.15$ and $M_{*,\mathrm{disk}}$ = $10^{9.3\pm0.1} M_\odot$. Combined, the masses of the bulge and disk are consistent with the NASA-Sloan Atlas total stellar mass of M_* = $10^{9.3} M_\odot$. We also obtain a bulge-to-disk mass ratio of ~ 0.3 based on SDSS imaging.

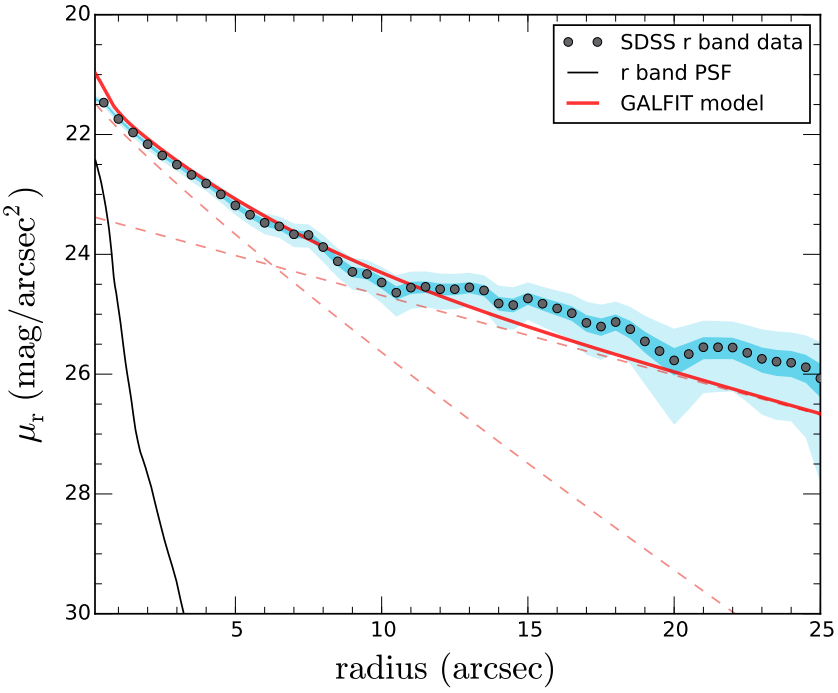

Figure 3.7 *r* band surface brightness versus radius for RGG 118. Surface brightness profile measurements from IRAF's ELLIPSE package are shown as gray dots. The dark and light blue shading represents the 1σ and 3σ uncertainties, respectively, due to the sky background. The solid black lines plot the *r*-band PSF. The solid red line shows the best-fit Sérsic+exponential disk profile as determined by GALFIT (dashed red lines are individual components).

3.6.2 HST imaging

Profile fitting

We fit the 2-D light profile of the HST imaging of RGG 118 using GALFIT (Peng et al. 2002, 2010). Fitting is performed on the image taken in the F160W filter, which has the greatest sensitivity. The best fit model is then applied to the optical filters in order to measure the total luminosity of each component. We also compare the results of the 2-D fitting to the 1-D surface brightness profile. We extract 1-D light profiles for each filter using the IRAF program *ellipse*, which fits elliptical isophotes to imaging data. Using the results of *ellipse*, we plot 1-D surface brightness profiles for RGG 118 (i.e., surface brightness as a function of semi-major axis). We also obtain measurements of the ellipticity and position angle as a function of semi-major axis from *ellipse*.

The main goal of this analysis is to decompose the 2-D light profile of RGG 118 into its individual components. Each tested model is comprised of some combination of the following components: Sérsic profile (Sérsic 1963), disk (defined as a Sérsic profile with index $n = 1$), Ferrers profile (typically used to model galaxy bars; Peng et al. 2010), and PSF. In some models, we also introduce spiral structure in the outermost component. The components used for each tested model are listed in Table 3.2.

We start by testing a model with a single Sérsic component to describe the galaxy light output, and find that a single Sérsic profile produces a poor fit. The addition of a central PSF components improves the fit, but still results in large residuals. We next consider models with two main components: an "inner" component and an "outer" component. The outer component is always described by a Sérsic profile, the index of which is either free to vary or restricted to the canonical disk value of $n = 1$. We also consider spiral structure in the outer profile. The inner component is either modeled with a Sérsic or modified Ferrers profile.

Each combination of inner and outer component is also tested with and without a central PSF component; in all cases, the inclusion of a central PSF improves the χ^2 value by more than 40%. Table 3.2 lists each tested model and its corresponding χ^2 value, computed by comparing the intensity as a function of semi-major axis for the model and data. Ultimately, we find the best-fit model to include an outer disk ($n = 1$) with spiral structure, an inner Sérsic component with $n = 0.8 \pm 0.01$, and a central PSF (see Figure 3.8). The best-fit parameters (Sérsic index, effective radius, effective surface brightness) for this model are given in Table 3.3. Figure 3.9 shows the Sérsic+Spiral Disk+PSF model applied to the F475W and F775W filters. In applying the model to the F475W and F775W bands, all components were held fixed except the magnitude of each component. The position of the PSF was also allowed to vary.

The magnitudes of each component in each filter for our best-fit model are reported in Table 3.4. As noted in the GALFIT documentation [2], the errorbars returned by GALFIT rely on the assumptions that the residuals are due only to Poisson noise, and the noise has a Gaussian distribution. Similar to the procedure described in Shangguan et al. (2016), we estimate errors on the magnitude using the standard deviation of the sky background. The standard deviation is computed by measuring the median sky value in a series of 50x50 pixel boxes placed in the sky regions surrounding the galaxy.

Colors and stellar masses

Using the g, i, and H-band magnitudes from GALFIT and extinction corrections based on the extinction map from Schlafly & Finkbeiner (2011), we find the $g - i$ color and H-band luminosity for the outer disk and inner Sérsic components. For the inner component, we find $(g - i)_{\rm bulge} = 1.18^{+0.48}_{-0.40}$. The disk is faint in the g and i bands, and the errors on the disk magnitudes returned from GALFIT are large (they give $(g - i)_{\rm disk} = -0.01^{+1.1}_{-1.2}$).

[2] https://users.obs.carnegiescience.edu/peng/work/galfit/galfit.html

Table 3.2. GALFIT fitting results

Components	χ^2	M_{F160W} (PSF)
Sérsic	347.77	–
Sérsic + PSF	33.09	21.92 $\pm$0.02
Sérsic + Sérsic	353.31	–
Sérsic + Sérsic + PSF	6.05	22.00$\pm$0.03
Sérsic+ Disk	281.56	–
Sérsic + Disk + PSF	11.51	22.06$\pm$0.03
Ferrers + Sérsic	83.37	–
Ferrers + Sérsic + PSF	74.09	22.22 $\pm$0.03
Ferrers + Disk	82.88	–
Ferrers + Disk + PSF	64.83	22.25$\pm$0.03
Sérsic + Spiral Sersic + PSF	11.46	22.05$\pm$0.03
Sérsic + Spiral Disk + PSF	3.97	22.02$\pm$0.03

Note. — Model components and corresponding chi-squared values for each GALFIT trial. For all models except Sérsic + Spiral Disk + PSF (shown in Figure 3.8). Errors on the PSF are those reported by GALFIT.

Table 3.3. Best fit model parameters

Inner Sérsic component				Outer disk			
$r_{\rm eff}$ (kpc)	$\mu_{\rm eff}$ (mag/arcsec^2)	n	(b/a)	$r_{\rm eff}$ (kpc)	$\mu_{\rm eff}$ (mag/arcsec^2)	n	(b/a)
1.57	22.5	0.80	0.45	6.51	24.1	1.00 (fixed)	0.69

Note. — Best fit model parameters (effective radius, surface brightness at the effective radius, Sérsic index, and axis ratio) for the Sérsic + Spiral Disk + PSF model in the F160W filter.

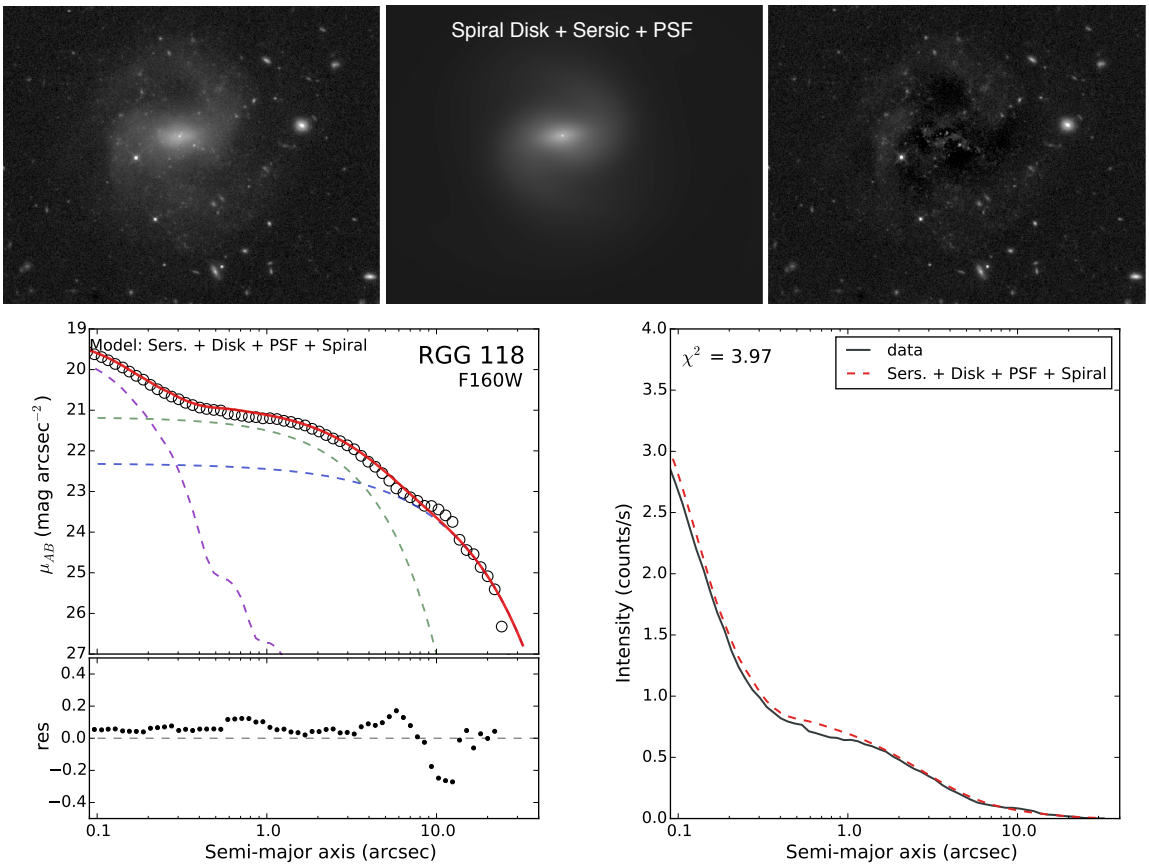

Figure 3.8 Top row: Image of RGG 118 in the F160W filter (left); best fitting GALFIT model including a PSF, inner Sérsic component, and outer spiral disk (middle); residuals (right). Bottom row: Left panel shows the observed surface brightness profile of RGG 118 as open circles. The overall best-fit GALFIT model is shown in red, and is comprised of a PSF (purple dashed line), inner Sérsic component (green dashed line) and outer disk (blue dashed line). The residuals are shown below the surface brightness profile. Right panel shows the average intensity along a given isophote from the data and the intensity as a function of radius for the best-fit GALFIT model. Scale and colormap are consistent between the images.

Table 3.4. AB magnitude of individual components

Filter	PSF (mag)	Inner component (mag)	Disk (mag)
F475W	$22.56^{+0.37}_{-0.28}$	$19.38^{+0.36}_{-0.27}$	$17.49^{+0.65}_{-0.40}$
F775W	$22.37^{+0.38}_{-0.28}$	$18.20^{+0.13}_{-0.12}$	$17.48^{+0.82}_{-0.46}$
F160W	20.02 ± 0.02	$18.31^{+0.09}_{-0.08}$	$16.42^{+0.14}_{-0.12}$

Note. — AB magnitude of each component in the best-fitted model (Sérsic + Spiral Disk + PSF) for each filter. Modeling was performed on the F160W filter, and the best-fitted model was applied to the two optical filters.

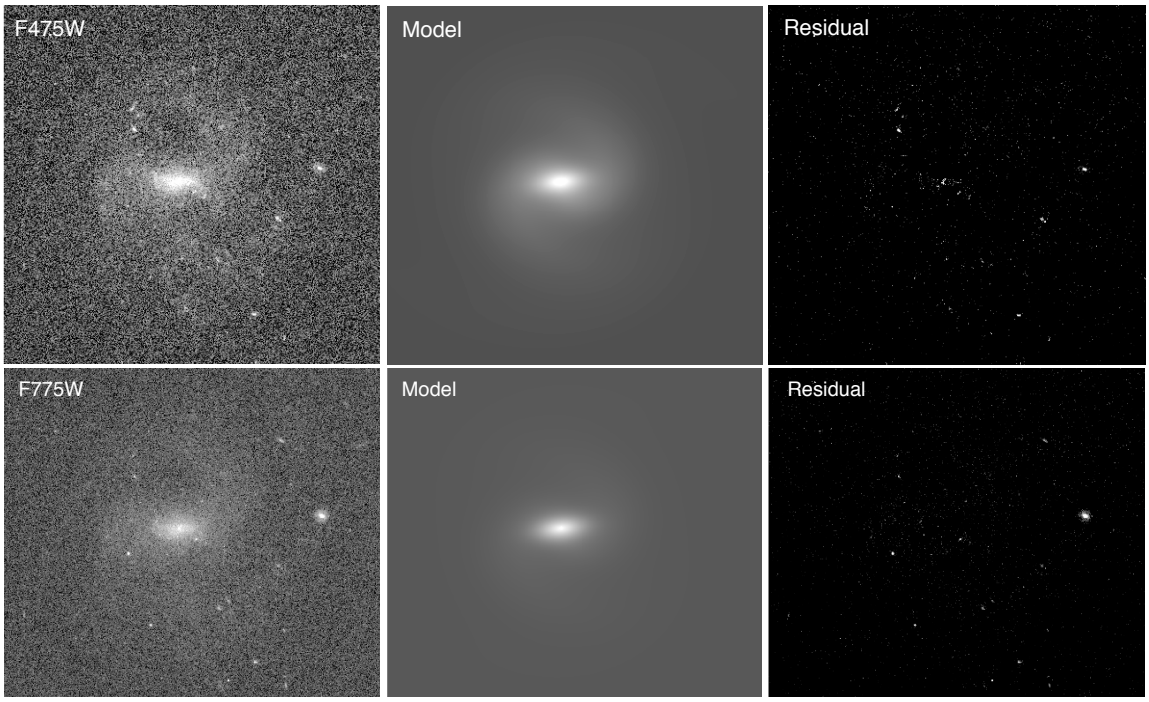

Figure 3.9 Best-fit model as determined from the F160W data applied to the F475W (top row) and F775W (bottom row) images. For each filter, the scale and colormap are consistent between the images .

An alternate way to try to constrain the disk color is using the 1-D light profiles output by *ellipse*. Using the total flux enclosed in an annulus between 10″ and 16″, i.e., where the disk is dominant, we find $(g-i)_{\rm disk} = 0.5 \pm 0.3$.

We show the $g-i$ (F475W-F775W) color evolution of single stellar population with initial mass of 10^8 solar masses using GALEV (Kotulla et al. 2009) and show the results in Figure 3.10 for a solar-metallicity model and sub-solar metallicity model. While treating the bulge and disk as single stellar populations is a significant simplification, we can nevertheless get a rough idea of the relative ages of the bulge and disk. A disk with $(g-i) \approx 0.0$ would be dominated by young stellar populations with ages of tens to hundreds of Myr. The observed bulge color suggests a population that is older than ~ 1 Gyr. We also show the color evolution for an Sa-galaxy with total mass of $5 \times 10^9 M_\odot$ in Figure 3.10.

We compute the stellar mass of each component using the color-based mass-to-light

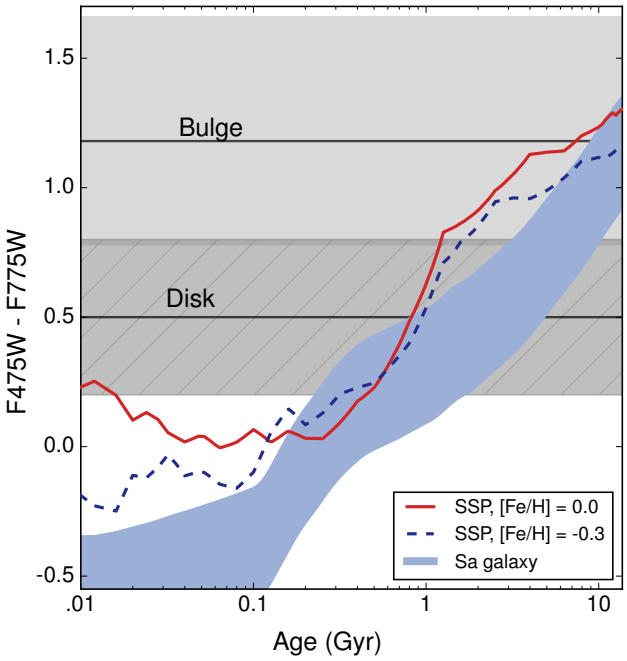

Figure 3.10 F475W - F775W color versus stellar population age. The solid red and dashed blue lines represent models for the extinction-corrected color evolution of a single stellar population with initial stellar mass of $10^8 M_\odot$. The solid red line shows the evolution of a population with solar metallicity, while the dashed blue shows a population with sub-solar metallicity ($[\mathrm{Fe/H}] = -0.3$, or roughly half the metallicity of the Sun). The gray horizontal lines show the color of the bulge and disk, and the shaded regions encompass the errors. The light blue shaded region encompasses evolutionary tracks for an Sa-galaxy with a *total* mass of $5 \times 10^9 M_\odot$ and chemically consistent metallicity. Models for this galaxy were computed for E(B-V) ranging from 0.0 to 0.5; increasing E(B-V) increases (reddens) the F475W-F775W color. All evolutionary tracks were computed using GALEV (Kotulla et al. 2009).

ratios derived by Bell et al. (2003). We measure the luminosity using our F160W observations (roughly the equivalent of H band), since the variation in M/L is decreased at NIR wavelengths. We use the $(g-i)$ color to compute the $\log(\mathrm{M/L}_H)$ ratio Υ_H. The resulting equation is $\Upsilon_H = -0.186 + (0.179 \times (g-i))$. We compute a disk stellar mass of $M_{*,disk} = 10^{9.13(+0.27,-0.25)} M_\odot$ and an inner component stellar mass of $M_{*,bulge} = 10^{8.59(+0.11,-0.12)} M_\odot$. This gives a total stellar mass of $M_{*,total} = 10^{9.24(+0.38,-0.37)} M_\odot$.

3.6.3 Comparison of SDSS and HST imaging analyses

We find consistent bulge/disk/total stellar masses between our SDSS and HST imaging analyses. We do find a slightly lower Sérsic index for the inner component based on

modeling of the HST data than for the SDSS data ($n = 0.8$ in this work compared to $n = 1.13 \pm 0.26$).

The SDSS imaging was subsequently analyzed by Graham et al. (2016). They use 1-D modeling techniques to model the profile of RGG 118. Graham et al. (2016) include spheroid (bulge), bar, and disk components, and find that a central PSF is not required for their model. Their bar component is fit with a modified Ferrers profile, while their bulge is fit with a Sérsic component of n=0.41. Our attempts to model the RGG 118 light profile with a bulge, bar, and disk did not converge on a solution in GALFIT.

One potential explanation for our differing preferred models is that their spheroid component has an effective radius of 0.63″, less than the typical FWHM of the SDSS r-band PSF (1.3″), making it difficult to distinguish their bulge from a point source. We are able to find best-fit solutions for models including a point source, bar, and disk, though these have higher χ^2 values than models without a bar (Table 3.2). Graham et al. (2016) find the stellar masses of the disk, bar, and bulge to be $10^{9.36} M_\odot$, $10^{7.76} M_\odot$, and $10^{7.92} M_\odot$, respectively. Their total stellar mass is consistent with our findings, though the masses of the individual components are not. Overall, we find models included Ferrers (bar) components to produce poorer fits to the HST data.

The presence of a bar can also be assessed using the ellipticity and position angle profiles of RGG 118 (Figure 3.11). Menéndez-Delmestre et al. (2007) describe several signatures produced by a bar. Within the bar, there is typically a continuous increase in ellipticity with a fixed position angle. At the end of the bar, there is an abrupt drop-off in ellipticity and a sharp change in position angle as the profile moves from bar-dominated to being dominated by the disk. We do not find evidence for a bar in either the ellipticity or position angle profile of RGG 118.

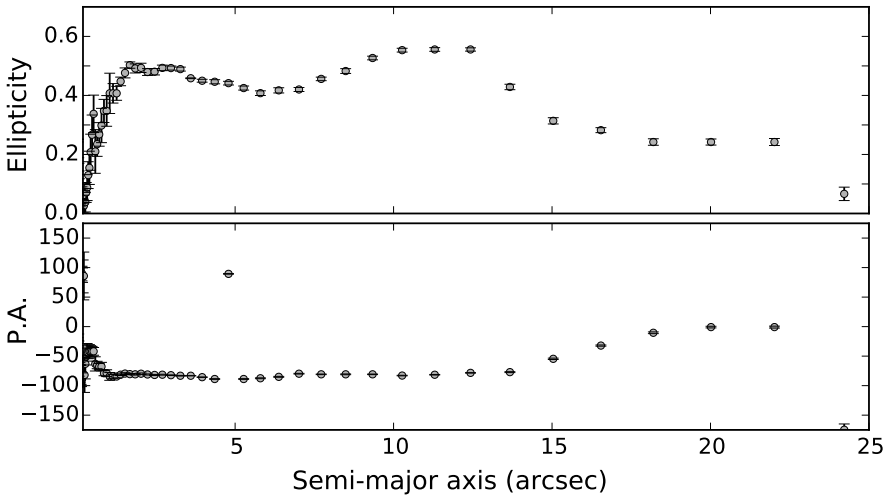

Figure 3.11 Position angle and ellipticity profile of RGG 118. Signatures of a bar are an increase in ellipticity with fixed position angle within the bar, followed by a sharp drop off in ellipticity coincident with a change in position angle. We do not observe these features for RGG 118.

3.7 Scaling relations

There are well known scaling relations between BH mass and bulge properties such as stellar velocity dispersion (Ferrarese & Merritt 2000; Gebhardt et al. 2000a; Gültekin et al. 2009; McConnell & Ma 2013), stellar mass (Marconi & Hunt 2003; Häring & Rix 2004), and near-infrared luminosity (Marconi & Hunt 2003). These relations imply that the BH and galaxy co-evolve despite the small gravitational sphere of influence of the BH relative to the galaxy. In this section, we discuss the importance of constraining the low-mass end of scaling relations and explore the position of RGG 118 on scaling relations between BH mass and host galaxy properties.

Cosmological simulations suggest that the BH occupation fraction in low-mass galaxies, as well as the slope and scatter of the low-mass end of BH-galaxy scaling relations are related to the primary mechanism by which BH seeds form in the early universe (Volonteri & Natarajan 2009). BH seed formation models tend to fall into two categories: light seeds ($M_{\rm BH,seed} \approx 100\ M_{\odot}$) and heavy seeds ($M_{\rm BH,seed} \approx 10^{4-5}\ M_{\odot}$). In light seed models,

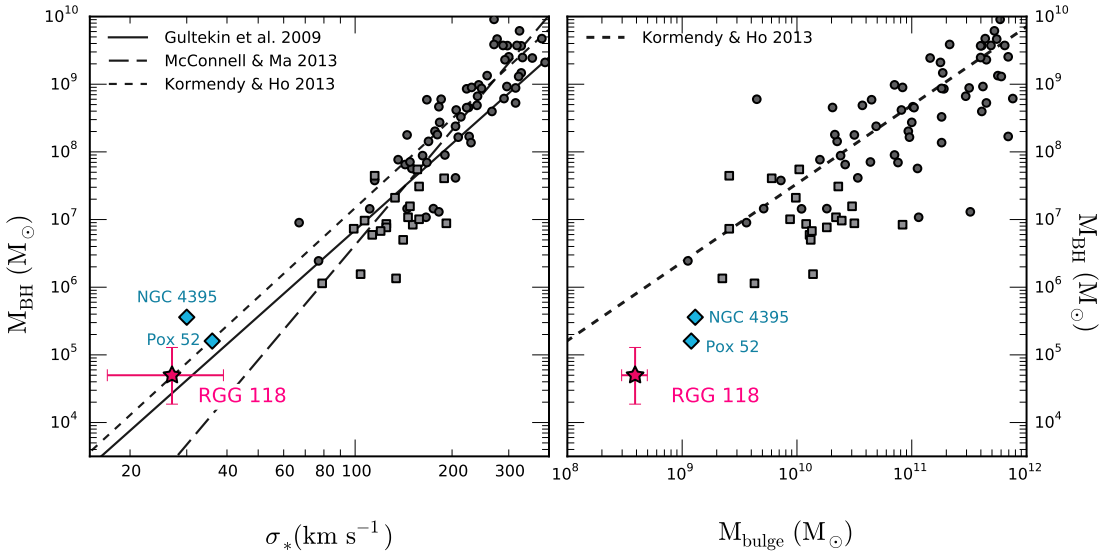

Figure 3.12 Position of RGG 118 on black hole-host galaxy scaling relations. *Both*: Black solid/dashed lines represent various determinations of scaling relations. Circles and squares represent systems having dynamically measured BH masses (Kormendy & Ho 2013) with classical and pseudobulges, respectively. *Left*: $M_{\rm BH} - \sigma_*$ relation. RGG 118 is plotted as the pink star. Error bars on the mass account for the scatter in the correlations used to determine the BH mass; velocity dispersion errors include scatter in the relation between stellar and gas velocity dispersion (Barth et al. 2008). We also show the well-studied dwarf AGN POX 52 (Barth et al. 2004; Thornton et al. 2008) and NGC 4395 (Filippenko & Ho 2003) (turquoise diamonds). For NGC 4395, which is bulgeless, the velocity dispersion is an upper limit and refers to the nuclear star cluster (Filippenko & Ho 2003). *Right*: Dashed black line gives the $M_{\rm BH} - M_{\rm bulge}$ relation. Total masses are plotted for POX 52 (Thornton et al. 2008), and NGC 4395 (Filippenko & Ho 2003).

BH seeds form from the deaths of Population III stars (Madau & Rees 2001; Alvarez et al. 2009; Madau et al. 2014). These models predict a plume of objects which scatter *below* the present-day M-σ relation at low galaxy/BH masses. On the other hand, heavy seed models (Begelman et al. 2006; Lodato & Natarajan 2006) produce BH seeds via direct collapse of gas clouds and predict that objects at the low-mass end of M-σ should scatter *above* the relation.

We find that RGG 118 falls on the extrapolation of the $M_{\rm BH} - \sigma_*$ relation to low BH masses, but falls an order of magnitude below the $M_{\rm BH}$–$M_{\rm bulge}$ relation (Figure 3.12). We did not detect stellar absorption lines in the spectra of RGG 118, so instead use the gas velocity dispersion as a proxy for stellar velocity dispersion; the two have been shown to cor-

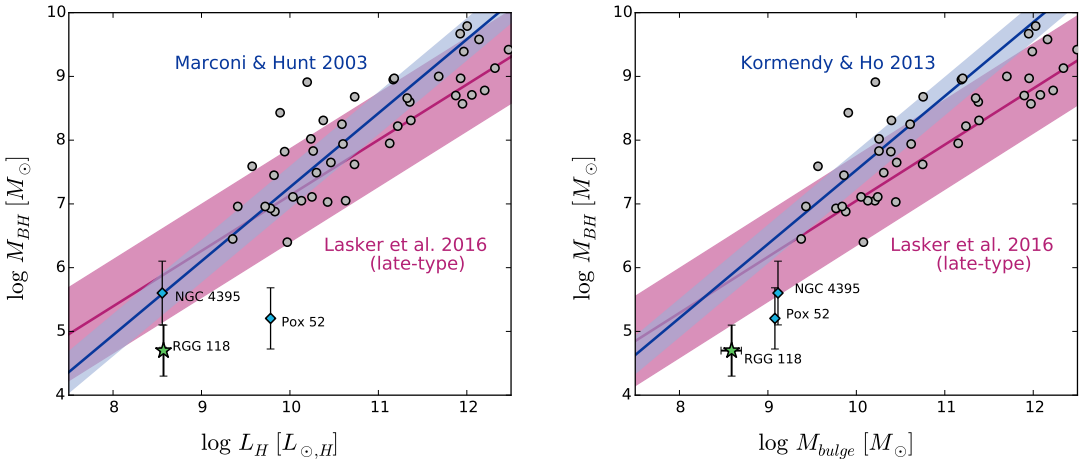

Figure 3.13 Scaling relations between bulge properties and BH mass. *Both panels:* The green star represents RGG 118, and the gray circles show galaxies from Läsker et al. (2014) and Läsker et al. (2016). We also show the positions of NGC 4395 (Filippenko & Ho 2003; den Brok et al. 2015) and Pox 52 (Barth et al. 2004; Thornton et al. 2008). Note that NGC 4395 is bulgeless, so the "bulge" stellar mass and luminosity refer to the entire galaxy. WFC3 H-band luminosities for NGC 4395 and Pox 52 are computed by transforming their 2MASS H-band luminosities via the relations given in Riess (2011). The pink lines and shading show the scaling relations derived by Läsker et al. (2016) including the offsets found for their late-type galaxy sample relative to the full sample. *Left:* M_{BH} versus $L_{\rm bulge,H}$. The blue line and shaded region show the $L_{\rm bulge} - M_{BH}$ relation and intrinsic scatter from Marconi & Hunt (2003). *Right*: M_{BH} versus $M_{\rm bulge}$. The blue line and shaded region show the $M_{\rm bulge} - M_{BH}$ relation and scatter from Kormendy & Ho (2013).

relate, though the scatter in the relation is ~ 0.15 dex (Barth et al. 2008; Xiao et al. 2011). Using the [NII] line, we measure a gas velocity dispersion of $\sigma_{\rm [NII]} = 27\,{\rm km\,s^{-1}} \pm 5\,{\rm km\,s^{-1}}$, after correcting for instrumental dispersion. This yields a stellar velocity dispersion estimate of $\sigma_* = 27^{+12}_{-10}\,{\rm km\,s^{-1}}$, after adding uncertainties in quadrature.

From HST imaging, we compute a bulge mass of $M_{*,bulge} = 10^{8.59(+0.11,-0.12)} M_\odot$ for RGG 118; this gives a $\rm M_{BH}$-$\rm M_{bulge}$ ratio of $\sim 10^{-4}$ and places RGG 118 roughly an order of magnitude below the $\rm M_{BH}$-$\rm M_{bulge}$ relation (right panel of Figure 3.12). We also show the position of RGG 118 relative to relations between BH mass and bulge IR luminosity (Figure 3.13). In Figure 3.13 we also show scaling relations derived for spiral galaxies by Läsker et al. (2016); the BH in RGG 118 appears to be under-massive with respect to these as well.

There has been considerable discussion regarding whether galaxies without classical

bulges follow scaling relations. Kormendy & Ho (2013) find that the properties of galaxies with pseudobulges (i.e., flatter, rotationally supported components with Sérsic indices $n < 2.0$; Kormendy & Kennicutt 2004) do not correlate with BH mass. In fact, galaxies with pseudobulges tend to scatter below the $M_{\rm BH} - M_{\rm bulge}$ relation, such that their BHs are under-massive with respect to the mass of the (pseudo)bulge (Greene et al. 2010). With a Sérsic index of $n = 0.8$, the central component of RGG 118 is more consistent with a pseudobulge than a classical bulge. Baldassare et al. (2015) find that RGG 118 does sit below the $M_{\rm BH} - M_{\rm bulge}$ relation defined by early-type galaxies; our results based on *HST* imaging are consistent with this. For the bulge mass of RGG 118 ($10^{8.59} M_{\odot}$), the relation given by Kormendy & Ho (2013) predicts a BH mass of $\sim 8 \times 10^5 M_{\odot}$, or 0.2% of the bulge mass. The BH in RGG 118 is in actuality roughly an order of magnitude smaller. We also find that RGG 118 sits below the relation between BH mass and IR bulge luminosity. In Figure 3.7 we show the position of RGG 118 relative to the $M_{\rm BH} - M_{\rm bulge}$ and $M_{\rm BH} - L_{\rm bulge}$ relations.

Our result is consistent with those of Greene et al. (2008) (followed by Jiang et al. 2011a,b) suggesting a break-down in scaling relations for low-mass ($M_{\rm BH} < 10^6 M_{\odot}$) BHs. Recent work by Reines & Volonteri (2015) showed that nearby AGNs (including dwarf AGNs) fall systematically $\sim$ an order of magnitude below quiescent galaxies on the relation between total galaxy stellar mass and BH mass. This is potentially driven by a difference in host galaxy properties; they find a significant fraction of the AGN host galaxies are in spiral/disk galaxies.

There are several possible explanations for why bulgeless/disk-dominated galaxies or those with pseudobulges do not correlate with BH mass in the same way as galaxies with classical bulges. Kormendy & Ho (2013) (see also Greene et al. 2008; Jiang et al. 2011a) suggest that there are two different modes of BH growth: one in which a merger drives

copious amounts of gas towards the center, growing the BH rapidly, and a second where BH growth is a local, stochastic process. The first mechanism would be relevant for BHs in bulge-dominated/elliptical galaxies, while BHs in disk-dominated galaxies would grow via the second mode. This is consistent with a picture in which the BHs in disk-dominated and/or pseudobulge galaxies are undermassive with respect to the scaling relations defined by relatively massive, classical bulge-dominated systems.

3.8 Conclusions

We present multi-wavelength observations of the dwarf galaxy RGG 118, first identified as having composite narrow-line ratios by Reines et al. (2013). Our MagE spectroscopy confirms narrow-line evidence for an AGN, and reveals the presence of a broad Hα emission feature characteristic of dense gas orbiting around a BH. From the Hα emission, we measure a BH mass of $\sim 50,000$ solar masses – the smallest BH yet reported in a galaxy nucleus. We also show that RGG 118 sits on the extrapolation of the $M_{\rm BH} - \sigma_*$ to low BH/galaxy masses.

Chandra X-ray observations reveal a hard nuclear point source, which provides further confirmation of an AGN in RGG 118. Additionally, we use the X-ray luminosity to estimate the Eddington fraction, finding that the BH in RGG 118 is accreting at $\sim 1\%$ of its Eddington luminosity.

Finally, we find that the light profile of RGG 118 is well described by an outer spiral disk, an inner Sérsic component with a stellar population older than ~ 1 Gyr, and properties consistent with a pseudobulge, and a central point source. We confirm that RGG 118 sits well below scaling relations between BH mass and bulge mass/luminosity, similar to other low-mass, disk-dominated systems.

CHAPTER IV

X-ray and ultraviolet properties of AGN in dwarf galaxies

4.1 Motivation and Aims

This chapter presents an analysis of new Chandra X-ray and Hubble Space Telescope UV observations of eight dwarf galaxies identified by Reines et al. (2013) as having broad emission lines in their SDSS spectra. This chapter is based on results published in Baldassare et al. (2017). Of these eight objects, seven also have narrow emission-line evidence for AGNs. The goals of this analysis were to characterize X-ray emission from AGNs in dwarf galaxies and to study their accretion properties. We find that all galaxies in our sample have X-ray detected nuclei. For all objects with broad and narrow emission line evidence for an AGN, the X-ray emission is brighter than would be expected from X-ray binaries. Additionally, we find that the AGN are accreting at high Eddington fractions (0.1-50%), similar to more massive AGNs at high redshift. Finally, we explore the ratio of UV to X-ray emission, and find that these AGNs are relatively X-ray weak compared to more massive AGNs.

4.2 Introduction

In the last few years, the number of active galactic nuclei (AGN) identified in dwarf galaxies (i.e., $M_* \lesssim 3 \times 10^9 M_\odot$) has grown from a handful of quintessential examples (e.g., NGC 4395; Filippenko & Sargent 1989, and POX 52; Barth et al. 2004) to a body of

several hundred candidates (see Reines & Comastri (2016) for a review). This has largely been possible thanks to large scale optical spectroscopic surveys (e.g., the Sloan Digital Sky Survey; SDSS), which have facilitated the search for AGN signatures in samples of tens of thousands of galaxies (see e.g. Greene & Ho 2004, 2007; Dong et al. 2012a), with the most recent studies concentrating on *bona-fide* dwarf galaxies (Reines et al. 2013; Moran et al. 2014; Sartori et al. 2015). In particular, the most successful searches for AGN in dwarf galaxies have used narrow emission line diagnostics (e.g., the BPT diagram; Baldwin, Phillips & Terlevich 1989) to search for photo-ionized gas consistent with the presence of an AGN (see also Kauffmann et al. 2003; Kewley et al. 2006 for commonly used diagnostics).

For AGN exhibiting broad Hα emission, assuming that the broad line region gas is virialized, it is possible to estimate the mass of the central BHs. Note that, for AGN in dwarf galaxies, this also relies on the assumption that the scaling relation between BH mass and host stellar velocity dispersion (Ferrarese & Merritt 2000; Gebhardt et al. 2000a) holds in this mass regime (Bentz et al. 2016). The velocity of the broad line region gas is estimated from the width of the Hα line, and the radius to the broad line region is estimated from the luminosity of the broad emission (Kaspi et al. 2000; Peterson et al. 2004; Greene & Ho 2005b; Bentz et al. 2009, 2013). BH masses in dwarf AGN are typically $\sim 10^5 - 10^6 M_\odot$ solar masses (see e.g., Reines et al. 2013, Baldassare et al. 2016), with the lowest reported having a mass of just $\sim 50,000 M_\odot$ (Baldassare et al. 2015).

Despite these recent advances in the identification of AGN in dwarf galaxies, the radiative properties of this population of AGN as a whole are largely unconstrained. Much work has been done exploring the X-ray properties of $\sim 10^6 M_\odot$ optically selected AGN from the Greene & Ho samples (Desroches et al. 2009; Dong et al. 2012a; Plotkin et al.

2016), but these host galaxies tend to be more massive than the dwarf galaxies considered here. Stacking analyses have been used to detect X-ray emission in dwarf galaxies out to z $\approx$ 1.5 (Mezcua et al. 2016; Paggi et al. 2016). Additionally Pardo et al. (2016) used X-ray observations to search for AGN in dwarf galaxies at z < 1, finding an AGN fraction of $\sim 1\%$. However, we are concerned with following up individual systems in order to obtain a detailed look at the radiative properties of this relatively unexplored population.

Determining the radiation properties of actively accreting BHs at the cores of dwarf galaxies is important for several reasons. Firstly, the BHs at the centers of dwarf galaxies may provide clues about galaxy nuclei in the early universe, since they are expected to be similar (to first approximation; see, e.g., Bellovary et al. 2011; Habouzit et al. 2016). With current instrumentation, it is not possible to detect $10^5 M_\odot$ BHs in the earliest galaxies. A BH of this size accreting at its Eddington limit has a bolometric luminosity of $\sim 10^{43}$ erg s^{-1}. Assuming it releases $\sim 10\%$ of its energy in hard X-rays, the flux reaching us would be an order of magnitude below the detection limit of the 4 Ms Chandra Deep Field South (which has a 2-8 keV flux limit of 5.5×10^{-17} erg s^{-1} cm^{-2}; Xue et al. 2011). Furthermore, searches for AGN at high redshift (z > 6) find fewer sources than expected based on relations at lower redshift (Weigel et al. 2015), possibly due to the lower normalization for low-mass galaxies in the BH mass-galaxy stellar mass relation (Reines & Volonteri 2015; Volonteri & Reines 2016). As an alternative, present-day dwarf galaxies can serve as useful local analogs (Jia et al. 2011; Reines et al. 2011, 2014). Present day dwarf galaxies have likely not undergone any major mergers, and are thus relatively undisturbed and "pristine" compared to more massive systems.

Moreover, studying AGN in dwarf galaxies is useful for understanding the interplay between AGN activity and star formation on all galaxy scales. AGN feedback is expected to have an effect on galaxy scale star formation, particularly in more massive systems

(e.g., King & Pounds 2015). Feedback from massive stars and/or supernovae is expected to be particularly relevant for dwarf galaxies, but it is unclear what (if any) influence AGN can have on star formation in these smaller systems (Murray et al. 2005; Hopkins et al. 2010, 2014, 2016). Studying radiation from AGN in dwarf galaxies is also useful for understanding whether BH accretion had any influence on star formation in the earliest galaxies (see e.g., Alexandroff et al. 2012), as well as for investigating the contribution of low luminosity AGN to reionization (Milosavljević et al. 2009; Madau & Haardt 2015).

High resolution X-ray and UV follow-up of these systems is essential for understanding the accretion properties of AGN in dwarf galaxies. If detected, sufficiently bright, point-like nuclear UV/X-ray emission provides strong confirmation of the presence of an AGN (e.g., Elvis et al. 1994). Additionally, X-ray studies can be used to determine the distribution of Eddington ratios for AGN in dwarf galaxies. Furthermore, the relative strength of the UV and X-ray emission is important for learning about the structure and properties of the accretion disk and corona (Tananbaum et al. 1979; Lusso & Risaliti 2016). Finally, studies of the broad-band spectra of these objects is necessary for determining the bolometric correction for this class of AGN.

Reines et al. (2013) identified 151 dwarf galaxies with narrow and/or broad emission line signatures indicating the presence of an AGN. With the above goals in mind, we analyze *Chandra X-ray Observatory* observations of a sub-sample of these objects, focusing on the most promising broad-line AGN candidates. In Section 4.3, we discuss our sample, X-ray and UV observations, and data reduction and analysis. In Section 4.4, we report on properties of the X-ray and UV emission, including the ratio of X-ray to UV emission. In Section 4.5, we discuss the origin of the X-ray emission, and compare the properties of our galaxies to more massive quasars.

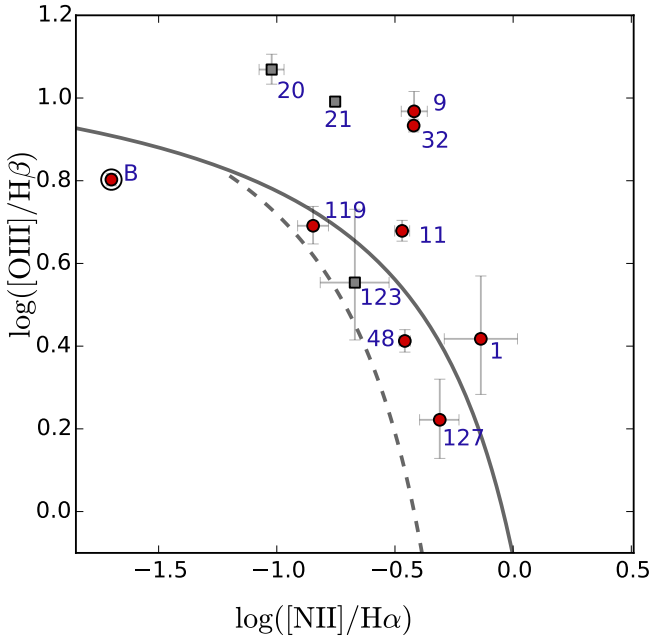

Figure 4.1 Location of our targets on the BPT diagram. Red circles represent objects with new *Chandra* observations, while gray squares represent objects with archival X-ray observations. The sole BPT star forming object is our sample is RGG B; in this plot and others in this paper, this object is surrounded by an open circle for clarity.

4.3 Observations and Analysis

Reines et al. (2013) identified 10 dwarf galaxies with both narrow *and* broad emission line AGN signatures. Of these, six fall in the "AGN" region of the BPT diagram, and four fall in the "composite" region. Composite objects are expected to have contributions to narrow line emission from both an AGN and recent star formation. The 10 galaxies include the well-studied NGC 4395 (RGG[1] 21), as well as two objects (RGG 20 and 123) identified in the Greene & Ho (2007) catalog and followed up in Dong et al. (2012a) (see Section 4.3.3). Figure 4.1 shows the location of our sample on the BPT diagram.

We have obtained new *Chandra X-ray Observatory* and *Hubble Space Telescope* (HST) Wide-Field Camera 3 (WFC3) ultraviolet observations (Proposal ID: 16700103, PI: Reines) of the remaining seven. Additionally, we observed RGG B, a dwarf galaxy identified by

[1]RGG refers to the ID assigned by Reines, Greene & Geha (2013).

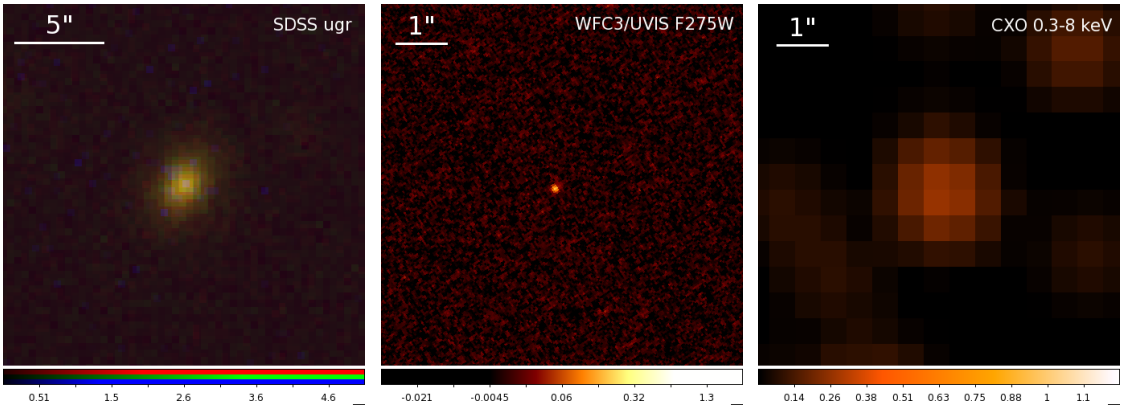

Figure 4.2 Optical, UV, and X-ray imaging of RGG 1. The leftmost panel is a three-color SDSS image, using u, g, and r bands as blue, green, and red, respectively. The center panel shows the HST WFC3/UVIS image taken with the F275W filter. The rightmost panel shows the *Chandra X-ray Observatory* image, smoothed with a Gaussian kernel with radius of 3 pixels. At the median sample redshift of $z = 0.04$, $1''$ corresponds to ~ 850 pc.

Reines et al. (2013) to have broad Hα emission but narrow-line ratios consistent with photoionization from HII regions. However, this object's narrow line ratios place it on the upper left of the star forming region of the BPT diagram, a regime where it is thought low-metallicity AGN can reside (Groves et al. 2006). In all, our full sample is comprised of 11 objects, three of which have *Chandra* observations analyzed in the literature, and eight of which have new *Chandra*/HST observations analyzed in this work. We stress that with our new observations, we complete high-resolution X-ray follow-up for all secure broad-line AGN identified in Reines et al. (2013).

All targets are nearby ($z < 0.055$), and stellar masses range from $\sim 1\times10^8-3\times10^9\ M_\odot$ (see Tables 1 and 3 in Reines et al. 2013). Stellar masses are computed using the kcorrect software (Blanton & Roweis 2007), and taken from the NASA-Sloan Atlas. Figures 4.2 through 4.9 show, for each of our eight new targets, the three-color SDSS image, the HST UV image, and the CXO image.

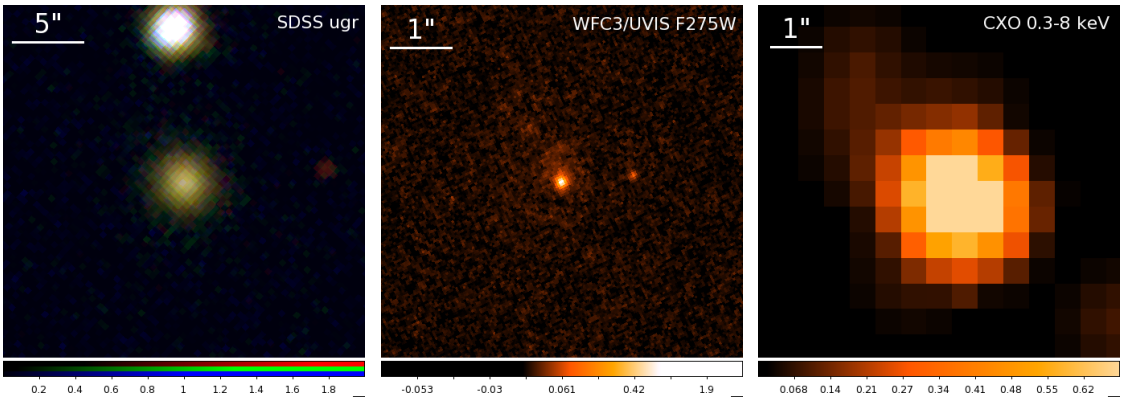

Figure 4.3 Optical, UV, and X-ray imaging of RGG 9. See Figure 4.2 for a more detailed description.

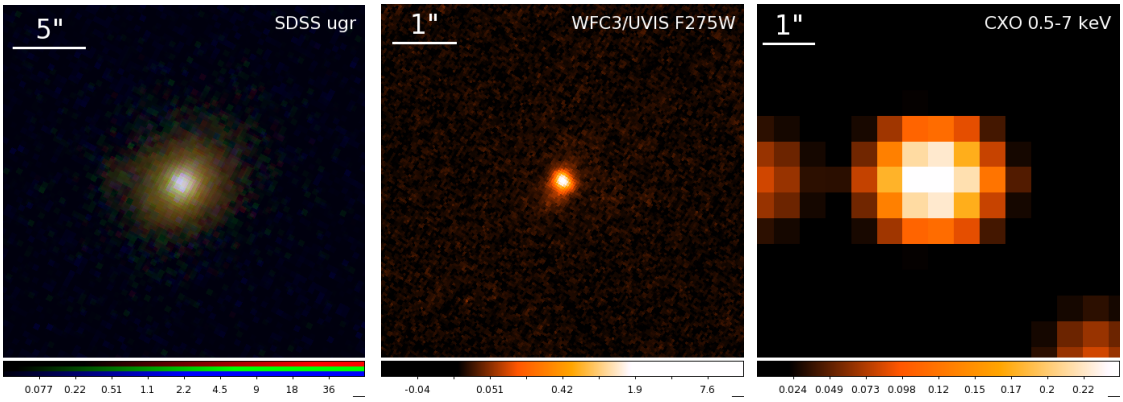

Figure 4.4 Optical, UV, and X-ray imaging of RGG 11. See Figure 4.2 for a more detailed description.

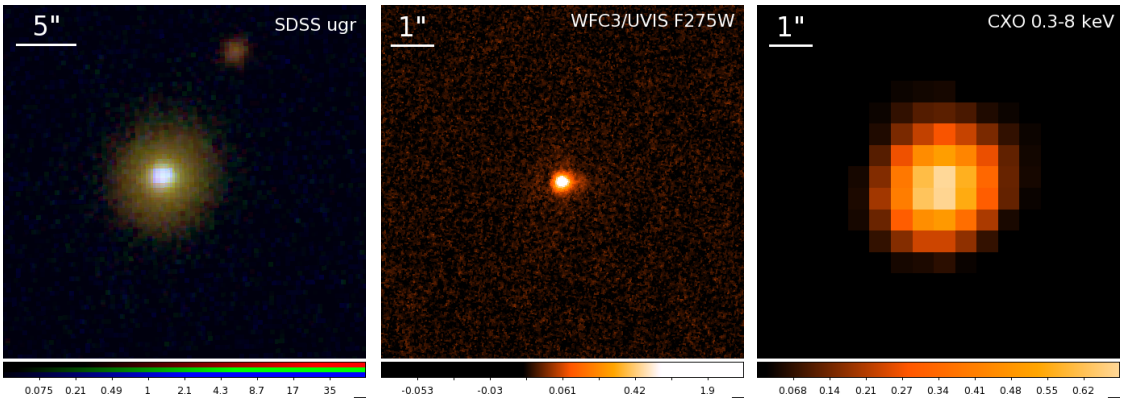

Figure 4.5 Optical, UV, and X-ray imaging of RGG 32. See Figure 4.2 for a more detailed description.

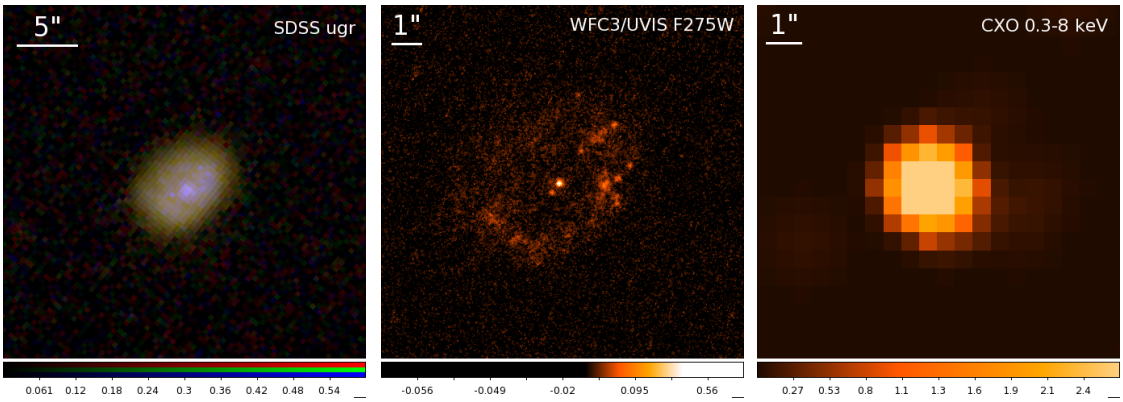

Figure 4.6 Optical, UV, and X-ray imaging of RGG 48. See Figure 4.2 for a more detailed description.

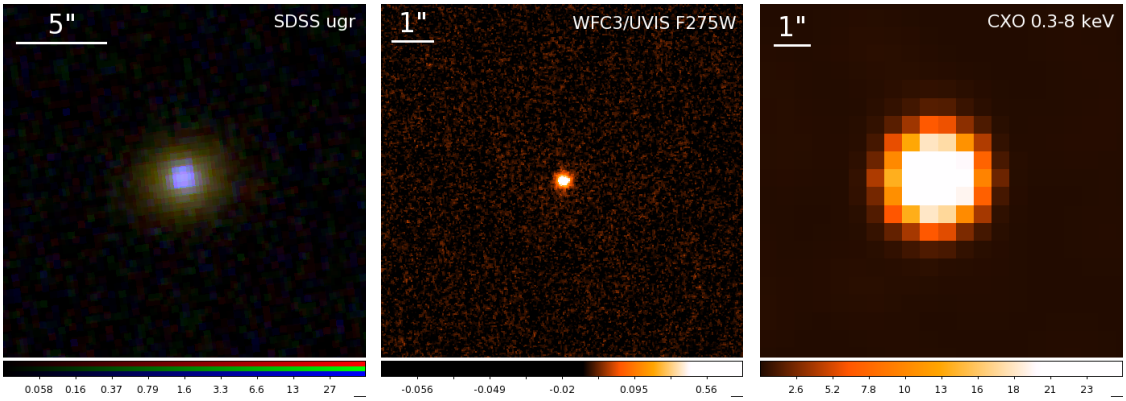

Figure 4.7 Optical, UV, and X-ray imaging of RGG 119. See Figure 4.2 for a more detailed description.

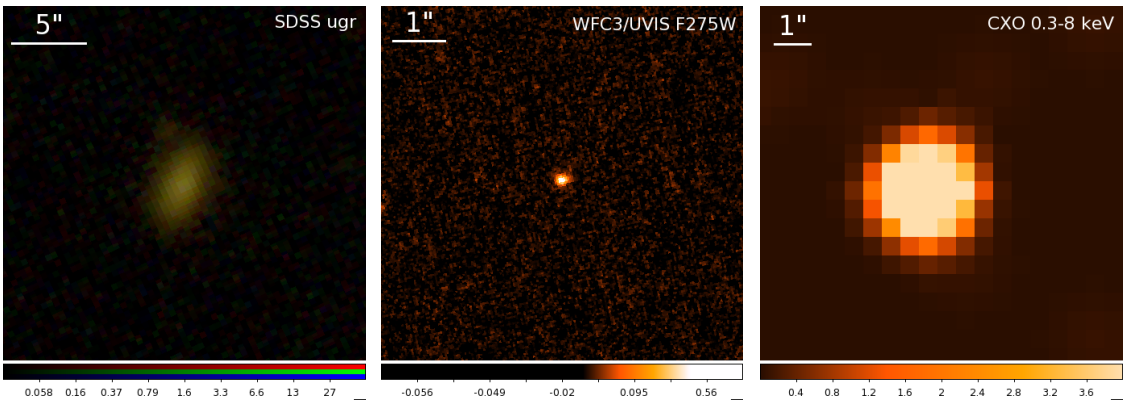

Figure 4.8 Optical, UV, and X-ray imaging of RGG 127. See Figure 4.2 for a more detailed description.

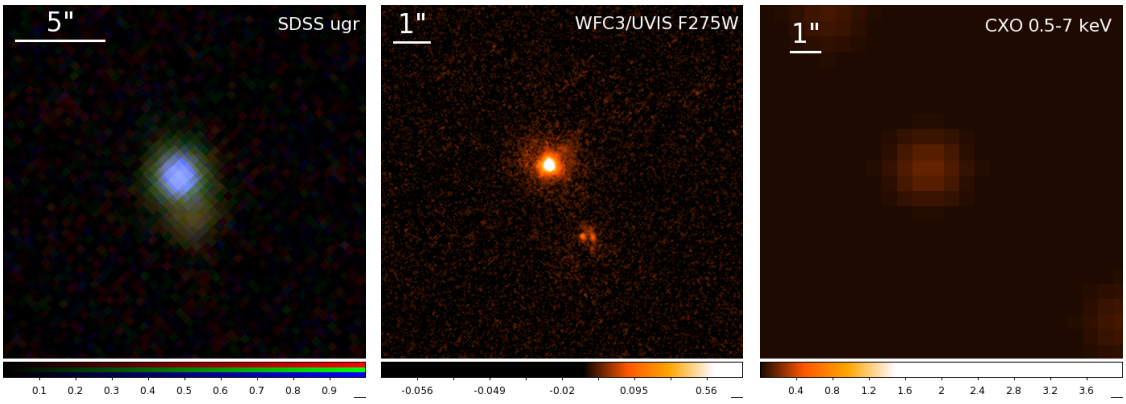

Figure 4.9 Optical, UV, and X-ray imaging of RGG B. See Figure 4.2 for a more detailed description. Note that RGG B is the sole object with narrow line ratios placing it in the star formation region of the BPT diagram.

4.3.1 Chandra X-ray Observatory

Chandra X-ray Observatory observations of our targets were taken with the Advanced CCD Imaging Spectrometer S-array (ACIS-S) between December 2014 and April 2016 (PI: Reines, Cycle 16). See Table 4.1 for a summary of observations. The data were re-processed and analyzed with the Chandra Interactive Analysis of Observations software package (CIAO; version 4.8). After reprocessing and restricting our data to the S3 chip, we generated a preliminary source list using CIAO WAVDETECT, and corrected the Chandraastrometry by cross-matching our observations with sources in the Sloan Digital Sky Survey catalog (excluding our own). In 3 observations (RGG 11, 32, B), there were not a sufficient number of cross-matched sources to apply an astrometry correction. For sources where there were three or more cross-matched sources, astrometric corrections ranged from $\sim 0.2 - 0.6''$. We checked all observations for background flares; none were found. We then applied an energy filter (0.3-8 or 0.5-7 keV) and re-ran WAVDETECT using a threshold significance of 10^{-6} (equivalent to 1 false detection over the S3 chip).

We used SRCFLUX to calculate count rates and errors in three energy bands: soft ($0.5-2$ keV), hard ($2-10$ keV), and broad ($0.5-7$ keV). For targets with a WAVDETECT

source coincident with the optical nucleus (RGG 9, 32, 48, 119, 127), we extracted counts in a circular source region of radius 2″ centered on the WAVDETECT coordinates. In the absence of a WAVDETECT source (RGG 1, 11, B), we extracted counts in a region of the same size centered on the nominal position of the nucleus as given by SDSS coordinates. We used a background annulus with inner and outer radii of 20 and 30″, respectively. All sources were detected in the soft and broad bands.

Counts were converted to unabsorbed fluxes using the Portable, Interactive Multi-Mission Simulator (PIMMS)[2]. We assumed the underlying spectrum to be a power law with $\Gamma = 2.0$, except in the cases of RGG 119 and RGG 127, for which we were able to measure Γ directly from the extracted spectra (see below). Galactic HI column density measurements were obtained with the HEASARC nH tool[3], which uses HI column densities measured by Kalberla et al. (2005). Table 4.2 presents the counts, unabsorbed fluxes, and luminosities for each target in each wave band.

We took the following steps to account for intrinsic absorption. First, assuming $\Gamma = 2.0$, we used PIMMS to determine the expected 0.5-2 keV count rate based on the count rate in the 2-10 keV band, which is largely unaffected by absorption. If the expected 0.5-2 keV count rate was *higher* than the observed rate, we determined what intrinsic n_H would be required to produce the observed rate. We then recalculated 0.5-2 and 0.5-7 keV fluxes accounting for both Galactic extinction and intrinsic absorption. Using this methodology, there is evidence for some intrinsic absorption in RGG 1, 11, and 48. Additionally, spectral fitting for RGG 127 suggests a small amount of intrinsic absorption (see below). Table 4.3 presents the computed intrinsic n_H for these four systems, and updated 0.5-2 keV and 0.5-7 keV fluxes. Extinction corrected fluxes are used throughout the remainder of this paper. We note that intrinsic n_H values range from 4×10^{20} to 9×10^{21} cm^{-2} and the extinction

[2]http://cxc.harvard.edu/toolkit/pimms.jsp
[3]http://heasarc.nasa.gov/cgi-bin/Tools/w3nh/w3nh.pl

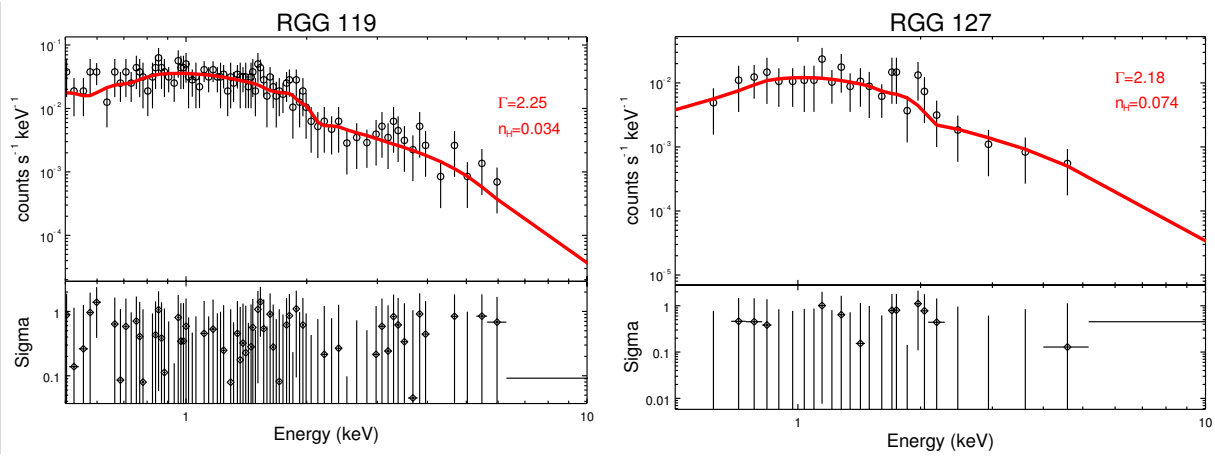

Figure 4.10 *Left*: X-ray spectrum of RGG 119. We fit the spectrum with an absorbed power law model, finding a best fit $\Gamma = 2.25$. *Right*: X-ray spectrum of RGG 127. We fit the spectrum with an absorbed power law model, finding a best fit $\Gamma = 2.18$ and $n_H = 7.4 \times 10^{20}$ cm^{-2} (approximately twice the galactic n_H value).

corrected fluxes are within a factor of ~ 2 of the observed fluxes (and generally within the errors on the observed fluxes).

Two sources (RGG 119 and 127) had enough counts (n $\gtrsim$ 100) to warrant spectral analysis (Figure 4.10). We use the Sherpa fitting package in CIAO to model the extracted spectra using an absorbed power law model. Since it is possible to have both Galactic absorption and absorption intrinsic to the galaxy itself, we fit the spectra two ways: with n_H frozen to the Galactic value, and with n_H constrained to be at least the Galactic value. We find that the spectrum of RGG 119 has a best fit power law index of $\Gamma = 2.25 \pm 0.25$. The models did not prefer an n_H greater than the galactic value, suggesting little-to-no intrinsic absorption. RGG 127, however, has a best fit n_H approximately twice the galactic value, indicating potential intrinsic absorption. For RGG 127, we find a corresponding best fit Γ of $2.18^{+0.55}_{-0.35}$. If we freeze n_H to the galactic value, we obtain $\Gamma = 2.03$.

4.3.2 Hubble Space Telescope

HST WFC3 images were taken with the UVIS channel and F275W filter. Individual exposures were processed and combined using the standard HST AstroDrizzle reduction pipeline. Total exposure times ranged from 747 s to 900 s. We detect UV emission from all eight targets.

We use the PHOT task within the STSDAS package for PyRAF to measure UV fluxes. The UV emission associated with the AGN emerges from the unresolved accretion disk. There may also be spatially resolved UV emission on scales larger than the WFC3 PSF. In order to isolate emission from the AGN, we measure the flux within an aperture with a radius of 3 pixels centered on the brightest pixel, accounting for the HST WFC3/UVIS F275W encircled energy fraction. We try four different background apertures ranging from an annulus immediately surrounding the source (effectively subtracting off any nearby star formation) to a large annulus containing only the sky background. The choice of background aperture does not strongly affect our results, but since we do expect some UV emission from star formation in addition to any from the AGN, we use the innermost annulus background for our measurements of the UV-to-X-ray flux ratio. Table 4.4 presents measured count rates for the background and AGN.

4.3.3 Archival data

Chandra imaging of RGG 21 (NGC 4395) was analyzed in Moran et al. (2005), and RGG 20 and RGG 123 were analyzed in Dong et al. (2012a). We briefly summarize their findings here.

RGG 20. RGG 20 (SDSS J122342.82+581446.4) was found to have a 0.5-8 keV luminosity of $L = 6.7 \times 10^{41}\ \mathrm{erg\ s^{-1}}$. There were a sufficient number of counts to extract a spectrum; the best-fit photon index was $\Gamma = 1.54 \pm 0.10$. The ratio of X-ray to UV

emission ($\alpha_{\rm OX}$; see Section 4.4.2) is $\alpha_{\rm OX}$= -1.30.

RGG 21. RGG 21 (NGC 4395; SDSS J122548.86+333248.7) was found to have a 2-10 keV luminosity of $L = 8.0 \times 10^{39}$ erg s^{-1}. NGC 4395 displays dramatic spectral variability, with measured power law indices ranging from $\Gamma = 1.72$ (Iwasawa et al. 2000) to $\Gamma = 0.61$ (Moran et al. 2005) on timescales of several years.

RGG 123. RGG 123 (SDSS J153425.58+040806.6) has a 0.5-8 keV luminosity of $L = 8.5 \times 10^{41}$ erg s^{-1}. There were not sufficient counts to extract an X-ray spectrum. The photon index as estimated from the hardness ratio is $\Gamma_{\rm HR} = 2.57 \pm 0.27$[4], and $\alpha_{\rm OX}$ was found to be -1.22.

Dong et al. (2012a) reports count rates for RGG 20 and 123 (as well as fluxes and luminosities) in the 0.5-2 keV and 2-8 keV bands. For uniformity, we convert their 2-8 keV count rates to 2-10 keV fluxes using PIMMS. For RGG 20, we use the photon index of $\Gamma = 1.54$ obtained from the fit to the spectrum. For RGG 123, we follow the same procedure as for our new data and use a photon index of $\Gamma = 2.0$.

4.4 Results

4.4.1 Nuclear X-ray Emission

All eleven targets are detected, i.e., we find a 100% X-ray detection rate for nearby ($z < 0.055$) dwarf galaxies with broad and narrow-line AGN signatures (i.e., those falling in the AGN *or* composite region of the BPT diagram). For our 8 new targets, we measure count rates in the $0.5 - 7$ keV band ranging from 1.5×10^{-4} cts/s to 5.2×10^{-2} cts/s. Correspondingly, we estimate $0.5 - 7$ keV luminosities ranging from $\sim 5 \times 10^{39}$ to $\sim 1 \times 10^{42}$ erg s^{-1}. Distances are estimated using redshifts reported in the NASA-Sloan Atlas and Ned Wright's cosmology calculator (Wright 2006).

[4]Dong et al. (2012a) found that the photon index estimated from the hardness ratio is highly correlated with the photon index of the fitted spectrum for $\Gamma > 2$.

If we assume that the measured X-ray luminosities are due to accreting BHs (see Section 4.5.1 for a discussion of the origin of X-ray emission for these sources), we can estimate Eddington fractions, i.e. at what percentage of their Eddington luminosities these BHs are accreting. Eddington luminosities are determined using the BH masses from Reines et al. (2013), with the exceptions of RGG 9 and RGG 119, which have updated BH masses given in Baldassare et al. (2016). BH masses for this sample are estimated using the luminosity and FWHM of the broad Hα emission line Kaspi et al. 2000; Peterson et al. 2004; Greene & Ho 2005b; Bentz et al. 2009, 2013 and a virial factor of $\epsilon = 1$ (see equation 5 in Reines et al. 2013). BH masses range from $7 \times 10^4 - 1 \times 10^6\ M_\odot$ (Reines et al. 2013, Baldassare et al. (2016)). We note that the uncertainty on BH masses calculated from this method is large; ~ 0.4 dex (Shen & Liu 2012).

We caution that bolometric corrections for AGN in this mass regime are largely unconstrained. However, in the absence of a full analysis of the spectral energy distribution of AGN in dwarf galaxies, we use a hard X-ray bolometric correction of $L_{\rm Bol}/L_{2-10{\rm keV}} = 10$ (Marconi et al. 2004). For $L_{\rm bol} = 10\ L_{2-10{\rm keV}}$, we find Eddington fractions ranging from $\sim 0.1 - 50\%$, including the archival observations (see Table 4.5 for Eddington ratios and black hole masses). The median Eddington fraction for this sample of 10 dwarf AGN is 4.3% (mean $\approx 10\%$); this range is comparable to the range of Eddington ratios for broad-line quasars at higher redshifts (see, e.g., Kelly et al. 2010; Shen & Kelly 2012). Note that we have excluded RGG B from this analysis, as we do not consider it a secure AGN; see Section 4.5.1.

4.4.2 UV-to-X-ray flux ratios

We measure $\alpha_{\rm OX}$ in order to quantify the relative power output in the UV and in X-rays (Tananbaum et al. 1979). The quantity $\alpha_{\rm OX}$ is defined as $\alpha_{\rm OX} = -0.383 \log(l_{2500}/l_{2{\rm keV}})$, where l_{2500} is the luminosity density at 2500Å and $l_{2{\rm keV}}$ is the unabsorbed luminosity

density at 2 keV. We measure the 2500Å UV flux density directly from the HST F275W imaging (the peak of the filter output is close to 2600Å, i.e. $\sim 2500\text{Å}$ for a galaxy at z=0.04). We use PIMMS and the appropriate power-law index ($\Gamma = 2.0$, except when measured directly from spectral fitting) to determine the 2keV luminosity.

We find $\alpha_{\rm OX}$ values ranging from -2.13 to -0.95 (Figure 4.11). Values of $\alpha_{\rm OX}$ are reported for each galaxy in Table 4.5. These values are consistent with those found by Dong et al. (2012a) and Plotkin et al. (2016) for low-mass AGN with BH masses of $\sim 10^6 M_\odot$. Though we have a very limited sample size, broadly speaking, the highest $\rm L_{bol}/L_{Edd}$ objects have the least negative $\alpha_{\rm OX}$ values, i.e. are more X-ray luminous relative to their UV emission.

In Figure 4.12, we compare our $\alpha_{\rm OX}$ values to expected values based on the relationship between $\alpha_{\rm OX}$ and l_{2500} found by Just et al. (2007). We find that our targets tend to have $\alpha_{\rm OX}$ *lower* than expected based on the $\alpha_{\rm OX}$-l_{2500} relation (the $\alpha_{\rm OX}$ values range from $\sim 0.1 - 1$ below the expected values). Despite the general trend, RGG 119 and RGG 127, i.e. the two objects with the highest $\rm L_{bol}/L_{Edd}$, have $\alpha_{\rm OX}$ consistent with their "expected" values. The large dispersion in $\alpha_{\rm OX}$ values for BHs with $M_{\rm BH} \lesssim 10^6 M_\odot$, as well as their tendency to be X-ray weak relative to the $\alpha_{\rm OX} - l_{2500}$ relation is also observed by Dong et al. (2012a) and Plotkin et al. (2016). This is further discussed in Section 4.5.2.

We also note that it is difficult to disentangle UV emission from the AGN from emission due to star formation. If a significant fraction of the UV emission is from star formation, then $\alpha_{\rm OX}$ values would appear *lower* (i.e., more negative) than they are.

4.4.3 X-ray hardness ratio

Hardness ratios can yield information about the spectral shape for sources with too few counts to extract a spectrum. We compute hardness ratios for our targets using the Bayesian Estimation of Hardness Ratios code (BEHR; Park et al. 2006). Hardness ratio

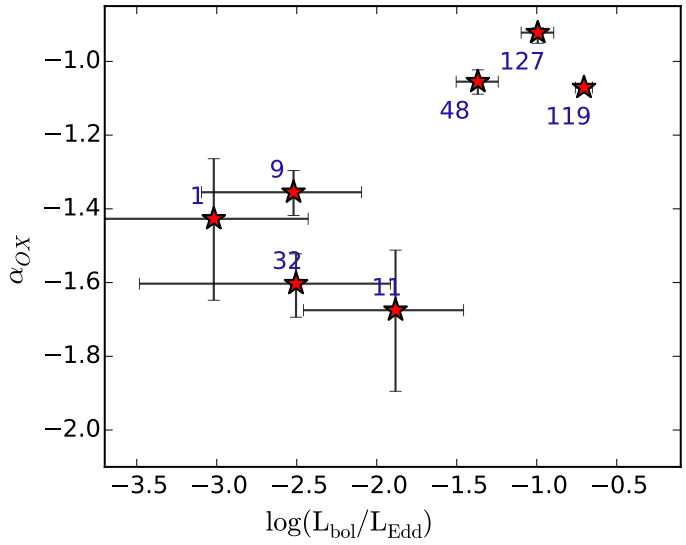

Figure 4.11 Ratio of UV-to-X-ray emission, $\alpha_{\rm OX}$, versus Eddington ratio. $L_{\rm bol}/L_{\rm Edd}$ is calculated using a bolometric correction of 10 (Marconi et al. 2004).

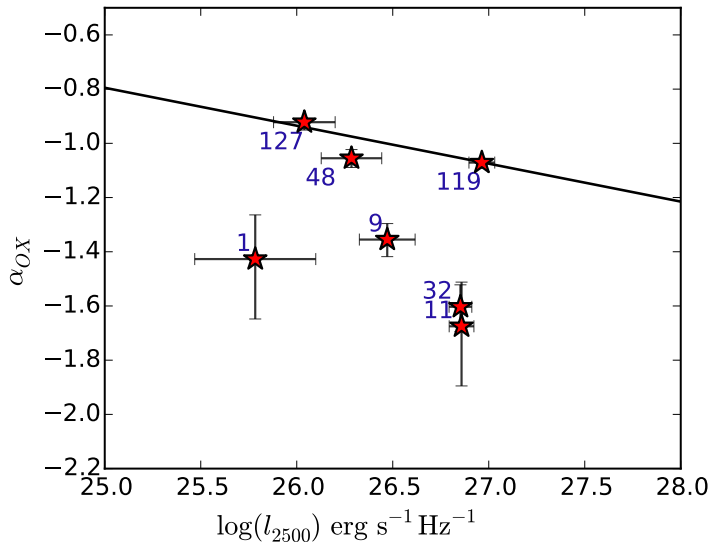

Figure 4.12 Ratio of UV-to-Xray emission ($\alpha_{\rm OX}$) versus luminosity at 2500 Å. The solid black line represents the relationship between l_{2500} and $\alpha_{\rm OX}$ found by Just et al. (2007) using a sample of 372 quasars from $z = 1.5 - 4.5$.

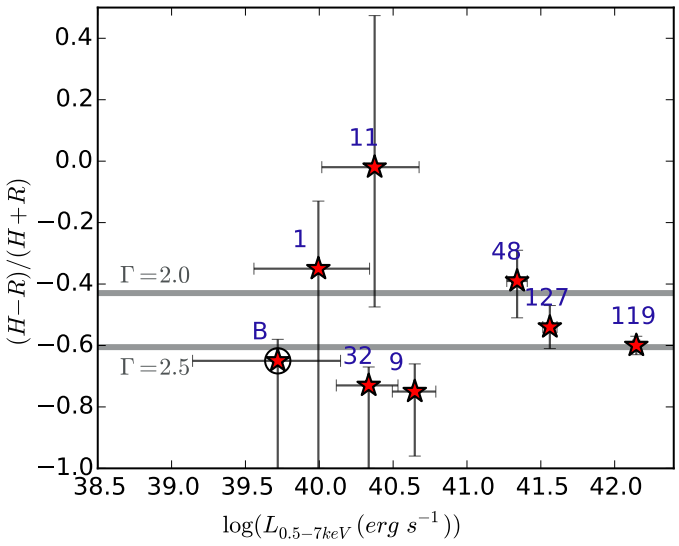

Figure 4.13 Hardness ratio versus 0.5-7 keV luminosity. Hardness ratios were computed using the BEHR code; error bars represent 90% confidence intervals. For reference, we show hardness ratios computed using the WEBPIMMS tool for unabsorbed power laws with $\Gamma = 2.0$ and $\Gamma = 2.5$. The lone BPT star forming object (RGG B) is also marked with an open circle.

is defined as $(\mathrm{H} - \mathrm{S})/(\mathrm{H} + \mathrm{S})$, where H and S are the number of counts in the hard and soft bands, respectively. Here, we use 0.5-2 keV as our soft band and 2-7 keV as the hard band. BEHR treats counts as independent Poisson random variables, and can be used even if the source is undetected in one of the bands (as is the case for RGG B). We find hardness ratios ranging from -0.75 to -0.02, with a median hardness ratio of -0.57 (see Figure 4.13). For reference, we compute expected hard and soft band counts for power law spectra with varying Γ; a hardness ratio of ~ -0.4 is characteristic of an unabsorbed power law spectrum with $\Gamma = 2.0$, while an unabsorbed power law spectrum with $\Gamma = 2.5$ produces a hardness ratio of ~ -0.6.

The hardness ratios for RGG 119 and RGG 127 are consistent with the expected hardness ratios for $\Gamma \approx 2.0 - 2.5$; these are in turn consistent with the Γ which best fit the extracted X-ray spectra (2.25 and 2.18 for RGG 119 and RGG 127, respectively).

4.5 Discussion

4.5.1 Origin of X-ray emission

The Eddington luminosity[5] for a $10^5\ M_\odot$ black hole is $\sim 10^{43}$ erg s^{-1}. Therefore, the X-ray luminosities of Eddington-limited X-ray binaries can be comparable to the luminosities of sub-Eddington AGN in our BH mass range of interest. Here, we carefully consider the origin of the detected X-ray emission in our targets.

The expected X-ray luminosity due to high mass X-ray binaries (HMXBs) scales with the star formation rate of the galaxy (Grimm et al. 2003), while the X-ray luminosity due to low-mass X-ray binaries (LMXBs) scales with stellar mass (Gilfanov 2004). As shown in Gilfanov (2004), for a galaxy with $M_* \sim 10^9 M_\odot$, we expect LMXBs to contribute $L_X < 10^{38}$erg s^{-1}; our X-ray sources are all more luminous by at least a factor of 10, making LMXBs an unlikely source of the nuclear X-ray emission. Additionally, while the fairly soft best-fit spectral indices for RGG 119 and 127 are typical of quasars, they are also typical of high mass X-ray binaries (HMXBs), particularly in the steep power law and high/soft states (Remillard & McClintock 2006). Thus, we consider HMXBs our most likely alternative source of X-ray emission. We estimate the expected luminosity contributed from HMXBs below.

Using the extinction-corrected luminosity of the narrow Hα emission from Reines et al. (2013) and the relation in Kennicutt & Evans (2012), we compute upper limits on the SFR for each galaxy by assuming that all the narrow Hα emission within the SDSS fiber is due to star formation. Note that for objects which fall in the composite or AGN region of the BPT diagram, we can be confident there is some contribution to the Hα emission from the AGN. Also note that the 3″ SDSS fiber is larger than the 2″ *Chandra* PSF, so we are calculating the expected contribution from HMXBs over a slightly larger area than necessary.

[5] $L_{\rm Edd} = ({\rm M_{BH}/M_\odot}) \times 1.25 \times 10^{38}\ {\rm erg\ s^{-1}}$

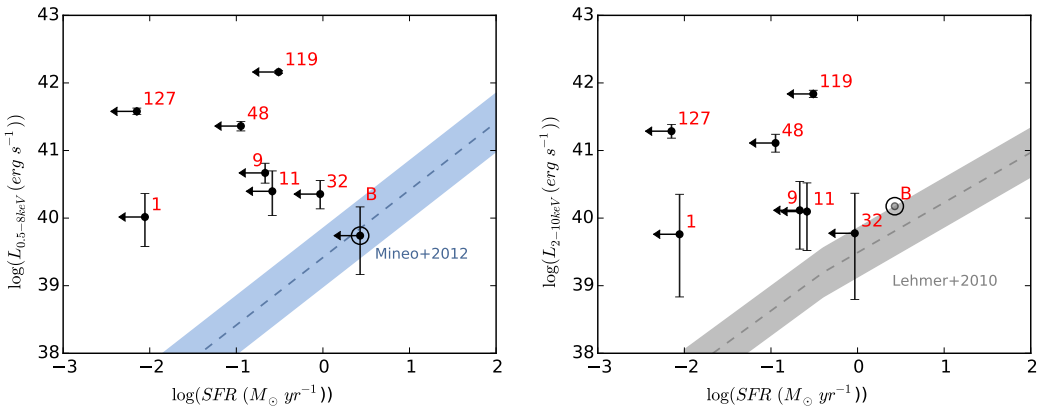

Figure 4.14 X-ray luminosity versus SFR for our eight targets. SFRs are conservative upper-limits determined based on the luminosity of narrow Hα (see text). The left panel uses 0.5-8 keV luminosities and the relation defined in Mineo et al. (2012). The right panel uses 2-10 keV luminosities and the relation defined by Lehmer et al. (2010). On the right panel, RGG B, the BPT star forming object, has only an upper limit on the 2-10 keV luminosity, and is shown as a faded point. In both panels, RGG B is also marked with an additional open circle.

We use relations from Lehmer et al. (2010) and Mineo et al. (2012) to compute, respectively, the expected 2-10 keV and 0.5-8 keV luminosities from HMXBs. As shown in the left panel of Figure 4.14, the 0.5-8 keV luminosities of all targets with broad *and* narrow optical emission line AGN signatures are higher (by $1.5 - 18\sigma$) than would be expected from star formation alone. RGG B, the sole target with narrow line ratios consistent with photoionization from HII regions, has a 0.5-8 keV X-ray luminosity consistent with that expected from star formation.

Using 2-10 keV luminosities and the relation given by Lehmer et al. (2010) we find that most targets have X-ray luminosities greater than would be expected from star formation ($1 - 9\sigma$ higher), with the exception of RGG 32, which has a hard X-ray luminosity consistent with the estimated contribution from HMXBs, and RGG B, which is not detected in the 2-10 keV band (see right panel of Figure 4.14). We stress again that the SFRs used are conservative upper limits, and that the actual star formation rates are lower for objects falling in the composite or AGN region of the BPT diagram.

With the exception of RGG B (and RGG 32 in the hard band), the X-ray luminosities of

our targets are higher than would be expected from star formation. For our seven targets with with broad *and* narrow emission line signatures of an AGN, we consider an AGN the most likely source of the nuclear X-ray emission. RGG B, which falls in the star forming region of the BPT diagram, has the lowest X-ray luminosity, and moreover, a 0.5-8 keV X-ray luminosity consistent with that which would be expected from star formation. Optical spectroscopy of RGG B was also analyzed in Baldassare et al. (2016), which carried out multi-epoch spectroscopy of star-forming dwarf galaxies with broad Hα. They found that the broad Hα faded in star forming targets, indicating the broad emission was likely produced by a transient stellar process for such objects. RGG B was classified as ambiguous with respect to the presence of broad Hα in spectra taken several years following the SDSS spectrum. However, even if the broad emission in the SDSS spectrum of RGG B is produced by an AGN, we cannot say with certainty that the observed nuclear X-ray emission is not associated with a HMXB.

We emphasize that more than a third of our sample falls in the composite region of the BPT diagram. Though BPT star forming objects with broad Hα are not necessarily AGN, this work provides strong evidence to suggest that the composite objects do indeed host AGN.

4.5.2 Comparison to more massive AGN

Below, we compare the properties of the AGN considered in this paper to the properties of more massive quasars, as well as to the properties of the Desroches et al. (2009) and Dong et al. (2012a) samples of low-mass AGN (i.e. $M_{BH} \approx 10^5 - 10^6 M_{\odot}$).

Just et al. (2007) explore the ultraviolet and X-ray properties of luminous quasars in SDSS from $z = 1.5-4.5$. They find a mean photon index of $\Gamma = 1.92^{+0.09}_{-0.08}$, with measured values ranging from $\Gamma = 1.3 - 2.3$. Our measured values of Γ (2.25 and 2.18 for RGG 119 and 127, respectively) are consistent with these. Moreover, it is predicted that objects

accreting at higher Eddington fractions will have lower (i.e. more negative) photon indices (Brightman et al. 2013). Just et al. (2007) also measure $\alpha_{\rm OX}$ values ranging from -2.2 to -1.5, and find a tight relation between l_{2500} and $\alpha_{\rm OX}$. While our measured $\alpha_{\rm OX}$ also fall in this range, based on the $l_{2500} - \alpha_{\rm OX}$ relation, we expect values closer to -1.0. We note that our two brightest, highest $\rm L_{bol}/L_{Edd}$ targets (RGG 119 and 127) have $\alpha_{\rm OX} \approx -1$, consistent with the Just et al. (2007) relation.

As discussed at length in Dong et al. (2012a), there are several factors which can influence $\alpha_{\rm OX}$. In the disk, UV photons are inverse-Compton scattered into an X-ray corona. The temperature of the disk therefore influences how much disk energy is reprocessed in this manner. If the disk extends to the innermost stable circular orbit, the peak disk temperature is dependent on BH mass such that smaller BHs have hotter disks. The disk temperature can also be dependent on the accretion rate. Additionally, the structure of the disk, i.e., whether the disk is thin or slim, can influence $\alpha_{\rm OX}$. Finally, absorption can lead to suppressed UV emission and a harder overall spectrum.

Dong et al. (2012a) combine their sample of low-mass AGN with more massive AGN in order to explore trends between $\alpha_{\rm OX}$, $L_{\rm bol}/L_{\rm Edd}$, and $M_{\rm BH}$. They find $\alpha_{\rm OX}$ is not correlated at all with $L_{\rm bol}/L_{\rm Edd}$. However, they find a potential trend between $\alpha_{\rm OX}$ and $M_{\rm BH}$ such that the mean $\alpha_{\rm OX}$ decreases (becomes more negative) with increasing $M_{\rm BH}$. This is expected to be due to the blackbody temperature of the accretion disk increasing with decreasing BH mass (for a given mass accretion rate; see Done et al. 2012). The accretion disk temperature is also expected to rise with increasing mass accretion rate. The mean $\alpha_{\rm OX}$ for our targets with $M_{\rm BH} \approx 10^{5-6} M_{\odot}$ does not follow the trend noted by Dong et al. (2012a), i.e., the mean $\alpha_{\rm OX}$ is more negative than for the objects with $M_{\rm BH} \approx 10^{6-7}\ M_{\odot}$ (though we reiterate that our sample size is small). Additionally, there appears to be a potential trend between $\alpha_{\rm OX}$ and $L_{\rm bol}/L_{\rm Edd}$ for our sample; the objects with the highest Eddington

fractions also have the least negative $\alpha_{\rm OX}$ values (see Figure 4.11). A larger sample size would aid in determining whether the disk properties of AGN in dwarf galaxies are indeed distinct from those of more massive objects.

Desroches et al. (2009) find that their five detected objects (out of eight total) show evidence for *slim disk* accretion (Abramowicz et al. 1988). This accretion mode is expected to be relevant at high Eddington fractions ($L_{\rm Bol}/L_{\rm Edd} \gtrsim 0.3$). In this regime, the disk puffs up at small radii, and accretion becomes radiatively inefficient due to photon-trapping. The result is that X-ray emission appears enhanced relative to optical/UV emission. Three AGN considered here show evidence for potential slim disk accretion. Using a bolometric correction of 10, we find that RGG 119, 123, and 127 are accreting at high fractions of their Eddington luminosities (20%, 54%, and 10%, respectively). Moreover, they all have relatively flat $\alpha_{\rm OX}$ values close to -1.0; Desroches et al. (2009) find similar values. However, the remaining targets are estimated to be accreting at lower Eddington fractions and have $\alpha_{\rm OX}$ values closer to ~ -1.5.

Dong et al. (2012a) explores whether their sample follow the relation between [OIII]$\lambda 5007$ luminosity and $2-10$ keV luminosity. There is a very tight correlation between these quantities for unobscured AGN (Panessa et al. 2006), since [OIII] is thought to be a good indicator of the power output of the central engine. While the Dong et al. (2012a) objects do cluster around this relation, they find that their sample tends to scatter below it, i.e., they are relatively X-ray weak compared to the [OIII] luminosity. This behavior is similar to the Compton-thick sample from Panessa et al. (2006), making local absorption a possible explanation for this trend. We observe this behavior for our target AGN in dwarf galaxies (Figure 4.15). However, while we do find evidence for some intrinsic absorption in our sample, the HI column densities we find are in the range of $10^{21}-10^{22}$ cm^{-2}, much lower than those for Compton thick sources ($> 10^{24}$ cm^{-2}).

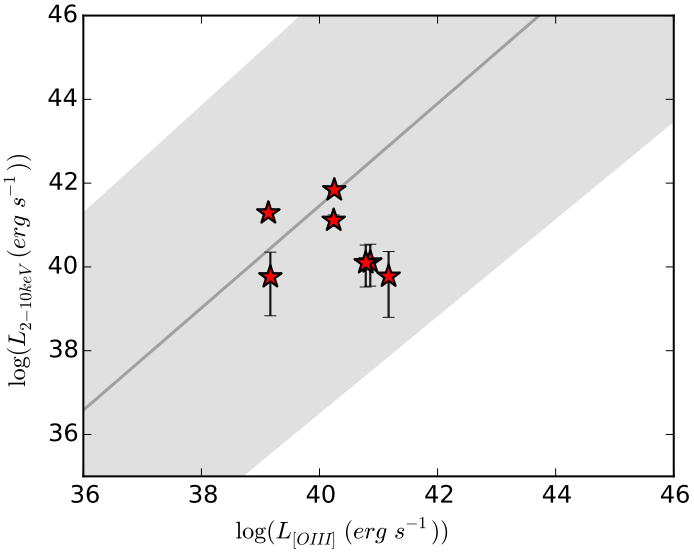

Figure 4.15 X-ray luminosity in the 2-10 keV band versus luminosity of the [OIII]λ5007 emission line. The gray line illustrates the relation between $L_{2-10\mathrm{keV}}$ and $L_{[\mathrm{OIII}]}$ as defined by Panessa et al. (2006). Our targets are shown as red stars. RGG B is not detected in the 2-10 keV band and is not included here.

Finally, Panessa et al. (2006) also finds a correlation between the 2-10 keV luminosity and the Hα luminosity. We show where our sample lies relative to this correlation in Figure 4.16. Our targets sit close to the relation, though 4/7 seem to scatter to slightly lower L_X at fixed $L_{H\alpha}$ relative to more luminous systems. Panessa et al. (2006) suggests such behavior could be due to intrinsic X-ray absorption (in Compton-thick systems) , or contributions to Hα from star formation. Additionally, there could be differences in the spectral energy distributions of AGN in dwarf galaxies, as compared to AGN in more massive systems.

4.6 Conclusions

We analyze *Chandra X-ray Observatory* of 11 broad-line AGN candidates in dwarf galaxies identified in Reines et al. (2013). These include all ten objects with broad and narrow emission line AGN signatures (6 BPT AGN, 4 BPT composite), plus one low-metallicity dwarf galaxy with broad Hα but narrow-emission lines dominated by star

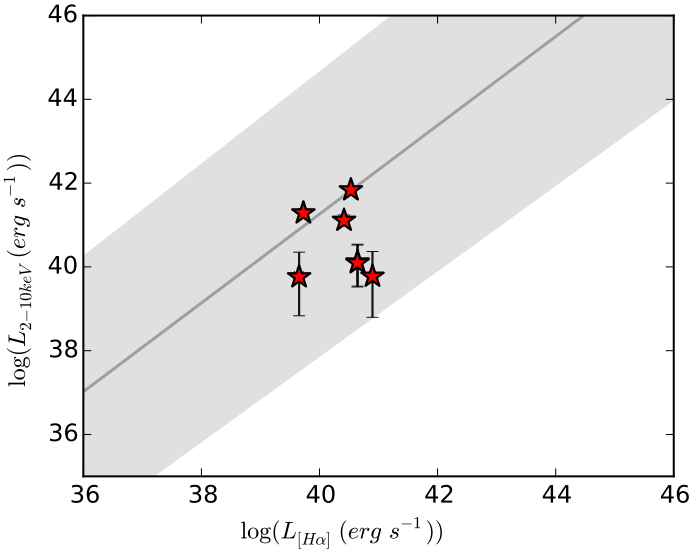

Figure 4.16 X-ray luminosity in the 2-10 keV band versus luminosity of the Hα λ6563 emission line (broad + narrow components; fluxes taken from Reines et al. 2013). The gray line illustrates the relation between $L_{2-10\mathrm{keV}}$ and $L_{\mathrm{H}\alpha}$ as defined by Panessa et al. (2006). Our targets are shown as red stars. RGG B is not detected in the 2-10 keV band and is not included here. Note that there are seven objects plotted here; two objects occupy the same point on this plot.

formation. Three out of eleven objects had *Chandra* observations analyzed in the literature. We analyze new *Chandra* observations of the remaining eight, supplemented by joint HST/WFC3 F275W imaging.

Nuclear X-ray emission is detected in all galaxies, i.e. we find a 100% detection rate. We also find that:

- The detected X-ray nuclei are bright, with $L_{0.5-7\mathrm{keV}} \approx 5 \times 10^{39} - 1 \times 10^{42}$ erg s^{-1}. Galaxies in our sample have BH masses in the range of $\sim 10^{5-6} M_{\odot}$; we infer Eddington fractions ranging from $\sim 0.1 - 50\%$, i.e., consistent with the range of Eddington fractions found for massive broad-line quasars.
- The observed X-ray emission in broad-line objects falling in either the AGN or composite region of the BPT diagram is brighter than would be expected from HMXBs. We conclude an AGN is the most likely source of the detected X-ray emission.
- We emphasize that the observations presented here provide strong evidence that the

BPT composite objects (i.e., those thought to have contributions to the narrow-line flux from both star formation and an AGN) do indeed host actively accreting BHs.

- Our targets tend to have $\alpha_{\rm OX}$ values lower than expected based on relationships defined by classical quasars. If the measured UV emission is not significantly enhanced by nuclear star formation, AGN in dwarf galaxies seem to be X-ray weak relative to their UV emission.

Table 4.1. New *Chandra* observations of broad-line AGN candidates

RGG ID	NSAID	RA	Dec	BPT Class	Redshift	Obs. Date	Obs. ID	Exp. Time (ks)
1	62996	02:46:56.39	-00:33:04.8	AGN	0.0459	2015-07-12	17032	17.4
9	10779	09:06:13.75	+56:10:15.5	AGN	0.0466	2014-12-26	17033	15.83
11	125318	09:54:18.14	+47:17:25.1	AGN	0.0327	2016-04-06	17034	10.26
32	15235	14:40:12.70	+02:47:43.5	AGN	0.0299	2015-04-01	17035	6.97
48	47066	08:51:25.81	+39:35:41.7	Composite	0.041	2015-12-07	17036	12.89
119	79874	15:26:37.36	+06:59:41.6	Composite	0.0384	2015-02-10	17037	10.9
127	99052	16:05:31.84	+17:48:26.1	Composite	0.0317	2015-02-22	17038	7.75
B	15952	08:40:29.91	+47:07:10.4	Star-forming	0.0421	2015-01-05	17039	12.89

Note. — Columns 1 and 2 give the IDs assigned by Reines et al. (2013) and the NASA-Sloan Atlas, respectively. Column 5 gives the BPT classification determined using SDSS spectroscopy. Column 7 gives the date of the Chandraobservation, column 8 gives the observation ID, and column 9 gives the Chandra exposure time.

Table 4.2. X-ray Properties

RGG ID	Counts			Flux (10^{-15}erg s^{-1} cm^{-2})			Luminosity (log(erg s^{-1}))		
	0.5-2 keV	0.5-7 keV	2-10 keV	0.5-2 keV	0.5-7 keV	2-10 keV	0.5-2 keV	0.5-7 keV	2-10 keV
1	2 (0.5, 5.3)	3 (1.1, 6.7)	1 (0.1, 3.9)	0.66 (0.18, 1.76)	1.42 (0.52, 3.16)	1.15 (0.20, 4.48)	39.52 (38.94, 39.95)	39.85 (39.41, 40.19)	39.76 (39.00, 40.35)
9	15 (10.3, 21.3)	17 (12.0, 23.6)	2 (0.5, 5.3)	5.23 (3.59, 7.42)	8.57 (6.04, 11.90)	2.52 (0.67, 6.71)	40.43 (40.27, 40.58)	40.65 (40.50, 40.79)	40.12 (39.54, 40.54)
11	2 (0.5, 5.3)	4 (1.8, 8.0)	2 (0.5, 5.3)	1.37 (0.36, 3.64)	3.97 (1.74, 7.92)	5.01 (1.33, 13.34)	39.53 (38.96, 39.96)	39.99 (39.63, 40.29)	40.10 (39.52, 40.53)
32	8 (4.7, 13.0)	9 (5.4, 14.2)	1 (0.1, 3.9)	6.42 (3.74, 10.43)	10.41 (6.28, 16.43)	2.87 (0.30, 11.15)	40.12 (39.88, 40.33)	40.33 (40.11, 40.53)	39.77 (38.79, 40.36)
48	48 (39.4, 58.2)	69 (58.6, 80.9)	21 (15.4, 28.2)	20.60 (16.90, 24.97)	42.81 (36.35, 50.19)	32.54 (23.83, 43.67)	40.91 (40.82, 40.99)	41.23 (41.16, 41.20)	41.11 (40.98, 41.24)
119	457 (429.8, 485.6)	572 (541.6, 603.9)	117 (103.4, 132.1)	244.7 (230.2, 260.0)	404.10 (382.6, 426.6)	198.1 (175.0, 223.7)	41.93 (41.90, 41.96)	42.15 (42.13, 42.17)	41.84 (41.79, 41.89)
127	111 (97.7, 125.8)	144 (128.9, 160.6)	34 (26.8, 42.8)	82.82 (72.92, 93.84)	144.6 (129.3, 161.3)	82.49 (64.96, 103.8)	41.29 (41.23, 41.34)	41.53 (41.48, 41.58)	41.29 (41.19, 41.39)
B	2 (0.5, 5.3)	2 (0.5, 5.3)	0 (0, 2.3)	0.87 (0.23, 2.30)	1.25 (0.33, 3.32)	0 (0, 4.1)	39.56 (38.98, 39.98)	39.72 (39.14, 40.15)	< 40.18

Note. — Columns 2-4 give the total counts in the 0.5-2, 0.5-7, and 2-10 keV ranges with lower and upper limits in parentheses, as computed by SRCFLUX. Errors on the counts were estimated using the 90% confidence limits given in Gehrels (1986). Columns 6-8 give the corresponding fluxes (corrected for galactic extinction only), and columns 10-12 present corresponding luminosities.

Table 4.3. Extinction Corrected X-ray Fluxes

RGG ID	Galactic N_H (cm^{-2})	Intrinsic N_H (cm^{-2})	Flux ($10^{-15}\mathrm{erg\ s^{-1}\ cm^{-2}}$) 0.5-2 keV	0.5-7 keV
1	4.25×10^{20}	2.5×10^{21}	1.03 (0.27, 2.74)	1.97 (0.72, 4.38)
11	1.6×10^{20}	9.2×10^{21}	4.96 (1.32, 13.2)	9.51 (4.16, 19.0)
48	2.43×10^{20}	1.70×10^{21}	28.8 (23.6, 34.9)	55.1 (46.8, 64.6)
127	3.30×10^{20}	4.1×10^{20}	95.3 (80.2, 103)	156 (140, 174)

Note. — Column 2 gives the galactic HI column density. Column 3 gives the intrinsic column density ("redshifted N_H" in PIMMS), computed as described in Section 4.3.1. Columns 4 and 5 give the corrected 0.5-2 and 0.5-7 keV fluxes, with upper and lower limits in parentheses.

Table 4.4. UV properties

RGG ID	Exp Time	Count rate (counts/s) Total	Background	AGN	f_{2500} ($\mathrm{erg\ s^{-1}\ cm^{-2}\ Hz^{-1}}$)	l_{2500} ($\mathrm{erg\ s^{-1}\ Hz^{-1}}$)
1	747	1.32	0.37	0.95	8.18×10^{-30}	4.10×10^{25}
9	900	6.31	3.19	3.12	2.69×10^{-29}	1.39×10^{26}
11	882	32.86	12.59	20.27	1.75×10^{-28}	4.35×10^{26}
32	747	37.40	20.33	17.07	1.47×10^{-28}	3.06×10^{26}
48	801	5.50	2.66	2.84	2.44×10^{-29}	9.71×10^{25}
119	747	29.79	7.63	22.17	1.91×10^{-28}	6.62×10^{26}
127	756	5.07	1.38	3.69	3.17×10^{-29}	7.44×10^{25}
B	789	90.14	35.20	54.94	4.73×10^{-28}	1.99×10^{27}

Note. — Column 2 gives the *HST* exposure time. Columns 3-5 give *HST* count rates. The total count rate refers to the total count rate in an aperture with radius of $3''$ centered on the UV source. The background count rate refers to the count rate in the annulus immediately surrounding the inner aperture, and is intended to account for any extended star formation in the galaxy. The AGN count rate is the total count rate minus the background count rate. Columns 6 and 7 give the flux and luminosity densities at 2500Å, respectively.

Table 4.5. Summary of Galaxy and AGN properties

RGG ID	$\log(M_*/M_\odot)$	$\log(L_{H\alpha})$ $(\log(\mathrm{erg\,s^{-1}}))$	FWHM$_{H\alpha}$ $(\mathrm{km\,s^{-1}})$	A_V (mag)	N_H $10^{20}\,\mathrm{cm^{-2}}$	$\log(L_{\mathrm{X,S}})$ $(\log(\mathrm{erg\,s^{-1}}))$	$\log(L_{\mathrm{X,H}})$ $(\log(\mathrm{erg\,s^{-1}}))$	$\log(M_{BH}/M_\odot)$	$L_{\mathrm{Bol}}/L_{\mathrm{Edd}}$	α_{OX}
1	9.41	39.38	1577	0.103	4.25	39.71	39.85	5.7	0.001	$-1.43^{+.16}_{-0.22}$
9	9.36	40.15	703	0.066	2.30	40.43	40.65	5.6[a]	0.003	$-1.36^{+.06}_{-.06}$
11	9.12	39.41	636	0.026	1.60	40.09	39.99	4.9	0.013	$-1.68^{+.16}_{-.22}$
20	9.47	40.13	1526	0.037	1.23	41.45[b]	41.72[b]	6.1	0.070	-1.3[b]
21	9.10	38.15	1288	0.046	1.35	–	–	5.0[c]	0.007	–
32	9.46	39.73	747	0.101	2.84	40.12	40.33	5.2	0.003	$-1.60^{+.08}_{-.09}$
48	9.41	39.67	894	0.085	2.43	41.06	41.23	5.4	0.043	-1.06 ± 0.03
119	9.33	40.16	1043	0.129	3.41	41.93	42.15	5.5[a]	0.197	-1.08 ± 0.01
123	9.12	39.82	634	0.122	4.24	41.77[b]	41.41[b]	5.1	0.543	-1.22[b]
127	9.24	39.45	792	0.135	3.30	41.35	41.53	5.2	0.102	$-0.92^{+.01}_{-.03}$
B	8.11	40.67	1245	0.070	2.80	39.56	39.72	6.1	–	$-2.13^{+.16}_{-.22}$

[a] Black hole mass from Baldassare et al. (2016), calculated from the average of several single-epoch spectroscopic black hole mass measurements.
[b] Value taken from Dong et al. (2012a).
[c] RGG 21 (NGC 4395) has several BH mass estimates reported in the literature. For consistency, we use the value quoted in Reines et al. (2013) based on the broad Hα emission, but note that the most recent estimate comes from den Brok et al. (2015), which finds a mass of $4^{+8}_{-3} \times 10^5\,M_\odot$ based on gas dynamical modeling.

Note. — Values in (2), (3), and (4) from Reines et al. (2013). (5) A_V values from NASA/IPAC Infrared Science Archive using measurements from Schlafly & Finkbeiner (2011) (6) from HEASARC nH tool (see Section 4.3.1). Soft X-ray luminosities are in the 0.5-2 keV energy range. Hard X-ray luminosities for objects analyzed in this paper are in the 2-7 keV band, while those reported from Dong et al. (2012) are in the 2-8 keV band.

CHAPTER V

Summary and future directions

5.1 Summary

This work described in this thesis represents a first effort to characterize the population of active BHs in the centers of dwarf galaxies. Until recently, there were only a handful of dwarf galaxies known to contain AGNs. Reines et al. (2013) identified 151 dwarf galaxies with broad and/or narrow-line optical spectroscopic signatures of AGN activity. In this thesis, we describe follow-up studies of well-defined sub-samples of dwarf galaxies identified by Reines et al. (2013) as having AGN signatures.

We analyze multi-epoch spectroscopy of dwarf galaxies as having broad and/or narrow emission line signatures of AGN activity. For galaxies with broad emission, our goal was to determine whether the broad lines were generated by AGN or transient stellar processes. While broad emission lines can be characteristic of dense gas orbiting around a BH, the broad line widths observed in dwarf galaxies are also characteristic of stellar processes like Type II supernovae. Multi-epoch spectroscopy helps distinguish between these scenarios as broad emission from a transient stellar process fades over several years while emission from an AGN typically does not. We find that for dwarf galaxies with recent star formation, broad emission is more likely due to transient stellar processes such as supernovae. Thus, broad emission lines alone should not be used to identify AGNs in dwarf galax-

ies. However, for dwarf galaxies with narrow-line AGN signatures, broad Hα emission is persistent and consistent on baselines of 5-10 years, indicating that for these objects, it originates from gas orbiting around the BH. This work was published in Baldassare et al. (2016).

We present a detailed multi-wavelength analysis of the dwarf galaxy RGG 118, which was part of the sub-sample mentioned above. Follow-up spectroscopy clearly revealed broad emission lines, which we used to estimate a BH mass of $\sim 50,000$ solar masses. At the time of this dissertation, this is the smallest BH yet reported in a galaxy nucleus. We also present Chandra X-ray observations of RGG 118, which show a hard X-ray point source coincident with the nucleus – further confirmation that RGG 118 hosts an accreting BH. These results were published in Baldassare et al. (2015). We also present an analysis of new Hubble Space Telescope observations of RGG 118, which are used to study the structure of the host galaxy (Baldassare et al. 2017, *submitted*).

Finally, we characterize the X-ray and ultraviolet properties of dwarf galaxies with broad and narrow-line AGN signatures. We find a 100% X-ray detection rate for these systems, with X-ray luminosities brighter than would be expected from X-ray binaries alone. This provides strong confirmation that these systems are *bona fide* AGNs. Moreover, the computed Eddington ratios for these systems are high (0.1-50%), similar to Eddington ratios found for more massive AGN at high redshift. These results were presented in Baldassare et al. (2017).

Collectively, these results begin to answer several of the open questions relating to BHs in dwarf galaxies, particularly relating to BH masses, scaling relations, and the spectral energy distribution of AGNs in dwarf galaxies. We show that broad emission lines from dwarf galaxies with narrow emission line AGN signatures are secure, i.e., also from the AGN, and can be used to estimate BH masses. BH masses in dwarf galaxies tend to be

between 10^5 and 10^6 $M_\odot$, but can be as low as $\sim 50,000 M_\odot$. The mass of the BH in RGG 118 indicates that BH seed formation mechanisms must produce BHs smaller than this at least some of the time.

We have begun to explore where dwarf galaxies sit with respect to BH mass-galaxy scaling relations defined by more massive systems. We find that RGG 118 and RGG 119 sit near the extrapolation of the $M_{\rm BH} - \sigma_*$ relation to low BH/galaxy masses. On the other hand, similar to other galaxies without classical bulges, RGG 118 sits below the extrapolation of the $M_{\rm BH} - M_{\rm bulge}$ and $M_{\rm BH} - L_{\rm bulge}$ relations. This result is consistent with the existence of different modes of BH growth, i.e. secular versus merger-driven.

Finally, our X-ray/UV analysis makes progress towards determining the spectral energy distributions of AGN in dwarf galaxies, which is necessary for determining the bolometric correction for such objects.

5.2 Future directions

As the number of known dwarf galaxies with AGN signatures increases, we can continue to move towards demographic studies to understand whether/how dwarf galaxies with AGNs differ from those without AGNs. There are many factors that have the potential to influence the presence of BHs in dwarf galaxies and/or their accretion rates. These include factors such as morphology and large scale environment. It will also be interesting to see whether AGN in dwarf galaxies have an effect on the host galaxy, e.g., shutting off star formation.

There are several upcoming missions that are expected to make significant contributions towards unanswered questions in this field. The Large Synoptic Survey Telescope (LSST) is an 8.4m telescope currently under construction in Chile, with operations scheduled to begin in 2023. LSST will conduct a 10-year survey of the sky, imaging the entire sky

in six bands every three nights. LSST is optimized for studying transient astronomical events (e.g., supernovae). Particularly relevant to this field will be discoveries of tidal disruption events (TDEs). TDEs occur when stars wander too close to a BH and are pulled apart by tidal forces, creating a flare. These events allow us to study distant BHs in formally non-active galaxies. LSST is expected to discover upwards of 100 TDEs per year. One interesting TDE scenario is the disruption of a white dwarf by an intermediate-mass BH. White dwarfs are dense enough that for BHs with $M_{\rm BH} \gtrsim 10^5 M_\odot$, the tidal disruption radius is smaller than the Schwarzschild radius, so no TDE would be observed. However, for BHs with masses $M_{\rm BH} \lesssim 10^5 M_\odot$, the tidal disruption radius is outside the Schwarzschild radius, and a TDE would be observable. Thus, detecting the tidal disruption of a white dwarf would also mean discovering an intermediate-mass BH. Finally, TDE rates can be used to probe the BH mass function. Stone & Metzger (2016) show that the rate of TDEs per unit volume is sensitive to the low-mass end of the BH occupation fraction.

The James Webb Space Telescope (JWST) is a 6.5m space telescope scheduled to launch in October 2018. JWST will observe in the near-IR and mid-IR, making it optimal for studying very distant stars and galaxies in the early universe. JWST may also be able to determine the dominant BH seed formation mechanism. Natarajan et al. (2017) predict that if BH seeds are massive ($10^{4-5} M_\odot$), there should exist a class of transient, high-redshift objects called "obese black hole galaxies", which should be detectable with JWST. On the other hand, seeds formed via the deaths of Population III stars should remain undetectable.

Bibliography

Abel, T., Bryan, G. L., & Norman, M. L. 2002, Science, 295, 93

Abramowicz, M. A., Czerny, B., Lasota, J. P., & Szuszkiewicz, E. 1988, Astrophysical Journal, 332, 646

Agarwal, B., Smith, B., Glover, S., Natarajan, P., & Khochfar, S. 2016, Monthly Notices of the Royal Astronomical Society, 459, 4209

Ahn, C. P., Seth, A. C., den Brok, M., et al. 2017, Astrophysical Journal, 839, 72

Aihara, H., Allende Prieto, C., An, D., et al. 2011, Astrophysical Journal Supplements, 193, 29

Alexandroff, R., Overzier, R. A., Paragi, Z., et al. 2012, Monthly Notices of the Royal Astronomical Society, 423, 1325

Alvarez, M. A., Wise, J. H., & Abel, T. 2009, Astrophysical Journal Letters, 701, L133

Baldassare, V. F., Reines, A. E., Gallo, E., & Greene, J. E. 2015, Astrophysical Journal Letters, 809, L14

—. 2017, Astrophysical Journal, 836, 20

Baldassare, V. F., Reines, A. E., Gallo, E., et al. 2016, Astrophysical Journal, 829, 57

Baldwin, J. A., Phillips, M. M., & Terlevich, R. 1981, Publications of the Astronomical Society of the Pacific, 93, 5

Barth, A. J., Greene, J. E., & Ho, L. C. 2008, Astronomical Journal, 136, 1179

Barth, A. J., Ho, L. C., Rutledge, R. E., & Sargent, W. L. W. 2004, Astrophysical Journal, 607, 90

Begelman, M. C. 2010, Monthly Notices of the Royal Astronomical Society, 402, 673

Begelman, M. C., Volonteri, M., & Rees, M. J. 2006, Monthly Notices of the Royal Astronomical Society, 370, 289

Bell, E. F., McIntosh, D. H., Katz, N., & Weinberg, M. D. 2003, Astrophysical Journal Supplements, 149, 289

Bellovary, J., Volonteri, M., Governato, F., et al. 2011, Astrophysical Journal, 742, 13

Bentz, M. C., Walsh, J. L., Barth, A. J., et al. 2009, Astrophysical Journal, 705, 199

—. 2010, Astrophysical Journal, 716, 993

Bentz, M. C., Denney, K. D., Grier, C. J., et al. 2013, Astrophysical Journal, 767, 149

Bentz, M. C., Batiste, M., Seals, J., et al. 2016, Astrophysical Journal, 831, 2

Bilir, S., Ak, S., Karaali, S., et al. 2008, Monthly Notices of the Royal Astronomical Society, 384, 1178

Blandford, R. D., & McKee, C. F. 1982, Astrophysical Journal, 255, 419

Blanton, M. R., & Roweis, S. 2007, Astronomical Journal, 133, 734

Blondin, S., & Tonry, J. L. 2007, Astrophysical Journal, 666, 1024

Böker, T., Laine, S., van der Marel, R. P., et al. 2002, Astronomical Journal, 123, 1389

Böker, T., Sarzi, M., McLaughlin, D. E., et al. 2004, Astronomical Journal, 127, 105

Brightman, M., Silverman, J. D., Mainieri, V., et al. 2013, Monthly Notices of the Royal Astronomical Society, 433, 2485

Bromm, V., & Loeb, A. 2003, Astrophysical Journal, 596, 34

Cappellari, M., & Emsellem, E. 2004, Publications of the Astronomical Society of the Pacific, 116, 138

Chen, C.-T. J., Brandt, W. N., Reines, A. E., et al. 2017, Astrophysical Journal, 837, 48

Chon, S., & Latif, M. A. 2017, Monthly Notices of the Royal Astronomical Society, 467, 4293

Côté, P., Piatek, S., Ferrarese, L., et al. 2006, Astrophysical Journal Supplements, 165, 57

Côté, P., Ferrarese, L., Jordán, A., et al. 2007, Astrophysical Journal, 671, 1456

Crowther, P. A. 2007, Annual Reviews of Astronomy & Astrophysics, 45, 177

Crowther, P. A., & Walborn, N. R. 2011, Monthly Notices of the Royal Astronomical Society, 416, 1311

Davies, M. B., Miller, M. C., & Bellovary, J. M. 2011, Astrophysical Journal Letters, 740, L42

De Robertis, M. M., & Osterbrock, D. E. 1984, Astrophysical Journal, 286, 171

den Brok, M., Seth, A. C., Barth, A. J., et al. 2015, Astrophysical Journal, 809, 101

Desroches, L.-B., Greene, J. E., & Ho, L. C. 2009, ApJ, 698

Dijkstra, M., Ferrara, A., & Mesinger, A. 2014, Monthly Notices of the Royal Astronomical Society, 442, 2036

Done, C., Davis, S. W., Jin, C., Blaes, O., & Ward, M. 2012, Monthly Notices of the Royal Astronomical Society, 420, 1848

Dong, R., Greene, J. E., & Ho, L. C. 2012a, Astrophysical Journal, 761, 73

Dong, X.-B., Ho, L. C., Yuan, W., et al. 2012b, Astrophysical Journal, 755, 167

Dressler, A., & Richstone, D. O. 1988, Astrophysical Journal, 324, 701

Elvis, M., Wilkes, B. J., McDowell, J. C., et al. 1994, Astrophysical Journal Supplements, 95, 1

Fabian, A. C., Iwasawa, K., Reynolds, C. S., & Young, A. J. 2000, Publications of the Astronomical Society of the Pacific, 112, 1145

Ferrara, A., Salvadori, S., Yue, B., & Schleicher, D. 2014, Monthly Notices of the Royal Astronomical Society, 443, 2410

Ferrarese, L., & Ford, H. 2005, Space Science Reviews, 116, 523

Ferrarese, L., & Merritt, D. 2000, Astrophysical Journal Letters, 539, L9

Ferrarese, L., Côté, P., Jordán, A., et al. 2006, ApJ, 164, 334

Filippenko, A. V. 1989, Astronomical Journal, 97, 726

—. 1997, Annual Reviews of Astronomy & Astrophysics, 35, 309

Filippenko, A. V., & Ho, L. C. 2003, Astrophysical Journal Letters, 588, L13

Filippenko, A. V., & Sargent, W. L. W. 1989, Astrophysical Journal Letters, 342, L11

Foley, R. J., Berger, E., Fox, O., et al. 2011, Astrophysical Journal, 732, 32

Freitag, M., Gürkan, M. A., & Rasio, F. A. 2006, Monthly Notices of the Royal Astronomical Society, 368, 141

Gal-Yam, A., & Leonard, D. C. 2009, Nature, 458, 865

Gebhardt, K., Bender, R., Bower, G., et al. 2000a, Astrophysical Journal Letters, 539, L13

Gebhardt, K., Richstone, D., Kormendy, J., et al. 2000b, Astronomical Journal, 119, 1157

Gebhardt, K., Richstone, D., Tremaine, S., et al. 2003, Astrophysical Journal, 583, 92

Gehrels, N. 1986, Astrophysical Journal, 303, 336

Georgiev, I. Y., & Böker, T. 2014, Monthly Notices of the Royal Astronomical Society, 441, 3570

Ghez, A. M., Salim, S., Hornstein, S. D., et al. 2005, Astrophysical Journal, 620, 744

Ghez, A. M., Duchêne, G., Matthews, K., et al. 2003, Astrophysical Journal Letters, 586, L127

Ghez, A. M., Salim, S., Weinberg, N. N., et al. 2008, Astrophysical Journal, 689, 1044

Gilfanov, M. 2004, MNRAS, 349, 146

Graham, A. W., Ciambur, B. C., & Soria, R. 2016, Astrophysical Journal, 818, 172

Graur, O., Bianco, F. B., & Modjaz, M. 2015, Monthly Notices of the Royal Astronomical Society, 450, 905

Graur, O., & Maoz, D. 2013, Monthly Notices of the Royal Astronomical Society, 430, 1746

Greene, J. E. 2012, Nature Communications, 3

Greene, J. E., & Ho, L. C. 2004, Astrophysical Journal, 610, 722

—. 2005a, Astrophysical Journal, 627, 721

—. 2005b, Astrophysical Journal, 630, 122

—. 2007, Astrophysical Journal, 670, 92

Greene, J. E., Ho, L. C., & Barth, A. J. 2008, Astrophysical Journal, 688, 159

Greene, J. E., Peng, C. Y., Kim, M., et al. 2010, Astrophysical Journal, 721, 26

Greene, J. E., Seth, A., Kim, M., et al. 2016, Astrophysical Journal Letters, 826, L32

Grimm, H.-J., Gilfanov, M., & Sunyaev, R. 2003, Monthly Notices of the Royal Astronomical Society, 339, 793

Groves, B. A., Heckman, T. M., & Kauffmann, G. 2006, Monthly Notices of the Royal Astronomical Society, 371, 1559

Gültekin, K., Richstone, D. O., Gebhardt, K., et al. 2009, Astrophysical Journal, 698, 198

Guseva, N. G., Izotov, Y. I., & Thuan, T. X. 2000, Astrophysical Journal, 531, 776

Habouzit, M., Volonteri, M., & Dubois, Y. 2016, ArXiv e-prints

Hainline, K. N., Reines, A. E., Greene, J. E., & Stern, D. 2016, Astrophysical Journal, 832, 119

Hao, L., Strauss, M. A., Fan, X., et al. 2005, Astronomical Journal, 129, 1795

Häring, N., & Rix, H.-W. 2004, Astrophysical Journal Letters, 604, L89

Heckman, T. M., Miley, G. K., van Breugel, W. J. M., & Butcher, H. R. 1981, Astrophysical Journal, 247, 403

Heger, A., Fryer, C. L., Woosley, S. E., Langer, N., & Hartmann, D. H. 2003, Astrophysical Journal, 591, 288

Hirano, S., Hosokawa, T., Yoshida, N., et al. 2014, Astrophysical Journal, 781, 60

Hopkins, P. F., Kereš, D., Oñorbe, J., et al. 2014, Monthly Notices of the Royal Astronomical Society, 445, 581

Hopkins, P. F., Murray, N., Quataert, E., & Thompson, T. A. 2010, Monthly Notices of the Royal Astronomical Society, 401, L19

Hopkins, P. F., Torrey, P., Faucher-Giguère, C.-A., Quataert, E., & Murray, N. 2016, Monthly Notices of the Royal Astronomical Society, 458, 816

Hosokawa, T., Omukai, K., Yoshida, N., & Yorke, H. W. 2011, Science, 334, 1250

Iwasawa, K., Fabian, A. C., Almaini, O., et al. 2000, Monthly Notices of the Royal Astronomical Society, 318, 879

Izotov, Y. I., Thuan, T. X., & Guseva, N. G. 2007, Astrophysical Journal, 671, 1297

Jester, S., Schneider, D. P., Richards, G. T., et al. 2005, Astronomical Journal, 130, 873

Jia, J., Ptak, A., Heckman, T. M., et al. 2011, Astrophysical Journal, 731, 55

Jiang, Y.-F., Greene, J. E., & Ho, L. C. 2011a, Astrophysical Journal Letters, 737, L45

Jiang, Y.-F., Greene, J. E., Ho, L. C., Xiao, T., & Barth, A. J. 2011b, Astrophysical Journal, 742, 68

Just, D. W., Brandt, W. N., Shemmer, O., et al. 2007, Astrophysical Journal, 665, 1004

Kalberla, P. M. W., Burton, W. B., Hartmann, D., et al. 2005, Astronomy & Astrophysics, 440, 775

Kasen, D., & Woosley, S. E. 2009, Astrophysical Journal, 703, 2205

Kaspi, S., Smith, P. S., Netzer, H., et al. 2000, Astrophysical Journal, 533, 631

Kauffmann, G., Heckman, T. M., Tremonti, C., et al. 2003, Monthly Notices of the Royal Astronomical Society, 346, 1055

Kelly, B. C., & Merloni, A. 2012, Advances in Astronomy, 2012

Kelly, B. C., Vestergaard, M., Fan, X., et al. 2010, Astrophysical Journal, 719, 1315

Kennicutt, R. C., & Evans, N. J. 2012, Annual Reviews of Astronomy & Astrophysics, 50, 531

Kewley, L. J., Dopita, M. A., Sutherland, R. S., Heisler, C. A., & Trevena, J. 2001, Astrophysical Journal, 556, 121

Kewley, L. J., Groves, B., Kauffmann, G., & Heckman, T. 2006, Monthly Notices of the Royal Astronomical Society, 372, 961

King, A., & Pounds, K. 2015, Annual Reviews of Astronomy & Astrophysics, 53, 115

Kormendy, J. 2004, Coevolution of Black Holes and Galaxies, 1

Kormendy, J., & Ho, L. C. 2013, Annual Reviews of Astronomy & Astrophysics, 51, 511

Kormendy, J., & Kennicutt, Jr., R. C. 2004, Annual Reviews of Astronomy & Astrophysics, 42, 603

Kormendy, J., & Richstone, D. 1992, Astrophysical Journal, 393, 559

Koss, M., Blecha, L., Mushotzky, R., et al. 2014, Monthly Notices of the Royal Astronomical Society, 445, 515

Kotulla, R., Fritze, U., Weilbacher, P., & Anders, P. 2009, Monthly Notices of the Royal Astronomical Society, 396, 462

Kunth, D., Sargent, W. L. W., & Bothun, G. D. 1987, Astronomical Journal, 93, 29

Kuo, C. Y., Braatz, J. A., Condon, J. J., et al. 2011, Astrophysical Journal, 727, 20

Läsker, R., Ferrarese, L., van de Ven, G., & Shankar, F. 2014, Astrophysical Journal, 780, 70

Läsker, R., Greene, J. E., Seth, A., et al. 2016, Astrophysical Journal, 825, 3

Latif, M. A., & Ferrara, A. 2016, Publications of the Astronomical Society of Australia, 33, e051

Lehmer, B. D., Alexander, D. M., Bauer, F. E., et al. 2010, Astrophysical Journal, 724, 559

Lemons, S. M., Reines, A. E., Plotkin, R. M., Gallo, E., & Greene, J. E. 2015, Astrophysical Journal, 805, 12

Li, W., Chornock, R., Leaman, J., et al. 2011a, Monthly Notices of the Royal Astronomical Society, 412, 1473

Li, W., Leaman, J., Chornock, R., et al. 2011b, Monthly Notices of the Royal Astronomical Society, 412, 1441

Li, W. D., Filippenko, A. V., Treffers, R. R., et al. 2000, in American Institute of Physics Conference Series, Vol. 522, American Institute of Physics Conference Series, ed. S. S. Holt & W. W. Zhang, 103–106

Lodato, G., & Natarajan, P. 2006, Monthly Notices of the Royal Astronomical Society, 371, 1813

Loeb, A., & Rasio, F. A. 1994, Astrophysical Journal, 432, 52

Lusso, E., & Risaliti, G. 2016, Astrophysical Journal, 819, 154

Madau, P., & Haardt, F. 2015, Astrophysical Journal Letters, 813, L8

Madau, P., Haardt, F., & Dotti, M. 2014, Astrophysical Journal Letters, 784, L38

Madau, P., & Rees, M. J. 2001, Astrophysical Journal Letters, 551, L27

Magorrian, J., Tremaine, S., Richstone, D., et al. 1998, Astronomical Journal, 115, 2285

Marconi, A., & Hunt, L. K. 2003, Astrophysical Journal Letters, 589, L21

Marconi, A., Risaliti, G., Gilli, R., et al. 2004, Monthly Notices of the Royal Astronomical Society, 351, 169

Marshall, J. L., Burles, S., Thompson, I. B., et al. 2008, in Society of Photo-Optical Instrumentation Engineers (SPIE) Conference Series, Vol. 7014, Society of Photo-Optical Instrumentation Engineers (SPIE) Conference Series, 54

Martini, P., Stoll, R., Derwent, M. A., et al. 2011, Publications of the Astronomical Society of the Pacific, 123, 187

McConnell, N. J., & Ma, C.-P. 2013, Astrophysical Journal, 764, 184

McConnell, N. J., Ma, C.-P., Murphy, J. D., et al. 2012, Astrophysical Journal, 756, 179

Medling, A. M., U, V., Max, C. E., et al. 2015, Astrophysical Journal, 803, 61

Menéndez-Delmestre, K., Sheth, K., Schinnerer, E., Jarrett, T. H., & Scoville, N. Z. 2007, Astrophysical Journal, 657, 790

Merloni, A., Heinz, S., & di Matteo, T. 2003, Monthly Notices of the Royal Astronomical Society, 345, 1057

Merritt, D. 2009, Astrophysical Journal, 694, 959

Merritt, D., Ferrarese, L., & Joseph, C. L. 2001, Science, 293, 1116

Mezcua, M., Civano, F., Fabbiano, G., Miyaji, T., & Marchesi, S. 2016, Astrophysical Journal, 817, 20

Miller, B. P., Gallo, E., Greene, J. E., et al. 2015, Astrophysical Journal, 799, 98

Miller, M. C., & Davies, M. B. 2012, Astrophysical Journal, 755, 81

Miller, M. C., & Lauburg, V. M. 2009, Astrophysical Journal, 692, 917

Milosavljević, M., Bromm, V., Couch, S. M., & Oh, S. P. 2009, Astrophysical Journal, 698, 766

Mineo, S., Gilfanov, M., & Sunyaev, R. 2012, Monthly Notices of the Royal Astronomical Society, 419, 2095

Miyoshi, M., Moran, J., Herrnstein, J., et al. 1995, Nature, 373, 127

Moran, E. C., Eracleous, M., Leighly, K. M., et al. 2005, Astronomical Journal, 129, 2108

Moran, E. C., Shahinyan, K., Sugarman, H. R., Vélez, D. O., & Eracleous, M. 2014, Astronomical Journal, 148, 136

Mortlock, D. J., Warren, S. J., Venemans, B. P., et al. 2011, Nature, 474, 616

Mullaney, J. R., Alexander, D. M., Fine, S., et al. 2013, Monthly Notices of the Royal Astronomical Society, 433, 622

Murray, N., Quataert, E., & Thompson, T. A. 2005, Astrophysical Journal, 618, 569

Mushotzky, R. F., Done, C., & Pounds, K. A. 1993, Annual Reviews of Astronomy & Astrophysics, 31, 717

Natarajan, P., Pacucci, F., Ferrara, A., et al. 2017, Astrophysical Journal, 838, 117

Neumayer, N., & Walcher, C. J. 2012, Advances in Astronomy, 2012

O'Neill, P. M., Kaspi, S., Laor, A., et al. 2006, Astrophysical Journal, 645, 160

Paggi, A., Fabbiano, G., Civano, F., et al. 2016, Astrophysical Journal, 823, 112

Panessa, F., Bassani, L., Cappi, M., et al. 2006, Astronomy & Astrophysics, 455, 173

Pardo, K., Goulding, A. D., Greene, J. E., et al. 2016, Astrophysical Journal, 831, 203

Park, T., Kashyap, V. L., Siemiginowska, A., et al. 2006, Astrophysical Journal, 652, 610

Peng, C. Y., Ho, L. C., Impey, C. D., & Rix, H.-W. 2002, Astronomical Journal, 124, 266

—. 2010, Astronomical Journal, 139, 2097

Peterson, B. M., Ferrarese, L., Gilbert, K. M., et al. 2004, Astrophysical Journal, 613, 682

Plotkin, R. M., Gallo, E., Haardt, F., et al. 2016, Astrophysical Journal, 825, 139

Polletta, M., Tajer, M., Maraschi, L., et al. 2007, Astrophysical Journal, 663, 81

Portegies Zwart, S. F., Baumgardt, H., Hut, P., Makino, J., & McMillan, S. L. W. 2004, Nature, 428, 724

Pritchard, T. A., Roming, P. W. A., Brown, P. J., et al. 2012, Astrophysical Journal, 750, 128

Prugniel, P., & Soubiran, C. 2001, Astronomy & Astrophysics, 369, 1048

Reines, A. E., & Comastri, A. 2016, Publications of the Astronomical Society of Australia, 33, e054

Reines, A. E., & Deller, A. T. 2012, Astrophysical Journal Letters, 750, L24

Reines, A. E., Greene, J. E., & Geha, M. 2013, Astrophysical Journal, 775, 116

Reines, A. E., Plotkin, R. M., Russell, T. D., et al. 2014, Astrophysical Journal Letters, 787, L30

Reines, A. E., Reynolds, M. T., Miller, J. M., et al. 2016, Astrophysical Journal Letters, 830, L35

Reines, A. E., Sivakoff, G. R., Johnson, K. E., & Brogan, C. L. 2011, Nature, 470, 66

Reines, A. E., & Volonteri, M. 2015, Astrophysical Journal, 813, 82

Remillard, R. A., & McClintock, J. E. 2006, Annual Reviews of Astronomy & Astrophysics, 44, 49

Richards, G. T., Lacy, M., Storrie-Lombardi, L. J., et al. 2006, Astrophysical Journal Supplements, 166, 470

Riess, A. G. 2011, An Independent Determination of WFC3-IR Zeropoints and Count Rate Non-Linearity from 2MASS Asterisms, Tech. rep.

Risaliti, G., & Elvis, M. 2004, in Astrophysics and Space Science Library, Vol. 308, Supermassive Black Holes in the Distant Universe, ed. A. J. Barger, 187

Ruan, J. J., Anderson, S. F., Cales, S. L., et al. 2015, ArXiv e-prints

Runnoe, J. C., Cales, S., Ruan, J. J., et al. 2016, Monthly Notices of the Royal Astronomical Society, 455, 1691

Salpeter, E. E. 1964, Astrophysical Journal, 140, 796

Sartori, L. F., Schawinski, K., Treister, E., et al. 2015, Monthly Notices of the Royal Astronomical Society, 454, 3722

Schauer, A. T. P., Agarwal, B., Glover, S. C. O., et al. 2017, Monthly Notices of the Royal Astronomical Society, 467, 2288

Schlafly, E. F., & Finkbeiner, D. P. 2011, Astrophysical Journal, 737, 103

Schmidt, M. 1963, Nature, 197, 1040

Schödel, R., Ott, T., Genzel, R., et al. 2003, Astrophysical Journal, 596, 1015

—. 2002, Nature, 419, 694

Schwarzschild, M. 1979, Astrophysical Journal, 232, 236

Sérsic, J. L. 1963, Boletin de la Asociacion Argentina de Astronomia La Plata Argentina, 6, 41

Seth, A. C., van den Bosch, R., Mieske, S., et al. 2014, Nature, 513, 398

Shangguan, J., Liu, X., Ho, L. C., et al. 2016, Astrophysical Journal, 823, 50

Shen, Y., & Kelly, B. C. 2012, Astrophysical Journal, 746, 169

Shen, Y., & Liu, X. 2012, Astrophysical Journal, 753, 125

Simard, L., Mendel, J. T., Patton, D. R., Ellison, S. L., & McConnachie, A. W. 2011, Astrophysical Journal Supplements, 196, 11

Simcoe, R. A., Sullivan, P. W., Cooksey, K. L., et al. 2012, Nature, 492, 79

Smith, N. 2014, Annual Reviews of Astronomy & Astrophysics, 52, 487

Smith, N., Li, W., Silverman, J. M., Ganeshalingam, M., & Filippenko, A. V. 2011a, Monthly Notices of the Royal Astronomical Society, 415, 773

Smith, N., Li, W., Miller, A. A., et al. 2011b, Astrophysical Journal, 732, 63

Soltan, A. 1982, Monthly Notices of the Royal Astronomical Society, 200, 115

Stern, D., Assef, R. J., Benford, D. J., et al. 2012, Astrophysical Journal, 753, 30

Stern, J., & Laor, A. 2012, Monthly Notices of the Royal Astronomical Society, 423, 600

Stone, N. C., Küpper, A. H. W., & Ostriker, J. P. 2017, Monthly Notices of the Royal Astronomical Society, 467, 4180

Stone, N. C., & Metzger, B. D. 2016, Monthly Notices of the Royal Astronomical Society, 455, 859

Tananbaum, H., Avni, Y., Branduardi, G., et al. 1979, Astrophysical Journal Letters, 234, L9

Thornton, C. E., Barth, A. J., Ho, L. C., Rutledge, R. E., & Greene, J. E. 2008, Astrophysical Journal, 686, 892

Tremou, E., Garcia-Marin, M., Zuther, J., et al. 2015, Astronomy & Astrophysics, 580, A113

Urry, C. M., & Padovani, P. 1995, Publications of the Astronomical Society of the Pacific, 107, 803

Valluri, M., Ferrarese, L., Merritt, D., & Joseph, C. L. 2005, Astrophysical Journal, 628, 137

Valluri, M., Merritt, D., & Emsellem, E. 2004, Astrophysical Journal, 602, 66

van den Bosch, R. C. E., & de Zeeuw, P. T. 2010, Monthly Notices of the Royal Astronomical Society, 401, 1770

Vasudevan, R. V., & Fabian, A. C. 2009, Monthly Notices of the Royal Astronomical Society, 392, 1124

Veilleux, S., & Osterbrock, D. E. 1987, Astrophysical Journal Supplements, 63, 295

Volonteri, M. 2010, A&A Rev., 18

Volonteri, M., & Begelman, M. C. 2010, Monthly Notices of the Royal Astronomical Society, 409, 1022

Volonteri, M., Lodato, G., & Natarajan, P. 2008, Monthly Notices of the Royal Astronomical Society, 383, 1079

Volonteri, M., & Natarajan, P. 2009, Monthly Notices of the Royal Astronomical Society, 400, 1911

Volonteri, M., & Reines, A. E. 2016, Astrophysical Journal Letters, 820, L6

Walsh, J. L., van den Bosch, R. C. E., Gebhardt, K., et al. 2016, Astrophysical Journal, 817, 2

Weigel, A. K., Schawinski, K., Treister, E., et al. 2015, Monthly Notices of the Royal Astronomical Society, 448, 3167

Wenger, M., Ochsenbein, F., Egret, D., et al. 2000, Astronomy & Astrophysics Supplements, 143, 9

Whitmore, B. C. 1980, Astrophysical Journal, 242, 53

Whittle, M. 1985, Monthly Notices of the Royal Astronomical Society, 213, 1

Woo, J.-H., Yoon, Y., Park, S., Park, D., & Kim, S. C. 2015, Astrophysical Journal, 801, 38

Woo, J.-H., Treu, T., Barth, A. J., et al. 2010, Astrophysical Journal, 716, 269

Wright, E. L. 2006, Publications of the Astronomical Society of the Pacific, 118, 1711

Xiao, T., Barth, A. J., Greene, J. E., et al. 2011, Astrophysical Journal, 739, 28

Xue, Y. Q., Luo, B., Brandt, W. N., et al. 2011, Astrophysical Journal Supplements, 195, 10

York, D. G., Adelman, J., Anderson, Jr., J. E., et al. 2000, Astronomical Journal, 120, 1579

Zakamska, N. L., & Greene, J. E. 2014, Monthly Notices of the Royal Astronomical Society, 442, 784